THE UNIVERSITY *of* EDINBURGH

EVAPORATION OF LIQUID LAYERS AND DROPS

Pedro J. Sáenz

Thesis submitted for the degree of

Doctor *of* Philosophy

at

The University *of* Edinburgh

April, 2014

Declaration

I declare that this thesis and the work described herein are my own, except where explicitly stated otherwise in the text. These have been conducted under the guidance of Dr. Prashant Valluri and Prof. Khellil Sefiane at the Institute for Materials and Processes in the School of Engineering of The University of Edinburgh. The work has not been submitted for any other degree or professional qualification.

Pedro J. Sáenz
22nd October 2014

Acknowledgments

I dedicate this work to my family for their unconditional love and support. Nobody can be more grateful than me for having such parents as Inés and Nicolás who have devoted their lives to provide my siblings and me with all the opportunities that they never had. Nobody can feel prouder of having a brother like David who shows me everyday what fighting and overcoming adversity really is. Nobody can feel more fortunate of having a sister like Soraya who makes my life meaningful. To them, to my "second mother", my grandmother Josefa, and to the rest of my relatives, thank you.

I am also deeply grateful to my supervisors Dr. P. Valluri and Prof. K. Sefiane for their guidance and patience and for providing me with more opportunities than I could have ever wished for. My special thanks also go to Prof. O. K. Matar and Dr. G. Karapetsas for enlightening and fruitful collaborations. I would like to acknowledge with grateful thanks all members of the School, faculty and staff, for being exceptionally passionate about their work. Special gratitude must be extended to the IMP members for making of Sanderson Building the most constructive, supportive and joyful workplace that one could desire. Among my colleges, I should mention Dani, Alex, Ares, Olga and Alex and apologize to the rest, they are too many to name all of them here. It has been my greatest pleasure being part of this group of exceptional individuals and of The University of Edinburgh.

My deepest gratitude must go to Dan, who has become like a brother to me, for his endless patience and continuous support, especially valuable in those "whisky days", and for all the fantastic moments that we have shared during these years. Other especially important person in my life to whom I am also sincerely thankful is Laura, without her I would not have taken the path that has brought me here. My special love and gratitude

should be extended to my friends in Spain who, despite the distance that stands between us, are present in my heart everyday. I will never be able to thank them enough for so many things.

My placement in the United States had a profound impact on me. I will be forever in debt with Prof. J. Kim for welcoming me not only in his laboratory but also in his home. Many of the moments that we shared and his perspective on life are things that I will never forget. Many thanks also to all the members of the PCHT lab and, especially, to Alex and Valentin for helping me with my experiments and for the laughs that we shared everyday. A wonderful surprise of my placement was meeting Kristen. I am deeply grateful to her for her efforts to help me integrate in Maryland, for the moments that we shared and for everything that I have learned from her. Thanksgiving with the Aquilino family will always be a priceless gift.

To conclude, I would like to express my sincerest gratitude to a certain teacher of mine, who I admired above the rest and still do, for discouraging me from pursuing studies abroad. Without being aware of, he taught me that we should not make other people's limits our own.

Invictus

Out of the night that covers me,
Black as the pit from pole to pole,
I thank whatever gods may be
For my unconquerable soul.

In the fell clutch of circumstance
I have not winced nor cried aloud.
Under the bludgeonings of chance
My head is bloody, but unbowed.

Beyond this place of wrath and tears
Looms but the horror of the shade,
And yet the menace of the years
Finds and shall find me unafraid.

It matters not how strait the gate,
How charged with punishments the scroll,
I am the master of my fate:
I am the captain of my soul.

William Ernest Henley

"If you are uncomfortable with your fears,
go where your fears are and get comfortable."
- Anonymous

Preface

This thesis focuses on investigating the stability, dynamics and physical mechanisms of thermocapillary flows undergoing phase change by means of direct numerical simulations and experiments. The novelty of the general approach developed in this work lies in the fact that the problems under consideration are addressed with novel fully-coupled transient two-phase flow models in 3D. Traditional simplifications are avoided by accounting for deformable interfaces and by addressing advection-diffusion mechanisms not only in the liquid but also in the gas. This strategy enables a realistic investigation of the interface energy and mass transfer at a local scale for the first time. Thorough validations of the models against theory and experiments are presented. The thesis encompasses three situations in detail: liquid layers in saturated environments, liquid layers in unsaturated environments and evaporation of liquid droplets.

Firstly, a model grounded in the volume-of-fluid method is developed to study the stability of laterally-heated liquid layers under saturated environments. In this configuration, the planar layer is naturally vulnerable to the formation of an oscillatory regime characterized by a myriad of thermal wave-like patterns propagating along the gas-liquid interface, i.e. hydrothermal waves. The nonlinear growth of the instabilities is discussed extensively along with the final bulk flow for both the liquid and gas phases. Previously unknown interface deformations, i.e. physical waves, induced by, and enslaved to, the hydrothermal waves are reported. The mechanism of heat transfer across the interface is found to contradict previous single-phase studies since the travelling nature of the hydrothermal waves leads to maximum heat fluxes not at the points of extreme temperatures but somewhere in between.

The model for saturated environments is extended in a second stage to assess the

effect of phase change in the hydrothermal waves for the first time. New numerical results reveal that evaporation affects the thermocapillary instabilities in two ways: the latent energy required during the process tends to inhibit the hydrothermal waves while the accompanying level reduction enhances the physical waves by minimizing the role of gravity. Interestingly, the hydrothermal-wave-induced convective patterns in the gas decouple the interface vapour concentration with that in the bulk of the gas leading to the formation of high (low) concentrations of vapour at a certain distance above interface cold (hot) spots. At the interface the behavior is the opposite. The phase-change mechanism for stable layers is also discussed. The Marangoni effect plays a major role in the vapour distribution and local evaporation flux and can lead to the inversion of phase-change process, i.e. the thermocapillary flow can result into local condensation in an otherwise evaporating liquid layer.

The third problem discussed in this thesis concerns with the analysis of evaporating sessile droplets by means of both experiments and 3D numerical modeling. An experimental apparatus is designed to study the evaporation process of water droplets on superheated substrates in controlled nitrogen environments. The droplets are simultaneously recorded with a CCD camera from the side and with an infrared camera from top. It is found that the contact line initially remains pinned for at least 70% of the time, period after which its behaviour changes to that of the stick-slip mode and the drop dries undergoing contact line jumps. For lower temperatures an intermediate stage has been observed wherein the drop evaporates according to a combined mode. The experimental work is complemented with numerical simulations. A new model implementing the diffuse-interface method has been developed to solve the more complex problems of this configuration, especially those associated with the intricate contact-line dynamics. Further insights into the two-phase flow dynamics have been provided as well as into the initial transient stage, in which the Marangoni effect has been found to play a major role in the droplet heating. For the first time, a fully-coupled two-phase direct numerical simulations of sessile drops with a moving contact line has been performed. The last part of this work has been devoted to the investigation of three-dimensional phenomena on drops with irregular contact area. Non-sphericity leads to complex three-dimensional drop shapes with intricate contract

angle distributions along the triple line. The evaporation rate is found to be affected by 3D features as well as the bulk flow, which become completely non-axisymmetric. To the best of our knowledge, this work is the first time that three-dimensional two-phase direct numerical simulations of evaporating sessile drops have been undertaken.

Contents

Nomenclature

Acronyms

CA	Constant-angle evaporation mode
CR	Constant-radius evaporation mode
CSF	Continuum surface force model
DI	Diffuse-interface method
DNS	Direct numerical simulations
FFT	Fast-Fourier transform
HTW	Hydrothermal wave
LHS	Left-hand side
MCL	Moving contact line
PCL	Pinned contact line
RHS	Right-hand side
VOF	Volume-of-fluid method

Dimensional analysis

$\hat{x}$	Dimensional variable

x	Dimensionless variable	

Physical properties

α	Thermal diffusivity	$m^2\ s^{-1}$
β	Thermal expansivity	K^{-1}
c_{pl}	Specific heat capacity	$J\ kg^{-1}\ K^{-1}$
D	Binary coefficient of mass diffusivity	$m^2\ s^{-1}$
Δh_v	Latent heat	$J\ kg^{-1}$
γ	Temperature coefficient of the surface tension	$N\ m^{-1}\ K^{-1}$
k	Thermal conductivity	$W\ m^{-1}\ K^{-1}$
M	Molecular weight	$g\ mol^{-1}$
μ	Dynamic viscosity	Pa s
ν	Kinematic viscosity	$m^2\ s^{-1}$
ρ	Density	$kg\ m^{-3}$
σ	Surface tension	$N\ m^{-1}$

Subscripts and superscripts

g	Gas mixture (Non-condensable gas in chapter 3)
$g1$	Non-condensable gas
$g2$	Vapour
l	Liquid
r	Refernce value (25°C)

s	Saturation
$'$	Disturbance (deviation from the base state)

Other variables

c	Liquid volume fraction
c_R	Phase speed
d	Layer depth
ΔT	Temperature difference
d_g	Gas depth
ε	Measure of the interface thickness
η_t	Instability's temporal growth rate
H	Droplet height
h	Heat transfer coefficient
J	Evaporation flux
k	Overall wavenumber
κ	Interface curvature
λ	Wavelength
$M(t)$	Overall evaporation rate
ω	Vapour mass fraction
p	Pressure
ϕ	Chemical potential
ψ	Angle of propagation

$\Psi(c)$	Bulk energy density
R	Droplet base radius
T	Temperature
t	Time
θ	Contact angle
$\mathbf{u}$	Velocity vector (u, v, w)
V	Droplet volume
$\mathbf{x}$	Coordinate vector (x, y, z)
ξ	Generic variable $(u, v, w, T...)$

Dimensionless numbers

B	Biot number $= \frac{\text{convective heat transfer}}{\text{conductive heat transfer}}$	$B = \frac{hd}{k}$
Bo_d	Dynamic Bond number $= \frac{\text{thermogravity forces}}{\text{thermocapillary forces}}$	$Bo_d = \frac{\rho\beta g L^2}{\gamma}$
Ca	Capillary number $= \frac{\text{viscous forces}}{\text{surface tension forces}}$	$Ca = \frac{\mu U}{\sigma}$
Fr	Froude number $= \frac{\text{inertial force}}{\text{gravitational force}}$	$Fr = \frac{U^2}{gL}$
Ja	Jakob number $= \frac{\text{sensible heat}}{\text{latent heat}}$	$Ja = \frac{c_p \Delta T}{\Delta h_v}$
Ma	Marangoni number $= \frac{\text{thermocapillary forces}}{\text{viscous forces}}$	$Ma = \frac{\gamma \Delta T L}{\mu \alpha}$
Pr	Prandtl number $= \frac{\text{momentum diffusivity}}{\text{thermal diffusivity}}$	$Pr = \frac{\nu}{\alpha}$
Re	Reynolds number $= \frac{\text{convective momentum transport}}{\text{viscous momentum transport}}$	$Re = \frac{\rho U L}{\mu}$
Sc	Schmidt number $= \frac{\text{momentum diffusivity}}{\text{mass diffusivity}}$	$Sc = \frac{\nu}{D}$
We	Weber number $= \frac{\text{inertial forces}}{\text{surface tension forces}}$	$We = \frac{\rho U^2 L}{\sigma}$

Chapter 1

Introduction

Phase change, capillarity and wetting phenomena are fundamental physical phenomena encountered in a vast number of practical situations. Despite their paramount importance and the many scientific attempts to shed light on them, these are highly complex phenomena in which much still remains unknown.

At this point, it may be appropriate to introduce some of the basic concepts of interface dynamics which recurrently appear in different chapters of this Thesis. To start with, *surface tension* can be defined as the force existing on the surface of a liquid due to asymmetries in the intermolecular cohesive (strong) and adhesive (weak) forces between surface molecules. These are only partially surrounded by other liquid molecules and, therefore, exhibit a stronger attractive force upon their neighbouring molecules in the bulk. The net effect is an inward force that tends to minimise the surface area. The liquid behaves as if its surface were covered with a stretched elastic membrane.

The *Marangoni effect* consists in the change of the effective surface-tension force along a liquid-gas interface due to variations in temperature and/or chemical composition. This investigation is restricted to changes in temperature. If the variation in the surface tension is nonuniform throughout the interface, stress gradients arise inducing interface flow wherein fluid is driven from low to high surface-tension regions. With the exception of the rare superfluids, both liquid and gaseous phases of any fluid are viscous to a higher or lower degree. Thus, the momentum transport leads the interface motion to generate fluid flow also in the bulk of the phases. These surface-tension driven currents are referred to

as *Marangoni flow*, in general, or as *thermocapillary flow,* if the stress gradients are due to temperature solely. If the temperature gradients are larger than a critical threshold inherent to the physical system, some thermocapillary flows are naturally vulnerable to departure from their equilibrium state and to the consequent development of an oscillatory regime characterized by thermal fluctuations travelling along the interface at a certain angle with respect to the surface flow. These instabilities are called *hydrothermal waves*.

Phase change is the generic term employed to describe any process whereby molecules in certain phase (solid, liquid or gas) gain or lose sufficient energy to enter a different physical state. In subsequent chapters, the attention is essentially focused on the spontaneous phase transition from liquid phase to gas phase, i.e. *evaporation*, and vice versa, i.e. *condensation*. As opposed to *boiling*, which occurs in the bulk of the liquid when this is at the boiling temperature, evaporation takes place at the surface of the liquid only and at much lower temperatures.

1.1 History

More often than one would think, the quickest path to move forward in Science will first take you deep into the past. It is fundamental to know the origins and historical evolution of the subject matter if one aims to contribute to its development. Isaac Newton (1642-1727) firmly believed this and even reminded it to others. On a letter to a contemporary English scientist, Robert Hooke (1635-1703), while they were in dispute over optical discoveries, he wrote his famous statement *"If I have seen further, it is by standing on the shoulders of Giants"*. If truth be told, Newton popularised this quote but its first use in reality is attributed to the 12th-century philosopher Bernard of Chartres (11th century-1130). Authorship issues apart, what Newton was saying in such romantic style was nothing but that scientists should thoroughly study the works by previous colleagues, the *Giants*, or they may find themselves making no original discovery or one very poor in relation to their true capacity.

Curiously, it is the aforementioned recipient of Newton's correspondence who was one of the first scientists interested in capillarity and wetting phenomena. In 1661, Hooke

presented to his colleagues a pamphlet [1] with his very first scientific finding. In it, he demonstrated experimentally that when a glass tube was immersed in a bowl of water, the water within the tube would rise up to a level higher that the surface level of water in the bowl, and that the narrower the tube, the higher water would rise in it. Today, this phenomenon is explained by the so-called capillary action, i.e. the ability of liquids to flow in confined spaces without the assistance, and even in opposition to, external forces such as gravity.

What is it that keeps a drop of water in round shape? Why some insects float on the surface of ponds? Why liquid jets breakup into drops? These are some of the new questions that scientists began to ask themselves at the beginning of the 19th century. To explain these and some other phenomena, one of the most relevant figures in the subject, the English polymath Thomas Young (1773-1829), defended the idea of the liquids being surrounded by a thin, elastic membrane, less dense than the deeper parts of the drop, capable of adhering perfectly to them, and more or less strongly to solid bodies. This consideration led to the concept of surface tension. In 1805, Young presented his work *"An essay on the cohesion of fluids"* [2] wherein he introduced his famous interface force balances, namely the stress equilibrium at the contact line where solid, liquid and gas phases meet (Young equation),

$$\hat{\sigma}_{\mathrm{LG}} \cos\theta = \hat{\sigma}_{\mathrm{SG}} - \hat{\sigma}_{\mathrm{SL}}, \tag{1.1}$$

and the pressure discontinuity across curved interfaces (Young-Laplace equation),

$$\Delta\hat{p} = \hat{\sigma}_{\mathrm{LG}} \left(\frac{1}{\hat{R}_1} + \frac{1}{\hat{R}_2} \right). \tag{1.2}$$

Here, $\hat{\sigma}_{\mathrm{LG}}$, $\hat{\sigma}_{\mathrm{SG}}$ and $\hat{\sigma}_{\mathrm{SL}}$ denote the liquid-gas, solid-gas and solid-liquid interface tensions (the caret decoration identifies dimensional quantities), θ is the contact angle, $\Delta\hat{p}$ is the pressure difference between both sides of the interface, and $\hat{R}_1$ and $\hat{R}_2$ are the principal radii of curvature.

Other authors felt curiosity for the drops that seemed to be continuously forming and rolling down a glass above the surface of strong alcoholic beverages, the so-called "tears of

wine". Despite that this apparent wonder had been known to humans for many centuries (some argue that the first reference can be found in the Book of Proverbs) it was not until the second half of the 19th century when this phenomenon was correctly explained for the first time. In 1855, James Thomson (1822-1892), elder brother of Lord Kelvin, William Thomson, published his interpretation of the tears of wine in his paper *"On certain curious motions observable on the surfaces of wine and other alcoholic liquors"* [3]. He correctly suggested that local surface-tension gradients resulting from nonuniform alcohol evaporation were the driving force responsible for the spontaneous wine motion. In other words, Thomson was the first to introduce the concept of what today is called *Marangoni effect*. Even though Thomson's work was earlier, the phenomenon was, however, named after the Italian physicist Carlo Marangoni (1840-1925) for his dissertation entitled *"On the spreading of liquid droplets"* [4] wherein he concluded that variations not only in chemical composition but also in temperature could result in surface tension gradients.

The fact that capillary phenomena are usually tightly related to evaporation processes was evident once the underlying mechanism responsible for the tears of wine had been understood. Also, the intimate interaction between these phenomena is not surprising since both of them are characteristic of the same singular region of matter between phases, the interface. Between 1874 and 1878, Josiah Willard Gibbs (1839-1903), often regarded as one of the fathers of thermodynamics, provided a comprehensive theoretical treatment of the subject in his pioneering work *"On the equilibrium of heterogeneous substances"* [5]. In recognition of his contribution, the Marangoni effect began to be called the *Gibbs-Marangoni effect*. Other celebrated scientists have also shown interest in these matter. For example, in 1900 Albert Einstein (1879-1955) published his first paper entitled *"Conclusions from the capillarity phenomena"* [6]. Another Nobel laureate, Pierre-Gilles de Gennes (1932-2007), dedicated an important part of his career to the subject and co-authored one of the reference books in the topic: *"Capillarity and wetting phenomena: Drops, bubbles, pearls, waves"* [7].

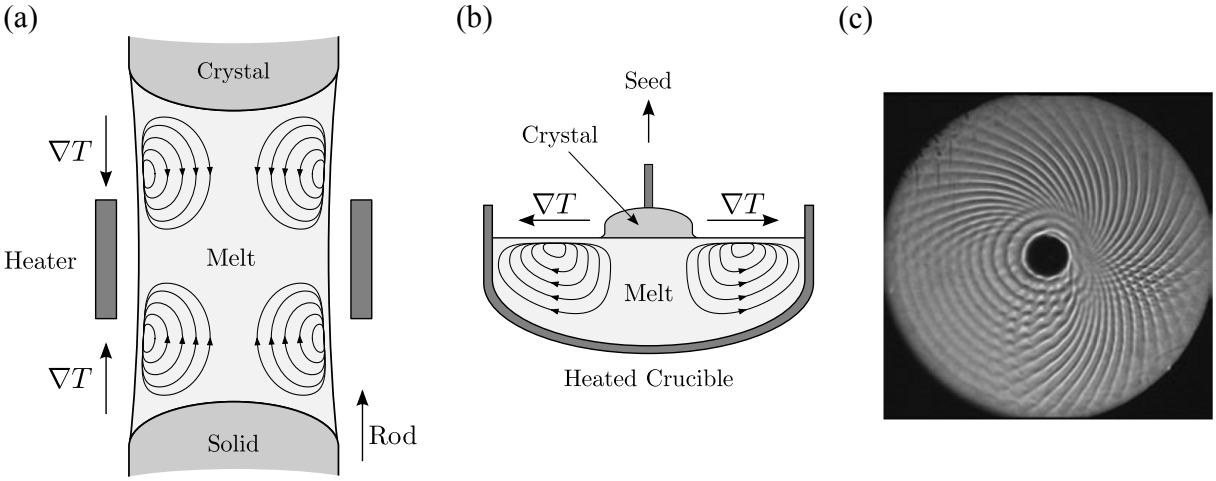

Figure 1.1: Sketches of the (a) floating-zone and (b) Czochralski crystal growth techniques with their typical thermocapillary convection cells; (c) Oscillatory instabilities in a annular pool recreating the conditions in the Czochralski process. Figure (c) has been obtained from Garnier *et al.* [8]

1.2 Modern Interest

Over the last three decades, there has been an increasing interest in the stability of Marangoni-driven flows given their relevance to fundamental industrial processes such as crystal growth of thin-film coating. In particular for the processing of single crystals, the *floating-zone* and the *Czochralski* methods are currently two of the most important techniques employed in industry wherein thermocapillary convection is of paramount importance to obtain a high-quality single crystal with uniform material properties

In the former, see FIG. 1.1a, a rod of material is vertically fed through a thin ring heater. As the rod moves very slowly across the heater, the original metal firsts melts and then recrystallises to form a single crystal. Under this configuration, it has been demonstrated experimentally by Schwabe *et al.* [9] that the liquid bridge held between the two coaxial rods is subjected to thermocapillary convection cells. These result from the axial temperature gradient established between the material next to the heater (hot) and that near the solid ends (colder). A similar type of thermocapillary flow is also found in the *Czochralski* process, normally employed to manufacture ingots of larger diameter for the semiconductor industry. A schematic of the technique is presented in FIG. 1.1b. Here, the original material is melted in a semi-spherical crucible maintained at high temperature. Once the molten metal is homogeneous, a cooled seed is slowly lowered and brought in contact with the melt at the centre of the crucible causing the local fluid temperature

to decrease below the melting point. The metal begins to gradually solidify around the seed at this point, increasing its diameter, while the seed is simultaneously withdrawn upwards. The desired diameter for the resulting single-crystal ingot is adjusted by carefully controlling the equilibrium between the rate of crystallization, mainly dependent on the temperature, and the rate of vertical pull. Since there is heating from the outer wall and cooling in the centre, a radial Marangoni-driven flow is generated with similar fundamental features to that observed in the floating zone.

The topic of thermocapillary convection in crystal growth is comprehensively dealt with by Kuhlmann [10]. One of the problems associated with these processing techniques is the development of striations or segregation bands parallel to the melt-crystal interface. These regions of varying impurity concentration lead to undesirable non-uniform material property distribution which has a profound impact on the quality of the final product. The underlying cause of these striations seems to be a time-dependent crystal-growth speed brought about by temperature oscillations in the melt [11]. Schwabe & Scharmann [12], Chun & Wuest [13] and Schwabe *et al.* [14] provided experimental evidence that, in the processing of single crystals, the above mentioned thermocapillary flow is prone to departure from its equilibrium state and to the consequent development of oscillatory unstable regimes. An example of travelling wave-like thermal instabilities is presented in FIG. 1.1c. Despite the fact that the practical thermocapillary flow shows annular features in both the floating-zone and the Czochralski methods, the fundamental physics are investigated by examining the stability of laterally-heated liquid layers in first instance. To date, the study of this problem has been significantly limited by a number of very unrealistic assumptions, i.e. non-deformable interface or negligible evaporation. The work presented in the first part of this Thesis aims to resolve these and other deficiencies providing further insights into the underlying mechanisms controlling the thermocapillarity instabilities.

The second part of this investigation deals with evaporating sessile droplets controlled by, to a certain extent, similar physical mechanisms. The evaporation of a liquid droplet on a solid substrate is a fundamental physical phenomenon encountered in a vast variety of situations ranging from the biomedical or the industrial to the geophysical or the domestic. In the field of biomedicine, for instance, there is real potential in development

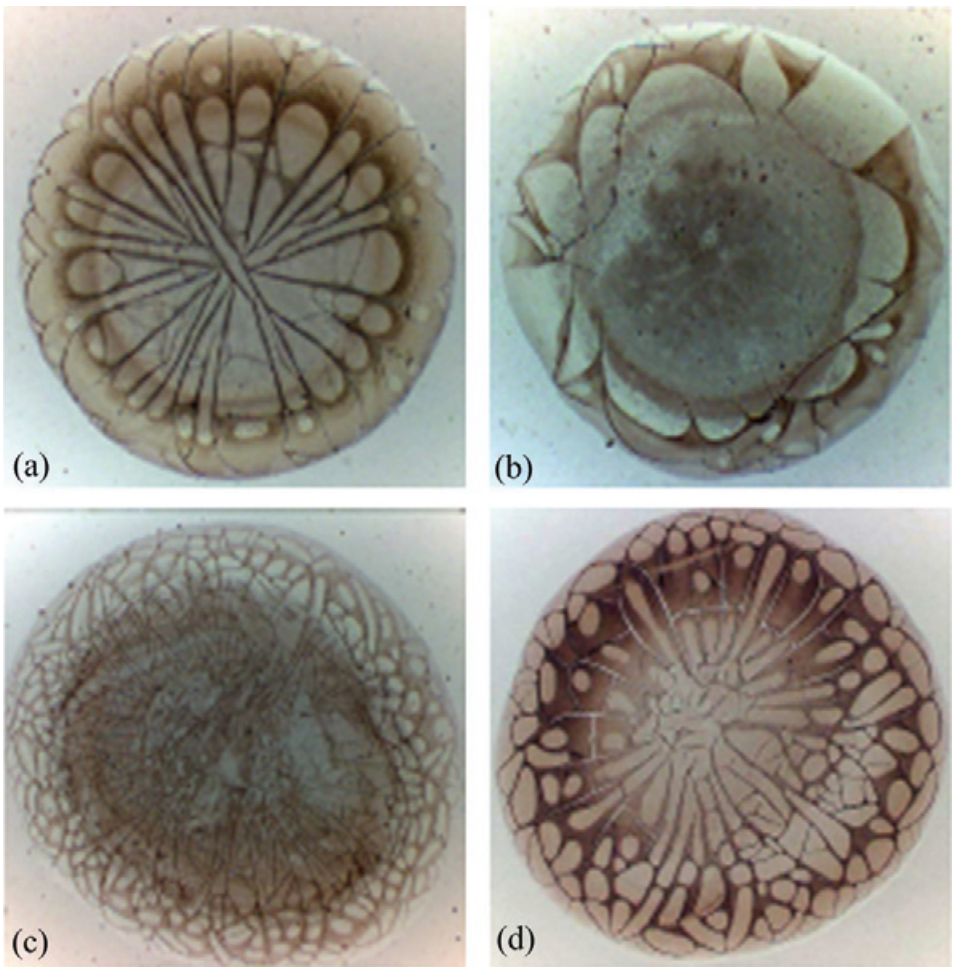

Figure 1.2: Patterns left by dried drops of blood serum of (a) a healthy person; (b), (c), (d) people with different diseases. Figure reproduced from Sefiane [15].

of new techniques for disease diagnosis based on the pattern formation from drying drops of different biofluids [15]. FIG. 1.2 illustrates the different patterns left by dried drops of blood serum depending on the type of disease suffered by the patients. Studying, understanding and interpreting pattern formation from evaporating droplets could lead to a simple and rapid technique for screening of various life threatening diseases [15]. Other important applications of this everyday phenomenon have recently emerged in the development of new methods for gene mapping. Jing *et al.* [16] proposed a high-throughput automatic DNA mapping method based on drying droplet. In this technique, water evaporation is used to induce a microscopic flow with which the DNA molecules can be precisely manipulated. Chopra *et al.* [17] found that, in process of DNA stretching, the final shape of the DNA molecules is intimately related to the flow field induced by the evaporating drop. At a low evaporation rate, the DNA molecules are less stretched and their molecular conformations are folded or coiled, whereas at a high evaporation rate, DNA molecules are more stretched and their shapes become dumbbells or half-dumbbells [18].

From a more industrial point of view, drying drops have widespread applications. To name some, in spray-based thin-film coating processes the final degree of surface smoothness is critically affected by the micro flow within the drop [19]. One of the fundamental reasons to explain this was given by Deegan *et al.* [20, 21] who showed that the uneven particle distribution left by dried particle-laden drops results from the radial capillary flow induced by nonuniform local evaporation along the drop surface. The mechanism described by Deegan and co-workers explains only part of the problem, nonetheless. It fails, for instance, to explain the different patterns found depending on the drop temperature, FIG. 1.3, or any three-dimensional feature, see FIG. 1.2 and FIG. 1.3a. Other examples of applications include micro-electronic cooling [22], DNA chip manufacturing [23], printing and painting [24], etc.

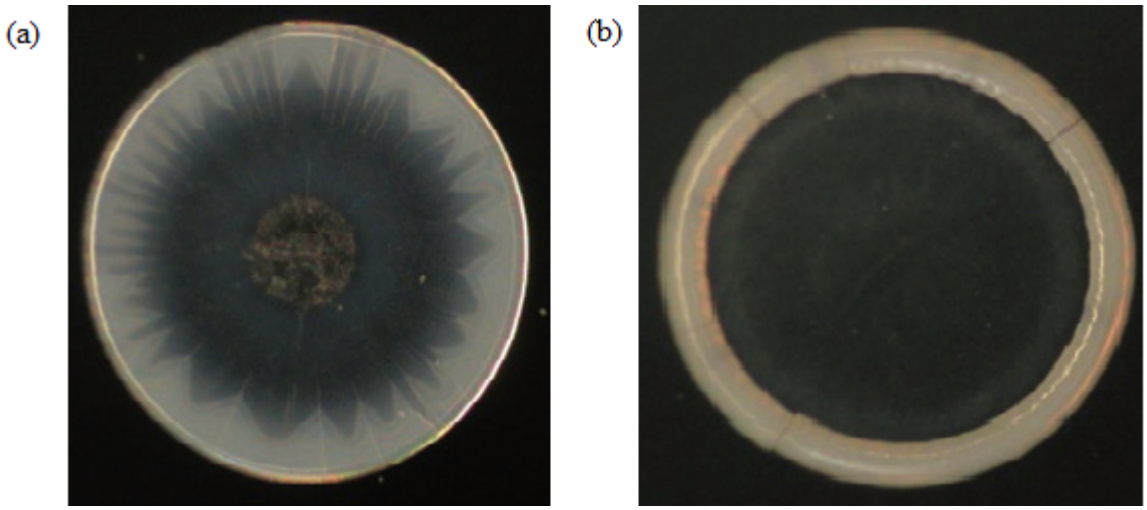

Figure 1.3: Patterns formed from drying $Al_2O_3(5\%) - H_2O$ nanofluid droplets at (a) 40 °C and (b) 70 °C. Figure reproduced from Sefiane [15].

1.3 Organization of this Thesis

This thesis comprises seven chapters, including the current one. A comprehensive literature review of the most relevant works to the subject matter of this investigation is presented in Chapter 2. This is divided into two sections according to the two physical systems examined in subsequent chapters, namely liquid layers and sessile drops.

Chapters 3 and 4 are devoted to the investigation of the dynamics and stability of laterally-heated liquid layers surrounded by saturated (Chapter 3) and unsaturated (Chapter 4) environments. A novel two-phase model with a number of significant improvements, and comparison of results to those obtained by previous methods available in the literature, is presented and validated against experiments and stability theory. The modelling strategy introduced in Chapter 3 is extended in Chapter 4 to address the more realistic case wherein the liquid layer undergoes phase change. Findings from the numerical simulations are discussed extensively throughout these chapters.

Evaporating sessile droplets are examined in Chapters 5 and 6. Experimental work performed on small drops released onto a superheated substrate and surrounded by a controlled environment is described in Chapter 5. The more complex singularities of evaporating drops, mainly due to contact-line dynamics, require the development of a new and more powerful model to simulate them. The details of this novel model are presented in Chapter 6 along with numerical results providing new insights into the underlying

fundamental physics experienced by evaporating sessile drops.

The most important conclusions resulting from the present investigation and the recommendations for future work are summarised in Chapter 7.

Chapter 2

Literature Review

The previous chapter demonstrates the chronological interest in phase change and capillary phenomena since the 17th century. The topic has gained classical significance and the number of investigations available in the literature is vast. Furthermore, over the last two decades there has been a remarkably rapid growth in the number of papers published in the area due to the scientific and technological relevance of such fundamental physical phenomena. A brief glance over them is enough to comprehend the complexity of what may appear a simple problem at first sight.

In this chapter, the emphasis is on presenting a review with the most important investigations to the subject matter of this thesis rather than attempting a comprehensive review of phase transition or capillarity. To guide the reader, this has been divided into two sections according to the physical configurations investigated in subsequent chapters, namely liquid layers and sessile droplets. Nonetheless, it should be noted that many of the principles can be extrapolated independently of the geometry.

2.1 Liquid Layers

The interests in thermocapillary flows and instabilities formally commenced at the beginning of the 20^{th} century when Bénard [25] performed a series of experiments, in which a horizontal liquid layer was subjected to a vertical temperature gradient, and found regular cellular convection patterns (Bénard cells). Motivated by this work, some years later

Lord Rayleigh [26] completed a fundamental theoretical study focusing on instabilities of liquid layers due to buoyancy which explained Bénard cells via density variations. Later investigations [27, 28, 29] showed that surface tension rather than buoyancy controls the convection cells in shallow liquid layers, nonetheless.

Pearson [28] examined drying paint films and pointed out the presence of steady convective cells of similar to those observed by Bénard even when the free surface was inverted and, therefore, the gravity vector was effectively reversed. Since the instabilities seemed unaffected by the direction of gravitational field, Pearson concluded that these patterns could not be explained by means of density gradients and proposed surface tension as the principal driving force, i.e. the Marangoni effect. Following a similar approach to that performed by Lord Rayleigh [26], Pearson [28] carried out a linear stability analysis on a horizontal liquid layer of depth $\hat{d}$ subjected to the vertical temperature gradient resulting from the supply of heat to the lower plate. He regarded surface tension $\hat{\sigma}$ as a linearly decreasing function of temperature, $\hat{\sigma} = \hat{\sigma}_0 - \hat{\gamma}\left(\hat{T} - \hat{T}_0\right)$ with $\hat{\gamma}$ = -$\partial\hat{\sigma}/\partial\hat{T}$, ignored the effects of the gas, assumed a fixed non-deformable interface and isolated capillary convection from buoyancy by neglecting gravity. Pearson expressed the critical conditions for the onset of convective instabilities by means of the Marangoni number $Ma = \hat{\gamma}\hat{b}\hat{d}^2/(\hat{\mu}\hat{\alpha})$, although he referred to it as the generic dimensionless number B, where $\hat{b}$ is the thermal gradient and $\hat{\mu}$ and $\hat{\alpha}$ are the dynamic viscosity and thermal diffusivity of the liquid, respectively. Scriven & Sterling [29] extended Pearson's stability analysis by taking into account free-surface deformations and provided a criterion to distinguish whether buoyancy or surface tension dominate cellular convection in liquid pools. By accounting for the possibility of shape deformations of the free surface, Scriven & Sterling concluded that there is no critical Marangoni number for the onset of stationary instability and that the limiting case of 'zero wave-number' is always unstable [29].

Motivated by the experimentally-observed temperature and velocity fluctuations in crystal-growth melts reported by Schwabe *et al.* [9] and Schwabe & Scharmann [12], Smith & Davis [11, 30] employed linear theory to examine the stability of the surface-tension-driven convection generated by a constant horizontal temperature gradient in a shallow fluid layer with a free upper surface. In the first part of their work [11], Smith

& Davis regarded the free-surface as non-deformable and neglected the dynamics of the gas phase. The liquid is bounded from below by an adiabatic rigid plane and there are no body forces. Heat transfer across the interface is controlled through the Biot number $B = \hat{h}\hat{d}/\hat{k}$, where $\hat{h}$ is the heat transfer coefficient, $\hat{d}$ is the layer thickness, and $\hat{k}$ is the liquid thermal conductivity. The authors considered two different planar geometries whose basic-state solutions are referred to as the *linear-flow* solution (infinite liquid layer) and the *return-flow* solution (two-dimensional slot). Smith & Davis [11] showed that, for sufficiently large horizontal temperature gradients, the flow may become unstable and exhibit steady longitudinal rolls or unsteady hydrothermal waves (hereafter referred to as HTWs). The former is basically the classical instability studied by Pearson [28], whereas the latter represents a different new mode of instability. Smith & Davis also used the Ma number to define the onset of the instabilities and, analogously to Pearson [28], discovered that the most unstable configuration is always that wherein there is no heat loss across the interface, i.e. $B = 0$. For the *linear-flow* solution, the preferred mode consists of two HTWs propagating at angles $\pm\psi$ with respect to the axis opposite to the direction of the surface flow when $Pr < 0.60$; a single two-dimensional HTW propagating in parallel to the basic state flow when $0.60 < Pr < 1.60$ and stationary longitudinal rolls for $Pr > 1.60$; here $Pr = \hat{\mu}\hat{c}_p/\hat{k}$ corresponds to the Prandtl number and $\hat{c}_p$ is the specific heat capacity. In the *return-flow* configuration the preferred mode is always a HTW propagating upstream at angles $\pm\psi$ with respect to the axis opposite to the direction of the surface flow. The angle of propagation for oblique HTWs is solely a function of Pr.

In the second part of their investigation, Smith & Davis [30] focused on a different family of thermocapillary instabilities, the so-called *surface-wave* instabilities, whose mechanism is critically connected to notorious interface deformations. Since this investigation is primarily interested in the HTWs, we do not go into the details of this new topic and refer the reader to [30] for further information. An extensive review on thermocapillary instabilities was performed by Davis [31]. In a subsequent paper, Smith [32] described the physical mechanisms of the new HTW instability reported in [11]. At small Pr numbers, the HTWs extract their energy from the externally-imposed horizontal temperature gradient by the streamwise flow. At large Pr numbers, on the other hand, the

energy is obtained from the flow-induced vertical temperature field by vertical convection [32].

It is worth highlighting the work of other authors who extended the theoretical study by Smith & Davis [11] to account for buoyancy effects, namely Garr-Peters [33, 34]; Parmentier *et al.* [35]; Mercier & Normand [36] and more recently Chan & Chen [37]. Parmentier *et al.* [35] confirmed the always stabilizing effect of viscosity and noticed that the system's behaviour was decisively connected to the Pr number. These authors concluded that it could only be guaranteed that buoyancy destabilises the flow when $Pr > 2.6$. However, if $Pr < 0.4$, the effect is inverted and gravity tends to stabilise the system. Mercier & Normand [36] investigated the transition between stationary and oscillatory modes, which depends on the relative importance of buoyancy and capillary forces, and reported two new types of oscillatory modes presenting significant differences with the predictions by Smith & Davis [11]. Very recently Chan & Chen [37] observed a slight increment in the angle of propagation when the effect of gravity is weak until an inflexion point from which the angle decreases steadily to zero for stronger body forces, i.e. it was concluded that as the effect of gravity is increased, the oblique mode of instability is replaced by instabilities in the transverse mode. The phase-speed and wavelength decrease constantly as the role of gravity becomes more predominant.

Numerous experimental investigations have been carried out in rectangular pools to study thermocapillary- and buoyancy-driven instabilities but only few of them provide conclusive proof of the existence of HTWs predicted by Smith & Davis [11]. Here, only the most relevant studies are discussed, the reader is referred to Schatz & Neitzel [38] and Burguete *et al.* [39] for more detailed reviews. Riley & Neitzel [40] argued that, due to buoyancy and geometric effects, previous experimental studies do not provide a definitive proof for the existence of the HTWs. Hence, they conducted a series of experiments in a laterally-heated rectangular geometry, considering very thin liquid layers of 1 cSt silicone oil, $\hat{d} = 0.75 - 2.5$ mm, and reported observing pure HTWs presenting good agreement with Smith & Davis [11] for $\hat{d} \leq 1.25$ mm. Burguete *et al.* [39] performed similar experiments in a wider rectangular cavity with 0.65 cSt silicone oil. These authors also considered a larger range of liquid heights, $\hat{d} = 0.5 - 10$ mm, and investigated the influence

of the geometrical aspect ratios. Burguete *et al.* observed oblique HTWs and longitudinal stationary rolls for small, $\hat{d} \leq \hat{h}_r$, and large, $\hat{d} > \hat{h}_r$, fluid depths, respectively. Within the HTW regime, for larger heights, $\hat{h}_c < \hat{d} < \hat{h}_r$, the HTW source is a line and generally evolves towards one end of the container leaving a single wave, whereas for smaller heights, $\hat{d} < \hat{h}_c$, the source looks like a point and emits a circular wave which becomes almost planar farther from the source in both directions. In accordance with Smith & Davis [11], Burguete *et al.* [39] found the HTW instability to be convective. The transition liquid depths, $\hat{h}_r$ and $\hat{h}_c$, are found to be dependent on cavity's aspect ratio. Due to its paramount importance for the semiconductor industry, several laboratory investigations on HTWs have also been carried out with radially-heated annular geometries recreating the conditions encountered in the Czochralski method of crystal growth. Schwabe *et al.* [41], Schwabe *et al.* [14] and Garnier *et al.* [8] reported spiral-like HTW trains consistent with the theory by Smith & Davis [11], the HTW deformations result from the annular geometry.

With the aims of contrasting previous theoretical and experimental works as well as providing further characterizations of thermocapillary driven flows, HTWs have also been studied by means of numerical simulations. Xu & Zebib [42] conducted 2D and 3D numerical investigations on rectangular cavities for fluids with $1 \leq Pr \leq 13.9$ and obtained neutral stability diagrams. In 2D, the authors also provided results illustrating the influence of the driving force, surface-tension gradients, and streamwise length aspect ratio on the flow structure. In 3D, their attention was focused on the influence of the sidewalls which, in general, had a damping effect on the oscillation. Bucchignani [43] investigated numerically the flow represented by the experiments of Riley & Neitzel [40] on shallow silicone layers, $\hat{d} = 1$ mm. This author reported temperature and velocity oscillatory perturbations consistent with the observation of pure HTWs. Following from the investigation by Schwabe *et al.* [14] on board of the satellite FOTON-12, several analogous numerical works have been carried out on annuli [44, 45, 46, 47, 48, 49]. Some of these authors also investigated other families of instabilities found when the liquid depth is increased, i.e. when buoyancy becomes the leading force.

All of the aforementioned numerical studies employ a qualitatively similar methodo-

logy which shares the same simplifications. The authors completely ignored the gas phase above the liquid layer, used a single-phase model whose upper boundary is regarded as non-deformable (with the exception of the stability analyses by Scriven & Sterling [29] and Smith & Davis [30]) horizontal free-surface and, if considered, modelled the heat transfer across the interface via the Biot number and the temperature jump between the free surface and a reference temperature; in most cases the reference temperature is taken to be a constant with the exception of Mercier & Normand [36] who considered instead a profile that varies linearly in the streamwise direction, and Mancho & Herrero [50] who took into account the effect of lateral heating walls.

An important aspect of this problem, that seems to have been ignored so far, is the effect of evaporation. It is well known that even in the absence of an externally-imposed temperature gradient, evaporating thin films may become unstable due the spontaneous development of temperature gradients as energy is transported through the film to the interface to provide the latent heat for evaporation, e.g. see [51, 52, 53, 54, 55]. Much earlier, Palmer [56] showed how the vapour recoil force in rapidly evaporating liquids could also destabilise a thin layer. However, all these works were concerned with interfacial instabilities only, i.e. interface deformations. To date, there is no investigation in the literature assessing the effects of phase change in the thermocapillary instabilities, i.e. HTWs, even though there have been experimental works focusing on these where special care was required to either estimate or to counteract the effects of evaporation, e.g. the ground-based experiments conducted by Schwabe *et al.* [41] and Riley & Neitzel [40] or the μ-gravity investigation by Schwabe *et al.* [14]. Phase change plays an important role in a great variety of applications and naturally has been the subject of numerous theoretical studies in the literature with a renewed interest in the last decade. Detailed reviews can be found in Kanatani & Oron [57] and Guo & Narayanan [58]. An important simplification that has been used extensively in the literature is based on the assumption that the vapour density, viscosity and thermal conductivity are much smaller than those of the liquid [59, 60, 61, 62, 63]. This assumption decouples the dynamics of the two phases allowing to concentrate solely on the liquid phase; this model is often called the "one-sided" approximation.

It should be noted that the use of the "one-sided" model can be quite restrictive. As it was shown by Deegan *et al.* [20, 21], in some cases the vapour phase cannot be ignored and must be taken into account, e.g. when evaporation is limited by diffusion of vapour in air. This has led several researchers to adopt a "two-sided" approach by fully accounting for the dynamics of the vapour phase [53, 64, 54, 65, 58, 57]. This is also the type of approach that will be followed in the present investigation. To the best of my knowledge, this work constitutes the first investigation that studies the effects of phase-change on the emergence of HTWs taking into account the dynamics at the interface and of the flow and concentration field in the gas phase.

2.2 Sessile Drops

The emergence of HTWs in a slightly different system was recently discovered by Sefiane *et al.* [66], who experimentally reported self-excited thermocapillary instabilities in sessile droplets evaporating into normal air. Employing infrared thermography, these authors studied the phase change process of drops of a number of liquids with different volatilities (water, ethanol, methanol and FC-72) released onto various hydrophilic solid substrates (PTFE, Macor, titanium and copper). As opposed to earlier investigations on HTWs, e.g. [11, 39, 14], where the thermal gradients responsible for the flow motion were externally imposed, these appear naturally in the drops due to the nonuniform evaporation flux along the interface. Sefiane *et al.* [66] observed temperature wave trains travelling in the azimuthal direction in ethanol and methanol drops consistent with the instabilities previously predicted by Smith & Davis [11] for planar layers. The wavenumber k was found to decrease almost linearly during the course of the evaporation process due to the variation in the drop thickness. This was reported in the range $k \sim 40 - 5$. The characteristics of the HTWs seemed critically affected by the thermal conductivity of the substrate observing substantially larger numbers of waves associated with the more conductive substrates. In terms of the angle of propagation, reported in the range $\psi \sim 11^\circ - 28^\circ$, this also increased with the substrate's conductivity as well as with Pr. In contrast to what happens for methanol and ethanol droplets, FC-72 droplets displayed

an interface thermal motion characterised by cell-like patters emerging near the apex and travelling radially towards the contact line. These appear to resemble more Bénard-like instabilities rather than HTWs.

A number of investigations have followed from that by Sefiane and co-workers [66]. Sefiane *et al.* [67] further studied the dependence of the HTWs on the substrate by examining the impact of its temperature. The non-isothermal configuration revealed that even relatively weak levels of superheat, $+4\,^{\circ}\mathrm{C}$, could significantly increase the resulting wavenumber. Brutin *et al.* [68] and Sobac & Brutin [69] also carried out experiments considering the non-isothermal case. The latter additionally investigated the effects of the initial volume and observed that the number of waves decreased with time according to a power law rather than linearly as it had been previously reported by Sefiane *et al.* [66]. Explanations of the difference between these evolutions can be found in the difference of experimental conditions: in the thermal resistances of the substrates or in the triple-line dynamics (pinned or receding) [69]. Carle *et al.* [70] compared the spontaneous growth of HTWs in ethanol drops deposited onto a constant-temperature substrate under terrestrial gravity and the μ-gravity levels provided by parabolic flights. The results seemed weakly affected by the magnitude of the gravitational field and confirmed the thermocapillary nature of these instabilities. Very recently, Sefiane *et al.* [71] developed a new experimental set-up which allowed simultaneous recording of the thermal motion in the liquid-gas and liquid-solid drop interfaces as well as computing the local heat flux through the heated substrate. Their findings provided experimental evidence that the thermocapillary instabilities are bulk phenomena, whose effects are felt throughout the drop volume and even alter the solid heat-transfer distribution. Karapetsas *et al.* [72] examined the stability of these drops by performing a linear stability analysis using the "one-sided" approach and invoking the quasi-steady-state approximation. They showed that evaporation induced a horizontal thermal gradient which gave rise, under certain conditions, to HTWs resembling those reported by Sefiane *et al.* [66]. The results of their energy analysis indicated that the mechanisms that are responsible for these waves are the same as those described by Smith [32].

The interest in evaporating sessile droplets started much earlier, nonetheless. The

number of investigations available in the literature is enormous. Here, only the most relevant to the subject of the present work will be highlighted. The reader is referred to Dunn *et al.* [73], Cazabat & Guena [74], Brutin *et al.* [68] and Erbil [75] for recent and comprehensive reviews on this matter. In addition, in what follows this review will be restricted to investigations of relatively slow evaporating drops in which the surface is saturated and the transport of vapour away from the drop is the rate-limiting mass-transfer mechanism. It should be noted that there is another body of work concerning the rather different situation of more rapidly evaporating liquids showing discontinuities at the interface. In this case, the evaporation flux is normally calculated through the application of classical kinetic theory to non-equilibrium effects at the interface. Representative investigation on this matter are those by Burelbach et al. [63], Anderson & Davis [76] or Ajaev [77].

A milestone work was achieved by Picknett & Bexon [78] who experimentally and theoretically investigated this problem in the late '70s. They addressed the two extreme modes of evaporation, namely constant angle (CA) and constant radius (CR) modes. In the former the droplet evaporates with a receding contact radius $\hat{R}$ while the contact angle remains fixed $\theta = \theta_0$. In the latter, the contact angle θ decreases with time while the base radius remains pinned $\hat{R} = \hat{R}_0$. Picknett & Bexon [78] observed that the instantaneous drop mass varies linearly and according to a power law when the drop evaporates in the CR and CA modes, respectively. They also examined the lifetime of the drop depending on the initial (equilibrium) contact angle θ_0 concluding that, in general, for the same θ_0 the lifetime of a drop evaporating in the CR mode is shorter than that of same drop if it were evaporating in the CA mode. Only when the level of hydrophobicity is very high, $\theta > 140°$, this behaviour is inverted. Bourgès-Monnier & Shanahan [79] conducted more experiments to study the impact of the substrate's roughness and showed that a droplet could also evaporate in a more complicated fashion mixing CR and CA modes. This mechanism is usually referred to as stick-slip (SS) mode. Theoretically, they focused their attention on the CR stage and obtained an approximate solution for the total mass flux across the droplet surface.

Significant insights into the dynamics of sessile drops were provided by Deegan *et al.*

[20, 21] in their investigation of the so-called "coffee-ring" effect, i.e the patterns left by thin pinned drops when the evaporating liquid is a suspension of colloidal particles. This was explained via the radial outward flow induced to replenish the liquid eliminated by evaporation from the edge of the drop. Hu & Larson [18] adopted the evaporation flux distribution along the droplet surface presented by Deegan *et al.* [21] and, with the help of their numerical results, suggested approximate analytical expressions to determine the evolution in time of this and of the evaporation rate as a function of the contact angle θ, in the range $\theta = 0 - 90°$. The authors compared their results with experiments, numerical simulations and the theory by Picknett & Bexon [78] finding reasonably good agreement without parameter fitting. Subsequently, Hu & Larson [80, 81] neglected inertial effects and employed lubrication theory to investigate the flow field within the drops, first without Marangoni stresses [80] and then accounting them [81]. The lubrication approximation restricted the validity of their analysis to $\theta < 40°$. Following from these works, Hu & Larson [82] also showed that spontaneously evaporation-induced thermocapillarity could invert the the typical coffee-ring depositions, therefore, driving the suspended particles to the centre of the drop rather than towards the contact line. Ristenpart *et al.* [83] concluded that the direction of the flow depends on the relative thermal conductivities of the substrate and liquid and provided the critical conditions limiting the outward/inward flow regimes.

Other works important to the subject of this investigation are those by Birdi *et al.* [84] and Rowan *et al.* [85] who conducted experiments showing that the evaporation rate vary with the size of the drops. Also experimentally, Erbil *et al.* [86] reported the more difficult to observe CA evaporation mode in n-butanol, toluene, n-nonane, and n-octane drops on a polytetrafluoroethylene (PTFE) surface with equilibrium contact angle $\theta_0 < 90°$. More work on evaporating drops with receding contact lines was later performed by Poulard *et al.* [87]. The role of the substrate temperature on the wetting and evaporation behaviour of volatile droplets was examined by Crafton & Black [88], with water and heptane drops on aluminium and copper surfaces, and by Mollaret *et al.* [89], with water drops on aluminium and PTFE. David *et al.* [90] showed the strong influence of the evaporation rate on the thermal conductivity of the substrate. This important

finding pointed out deficiencies of previous theoretical models [78, 79, 85, 18], which failed to take this phenomenon into account. Later, Dunn *et al.* [73] provided further insights into this problem by means of experiments and numerical work. Attempts suggesting new theoretical expressions to predict the evaporation rate correcting the deviations due to thermal effects have been recently presented by Sefiane & Bennacer [91] or Sobac & Brutin [92]. Xu & Luo [93] showed the weak Marangoni flow experienced by water drops via fluorescent nanoparticles added to the liquid. Sefiane *et al.* [94] performed experiments to elucidate the effect of the atmosphere on pinned water drops released onto various substrates. They observed that reducing the atmospheric pressure increased the molecular diffusion coefficient of the vapour and, therefore, the evaporation rate. Different evaporation rates were also reported for different ambient gases, namely nitrogen, helium and carbon dioxide. Shanahan *et al.* [95] revised the CA and CR pure modes of evaporation and derived new analytical expressions to demonstrate that the droplet lifetime changes with the hydrophobicity of the substrate. As Picknett & Bexon [78], they also concluded that the CR mode leads to shorter drop lifetimes. In an attempt to investigate the more usual SS mode, Nguyen & Nguyen [96] proposed very recently a more sophisticated theoretical analysis to predict the lifetime of droplets evaporating via a combined pinned-receding mode. Under these conditions, Stauber *et at.* [97] have recently showed that the lifetime of a drop may not always be constrained by the lifetimes of the extreme modes.

A number of investigations have also revolved around the complex pinning-depinning behaviour of the triple line (SS mode), e.g. Sefiane & Tadrist [98], Moffat *et al.* [99] and Orejón *et al.* [100]. The dynamics of this are dictated by a competition between pinning forces on one hand and depinning forces on the other hand. The pinning forces are usually due to the contact line being anchored to the substrate because of chemical and surface heterogeneities, whereas the depinning forces are normally the result of the deviation of the droplet profile from equilibrium [100]. Before these works, Shanahan [101] had already developed a simple theory to explain the jumps characteristic of the SS mode experienced by the drops in the last stages of the evaporation process.

Most of the aforementioned theoretical works essentially focused on predicting the

	Approach[♯]	Gas phase[⋆]	Contact Line[†]	Transient/ Pseudo-transient[‡]	Evap. flux[†]	Geom.[⋕]
Ruiz & Black [102]	FS	N	P	T	MTC	S
Hu & Larson [18]	FS	V(D)	P	PST	D	I
Mollaret *et al.* [89]	FS	V(D)	P	T	D	S
Hu & Larson [80, 81, 82]	FS	V(D)	P	PST	D	I
Girard *et al.* [103]	FS	N	P	PST	MTC	I
Girard *et al.* [104, 105, 106]	FS	T(D)	P	PST	MTC	I
Karapetsas *et al.* [72]	FS	N	M	T	MTC	S
This investigation	TP	F(AD)	P/M	T	AD	S

Table 2.1: Summary with the most relevant numerical works on evaporating sessile drops available in the literature. Legend - ([♯]) Approach - FS: Free surface, TP: Two-phase; ([⋆]) Dynamics of the gas - N: Neglected, T(D): Temperature (Diffusion), V(D): Vapour (Diffusion), F(AD): Full advection-diffusion transport of momentum, temperature and vapour; ([†]) Contact line - P: Pinned, M: Moving; ([‡]) Type of computation - T: Transient, PST: Pseudo-transient (transient solution obtained as a succession of steady-state solutions); ([†]) Computation of the evaporation flux - MTC: Mass-transfer coefficient, D: Vapour diffusion, AD: Vapor advection-diffusion; ([⋕]) Drop geometry - I: Imposed, S: Solution.

evaporation flux and lifetime of the drops regardless of what happens within them, except for Deegan *et al.* [20, 21], Hu & Larson [80, 81, 82], Mollaret *et al.* [89] and Karapetsas *et al.* [72] who also provided some insights into the dynamics of bulk flow by numerical simulations. Other authors have also directed their attention to revealing the underlying mechanisms taking place within the liquid, e.g. Ruiz & Black [102] and Girard and co-workers [103, 104, 105, 106]. At this point, it is important to realise the restrictions that all these numerical works share. To guide the reader, a summary is presented in TABLE 2.1. Firstly, most of these investigation completely neglected the dynamics of the gas phase by addressing the free-surface problem. In some cases the authors used some heat transfer coefficient to approximate the energy balance. Only Girard *et al.* [104, 105, 106] solved Laplace's equation for the temperature in the gas phase to calculate the energy transfer across the free surface in a more realistic manner. Regarding the evaporation flux, this has been computed either via the Laplace solution of the vapour field (Mollaret *et al.* [89], Hu & Larson [18, 80, 81, 82]) or by means of some kind of mass-transfer coefficient (Ruiz & Black [102], Girard *et al.* [103, 104, 105, 106], Karapetsas *et al.* [72]), understanding the latter as some relationship relating the local conditions with

those far away from the free surface. This is an important assumption whose validity is questionable for thermocapillary flows. In these, by virtue of viscosity the Marangoni effect may induce significant convective transport of vapour in the gas parallel to the interface which can alter the evaporation flux distribution. Thus, the full advection-diffusion solution for the vapour concentration (and temperature) in the gas is necessary to verify how the resulting local interface mass-transfer rate (purely calculated based on the local temperature/concentration balance at the interface) compares with that from the diffusion solution.

The reader should also note that very relevant works available in the literature, such as Hu & Larson [18, 80, 81, 82] or Girard *et al.* [103, 104, 105, 106], provided pseudo-transient solutions to the droplet development in time, i.e. their transient evolution are the sum of a set of steady-state solutions rather than the result of a pure transient approach as that by Ruiz & Black [102], Mollaret *et al.* [89] and Karapetsas *et al.* [72]. Pseudo-transient works additionally required the external imposition of the drop geometry. Thus, these models are suitable neither to capture transient phenomena, e.g. HTWs, nor to study cases wherein interface deformations are relevant, e.g. for larger drops in which gravity is not negligible as those investigated by Gatapova *et al.* [107]. Furthermore, Karapetsas *et al.* [72] is the only work addressing the moving contact line problem. However, they only provide insights for a mixed pinned-receding scenario. It would be desirable an investigation resolving both pure CR and CA evaporation modes to examine how the dynamics compare for the extreme cases, similarly to what Picknett & Bexon [78] did with the overall evaporation rate. A comprehensive review with the state of the art regarding the numerical simulations of flows with moving contact lines has been presented very recently by Sui *et al.* [108]. To conclude, to the best of my knowledge, no direct numerical simulation of evaporating sessile droplets has been yet performed in 3D. Thus, three-dimensional phenomena such as HTWs remain a challenge in terms of direct simulations.

Chapter 3

Liquid Layers under Saturated Environments

This chapter presents a novel model based on the full two-phase governing equations of flow and heat transfer towards understanding thermocapillary instabilities in liquid pools under saturated conditions (without phase change). It is important to note that most previous numerical studies on thermocapillary instabilities employ a range of major simplifications: no gas phase dynamics by virtue of negligible viscosity and thermal conductivity above the liquid (the so-called "one-sided" approach), a non-deformable gas-liquid interface (with the exception of the stability analyses by Scriven & Sterling [29], Smith & Davis [30] and Karapetsas *et al.* [72]), and interfacial heat transfer modelled via the Biot number and governed by the temperature jump between the free surface and a reference bulk liquid temperature.

In order to alleviate these concerns, a novel two-phase model is developed. This permits a more realistic direct numerical simulation (DNS) of thermocapillary flows by solving for the full set of governing equations of flow and heat transfer and including the coupling between liquid and gas phases. The model accounts for interface deformations and addresses the energy exchange between phases solely via the local conditions. The importance of these features is evident with our findings which, among other things, suggest the existence of interfacial deformations coupled with the HTWs as well as a sophisticated mechanism of interface energy transfer previously unnoticed.

The investigation presented in this chapter is also reported in Sáenz *et al.* [109].

3.1 Problem Statement and Formulation

3.1.1 Problem statement

The two-phase thermocapillary flow in a laterally-heated rectangular cavity is investigated by means of DNS. A rectangular pool of length $\hat{l}_x$, width $\hat{l}_y$ and height $\hat{l}_z$ is filled with a liquid layer of depth $\hat{d}$, bounded from above by a gas. The carets identify dimensional quantities. A sketch of the physical system is presented in FIG. 3.1. Both fluids present in the system are incompressible, viscous and immiscible. The density, dynamic viscosity, thermal conductivity, specific heat capacity and coefficient of thermal expansion, i.e. $(1/\hat{\rho})(\partial\hat{\rho}/\partial\hat{T})$, are $\hat{\rho}_l$, $\hat{\mu}_l$, $\hat{k}_l$, $\hat{c}_{pl}$, $\hat{\beta}_l$ for the liquid and $\hat{\rho}_g$, $\hat{\mu}_g$, $\hat{k}_g$, $\hat{c}_{pg}$, $\hat{\beta}_g$ for the gas, respectively. The liquid-gas interface tension $\hat{\sigma}$ is assumed to vary linearly with the temperature $\hat{T}$ according to:

$$\hat{\sigma} = \hat{\sigma}_r - \hat{\gamma}(\hat{T} - \hat{T}_a), \tag{3.1}$$

where $\hat{\gamma}$ = -$\partial\hat{\sigma}/\partial\hat{T}$ is the temperature coefficient of the surface tension and $\hat{\sigma}_r$ denotes the surface tension at the ambient (reference) temperature. The Marangoni effect induced by an externally-imposed thermal gradient in the x-direction, $\left(\hat{T}_h - \hat{T}_c\right)/\hat{l}_x$, gives rise to a capillary flow in the liquid equivalent to that referred to as *return-flow solution* in Smith & Davis [11]. The extreme temperatures are selected in such a way so that the mean value $(\hat{T}_h + \hat{T}_c)/2$ is equal to $\hat{T}_a = 25\,^{\circ}\mathrm{C}$. For now, we consider saturated conditions so that there is no phase change.

The following scalings are introduced to calculate the principal dimensionless variables (without carets),

$$\begin{aligned} \hat{\mathbf{x}} &= \hat{d}\,\mathbf{x}, & \hat{\mathbf{u}} &= \frac{\hat{\gamma}\Delta\hat{T}}{\hat{\mu}_l}\,\mathbf{u}, & \hat{p} &= \frac{\hat{\gamma}\Delta\hat{T}}{\hat{d}}\,p, \\ \hat{T} &= T\,\Delta\hat{T} + \hat{T}_a, & \hat{t} &= \frac{\hat{\mu}_l\hat{d}}{\hat{\gamma}\Delta\hat{T}}\,t, & \hat{\sigma} &= \hat{\sigma}_r\sigma, \end{aligned} \tag{3.2}$$

where $\mathbf{x} = (x,\, y,\, z)$ and $\mathbf{u} = (u,\, v,\, w)$ are the coordinate and velocity vectors with respect

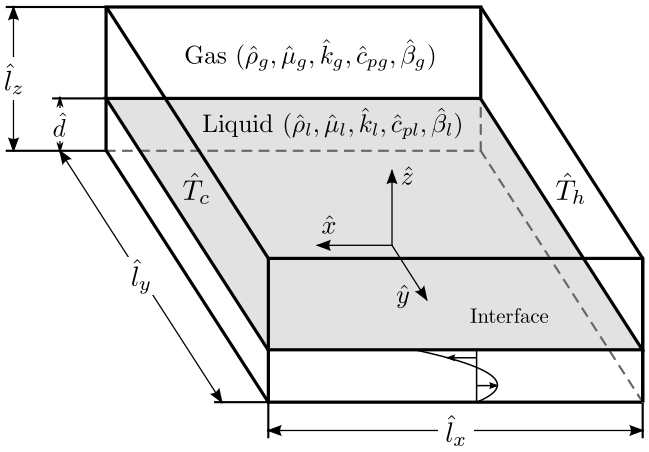

Figure 3.1: Schematic of the planar layer.

to the Cartesian system of coordinates located in the centre of the domain, and p, T and t denote the pressure, temperature and time, respectively. As a result of this change of variables, the following dimensionless parameters arise,

$$Re = \frac{\hat{\gamma}\Delta\hat{T}\hat{d}}{\hat{\mu}_l\hat{\nu}_l}, \quad Fr = \frac{\hat{\gamma}^2\Delta\hat{T}^2}{\hat{g}\hat{d}\hat{\mu}_l^2}, \quad We = \frac{\hat{\gamma}^2\Delta\hat{T}^2\hat{d}}{\hat{\mu}_l\hat{\nu}_l\hat{\sigma}_r}, \quad Bo_d = \frac{\hat{\rho}_l\hat{g}\hat{\beta}_l\hat{d}^2}{\hat{\gamma}}, \quad Pr = \frac{\hat{\nu}_l}{\hat{\alpha}_l}. \tag{3.3}$$

Here, Re, Fr, We, Bo_d and Pr are the Reynolds, Froude, Weber, Bond and Prandtl numbers, respectively, $\hat{\nu}_l = \hat{\mu}_l/\hat{\rho}_l$ and $\hat{\alpha}_l = \hat{k}_l/(\hat{\rho}_l\hat{c}_{pl})$ are the liquid kinematic and thermal diffusivities and $\hat{g}$ is the gravitational acceleration (acting in the negative z-direction). The physical properties of the gas are taken into account by means of the following ratios,

$$\Gamma_\rho = \frac{\hat{\rho}_l}{\hat{\rho}_g}, \qquad \Gamma_\mu = \frac{\hat{\mu}_l}{\hat{\mu}_g}, \qquad \Gamma_k = \frac{\hat{k}_l}{\hat{k}_g}, \qquad \Gamma_{cp} = \frac{\hat{c}_{pl}}{\hat{c}_{pg}}, \qquad \Gamma_\beta = \frac{\hat{\beta}_l}{\hat{\beta}_g}. \tag{3.4}$$

Another important dimensionless group is the Marangoni number. This parameter is traditionally used to quantify the strength of the thermocapillary convection arising for systems with variable interfacial tension such as the one under consideration. The definition of this group as $Ma_L = RePr = \hat{\gamma}\Delta\hat{T}\hat{d}/(\hat{\mu}_l\hat{\alpha}_l)$ is not adequate to interpret the HTWs observed in this investigation since it assumes a constant overall temperature gradient along the interface, $-\mathrm{d}\hat{T}/\mathrm{d}\hat{x} = \Delta\hat{T}/\hat{l}_x$. As discussed in section 3.2 (and also other works such as [40, 39]), the consideration of a finite domain leads to the formation of thermal boundary-layers at the end-walls in the streamwise direction. Consequently, the *interior* or *effective* thermal gradient, denoted by $\hat{b}_i = -\mathrm{d}\hat{T}/\mathrm{d}\hat{x}$, is often much smaller

than the overall gradient, i.e. $\hat{b}_i \ll \Delta\hat{T}/\hat{l}_x$. Burguete *et al.* [39] experimentally report changes up to $\hat{b}_i \cong 0.2\Delta\hat{T}/\hat{l}_x$. For this reason, $\hat{b}_i$ is computed *a posteriori* and used to calculate the *effective* Marangoni number Ma, comparable to that in Smith & Davis [11], as follows,

$$Ma = \frac{\hat{\gamma}\hat{d}^2\hat{b}_i}{\hat{\mu}_l\hat{\alpha}_l}. \tag{3.5}$$

3.1.2 Governing equations

The Volume-of-Fluid (VOF) method is used to compute the dynamics of the two-phase system under consideration. This is a well-established technique that has been used with success by several researchers in the past for the study of other thermocapillary driven flows [110, 111, 112]. Comprehensive descriptions of this method can be found in [113, 114]. The deformable interface is regarded as a diffuse region of finite thickness, $O\left(3\Delta z\right)$, and its position is tracked by solving the advection transport of a scalar variable (colour function). In this case, the colour function selected is the liquid volume fraction c, defined as the volume of liquid in a cell divided by the total volume of the cell. Hence,

$$c = \begin{cases} 1, & \text{cells filled with liquid,} \\ 0, & \text{cells filled with gas.} \end{cases} \tag{3.6}$$

The interface is the transition region where $0 < c < 1$. The VOF method treats both phases, liquid and gas, as a single fluid whose physical properties vary spatially according to c. The one-fluid form for the density ρ, viscosity μ, conductivity k and coefficient of thermal expansion β are volume-averaged, whereas the heat capacity c_p is mass-averaged, i.e,

$$\begin{aligned} \rho &= c + (1-c)/\Gamma_\rho, \\ \mu &= c + (1-c)/\Gamma_\mu, \\ k &= c + (1-c)\,/\Gamma_k, \\ \beta &= c + (1-c)/\Gamma_\beta, \\ c_p &= \frac{c + (1-c)\,/\left(\Gamma_\rho\Gamma_{cp}\right)}{c + (1-c)\,/\Gamma_{cp}}. \end{aligned} \tag{3.7}$$

The volume fraction is transported across the domain by the conservation equation,

$$\frac{\partial c}{\partial t} + \nabla \cdot (c\mathbf{u}) = 0. \tag{3.8}$$

In a two-phase system only one conservation equation needs to be solved as the volume fraction for the gas phase is simply $(1 - c)$. This formulation allows computing both Newtonian fluids using the divergence-free condition (continuity equation) and a single set of momentum equations, i.e.,

$$\nabla \cdot \mathbf{u} = 0, \tag{3.9}$$

$$\frac{\partial (\rho \mathbf{u})}{\partial t} + \nabla \cdot (\rho \mathbf{u}\mathbf{u}) = \frac{1}{Re}\left[-\nabla p + \nabla \cdot \mu \left(\nabla \mathbf{u} + \nabla \mathbf{u}^T\right)\right] + \mathbf{f_b} + \frac{1}{We}\mathbf{f_{sv}}. \tag{3.10}$$

The volumetric forces $\mathbf{f_b}$ and $\mathbf{f_{sv}}$ account for buoyancy and surface tension respectively. Riley & Neitzel [40] pointed out that buoyancy in the liquid phase cannot be disregarded if one aims to provide a conclusive and accurate description of physically-realisable HTWs. Following Boussinesq's approximation, the basic idea of the approach used here is to consider constant the density of the pure substances, $\hat{\rho}_l$ and $\hat{\rho}_g$, everywhere in the momentum equation except for the gravity term, where the densities are approximated by linear functions of $\hat{T}$. The application of this approach results in the dimensionless volumetric force,

$$\mathbf{f_b} = \text{-}\rho \left(\frac{1}{Fr} - \frac{Bo_d}{Re}\beta T\right) \mathbf{e_z}, \tag{3.11}$$

where $\mathbf{e_z}$ is the unit vector in the vertical direction. Note that this expression reduces to $\mathbf{f_b} = \text{-}(1/Fr - Bo_d\, T/Re)\mathbf{e_z}$ in the bulk of the liquid ($c = 1$) and to $\mathbf{f_b} = \text{-}(1/\Gamma_\rho)[1/Fr - Bo_d\, T/(Re\, \Gamma_\beta)]\mathbf{e_z}$ in the gas ($c = 0$), which in dimensional terms is $\hat{\mathbf{f}}_\mathbf{b} = \text{-}[\hat{\rho}_l - \hat{\rho}_l\hat{\beta}_l(\hat{T} - \hat{T}_a)]\hat{g}\mathbf{e_z}$ and $\hat{\mathbf{f}}_\mathbf{b} = \text{-}[\hat{\rho}_g - \hat{\rho}_g\hat{\beta}_g(\hat{T} - \hat{T}_a)]\hat{g}\mathbf{e_z}$, respectively.

Surface tension effects are incorporated in the momentum balance by means of the Continuum Surface Force (CSF) model formulated by Brackbill *et al.* [115]. Contrary to other sharp-interface approaches where the surface tension is a superficial force applied as a discrete boundary condition, the essential idea underlying the CSF model is the computation of the surface tension as a smoothly-varying volumetric force acting on the transition region between phases. The momentum balance at the liquid-gas interface

yields the classical surface tension force per unit of interfacial area,

$$\mathbf{f_{sa}} = \sigma\kappa\mathbf{n} + \nabla_{\mathrm{s}}\sigma, \tag{3.12}$$

where $\kappa = -(\nabla_{\mathrm{s}} \cdot \mathbf{n})$ denotes the interface curvature, $\mathbf{n} = \nabla c / |\nabla c|$ is the unit vector normal to the interface pointing from the gas to the liquid and $\nabla_{\mathrm{s}} = \nabla - \mathbf{n}(\mathbf{n} \cdot \nabla)$ is the gradient operator tangent to the interface. The first term in (3.12) represents the force normal to the interface proportional to the surface tension coefficient and the curvature, i.e. Laplace's formula. The second term is a force tangent to the interface that arises only in cases in which the surface tension varies spatially giving rise to thermocapillary-driven flows. In dimensionless form, the linear dependency between σ and T, previously presented in equation (3.1), takes the form,

$$\sigma = 1 - Ca\,T, \tag{3.13}$$

where Ca is the capillary number defined as $Ca = \hat{\gamma}\Delta\hat{T}/\hat{\sigma}_r$. The reader should note that Ca is not a new independent dimensionless number and can be obtained as $Ca = We/Re$. In accordance with the CSF model, the force per unit interface area $\mathbf{f_{sa}}$ is converted into a force per unit volume $\mathbf{f_{sv}}$ via $\delta = |\nabla c|$, which takes a finite value at the interface and zero elsewhere, i.e.,

$$\mathbf{f_{sv}} = (\sigma\kappa\mathbf{n} + \nabla_{\mathrm{s}}\sigma)\,\delta. \tag{3.14}$$

Substitution of equation (3.13) in the tangential term in (3.14) yields,

$$\mathbf{f_{sv}} = (\sigma\kappa\mathbf{n} - Ca\,\nabla_{\mathrm{s}}T)\,\delta. \tag{3.15}$$

Combination of equations (3.10), (3.11) and (3.15) and small rearrangements in the surface-tension term yield the final expression of the momentum equation,

$$\begin{aligned}\frac{\partial(\rho\mathbf{u})}{\partial t} + \nabla\cdot(\rho\mathbf{u}\mathbf{u}) &= \frac{1}{Re}\left[-\nabla p + \nabla\cdot\mu\left(\nabla\mathbf{u} + \nabla\mathbf{u}^T\right)\right] - \rho\left(\frac{1}{Fr} - \frac{Bo_d}{Re}\beta T\right)\mathbf{e_z} \\ &\quad + \left(\frac{1}{We}\sigma\kappa\mathbf{n} - \frac{1}{Re}\nabla_{\mathrm{s}}T\right)\delta. \end{aligned} \tag{3.16}$$

The model is completed with the equation for the conservation of heat in its temperature form. Since the flow under consideration is very slow, pressure and viscous dissipations are negligible and the governing equation can be written as follows,

$$\frac{\partial\left(\rho c_p T\right)}{\partial t} + \nabla\cdot\left(\rho c_p T\mathbf{u}\right) = \frac{1}{RePr}\nabla\cdot\left(k\nabla T\right). \tag{3.17}$$

3.1.3 Boundary and initial conditions

The rectangular domain is bounded below by a adiabatic wall and in the streamwise direction by vertical walls at fixed temperatures. These solid boundaries are all impermeable and the no-slip condition is applied for the momentum equation. In dimensionless form, the streamwise $\hat{l}_x$, spanwise $\hat{l}_y$ and vertical $\hat{l}_z$ lengths are taken into account by means of the geometrical ratios,

$$L = \frac{\hat{l}_x}{\hat{d}}, \qquad W = \frac{\hat{l}_y}{\hat{d}}, \qquad H = \frac{\hat{l}_z}{\hat{d}}. \tag{3.18}$$

Hence, we can express the previous conditions in mathematical notation as follows,

$$\mathbf{u} = (0,\,0,\,0) \qquad T = \pm\frac{1}{2} \qquad \text{at} \qquad x = \mp\frac{L}{2}, \tag{3.19}$$

$$\mathbf{u} = (0,\,0,\,0) \qquad \mathbf{e_z}\cdot\nabla T = 0 \qquad \text{at} \qquad z = 0. \tag{3.20}$$

To minimise any end-effects in the spanwise direction, periodic boundary conditions are employed at the sidewalls, $y = \pm W/2$. The upper surface, $z = H$, is assumed to be a constant-pressure, $p = 0$, open boundary which allows flow into and/or out of the domain. A priori unknown, the flow direction is locally calculated based on the direction of the surrounding velocity field. For velocity vectors pointing into the domain, the temperature of the gas is assumed to be at $\hat{T}_a$; whereas for flows leaving the domain, zero gradient conditions for velocity and temperature are applied to close the boundary value problem. This open boundary is, therefore, a mixed Dirichlet-Neumann boundary condition.

Initially, the liquid layer is flat and the initial conditions for the velocity, temperature and pressure fields are those corresponding to the *return-flow solution* in Smith & Davis

[11] with the approximation $\hat{b}_i(\hat{t}=0) = \Delta\hat{T}/\hat{l}_x$. The gas starts at rest with the temperature field characteristic of pure steady-state heat conduction in the streamwise direction, i.e.,

$$\begin{aligned} \mathbf{u} &= \frac{c}{L}\left(\frac{3z^2-2z}{4},\, 0,\, 0\right), \\ T &= \text{-}\frac{1}{L}\left[x + c\frac{RePr}{48L}\left(3z^4-4z^3+1\right)\right], \qquad \text{at} \qquad t=0. \\ p &= c\frac{3x}{2L}, \end{aligned} \tag{3.21}$$

It must be emphasised that these equations represent an approximate initial base state, which will be different from the effective base state (also called as the numerical base state) which is determined once the thermal boundary-layers have been established. For this investigation, the results are not sensitive to the initial conditions because the oscillatory regime is triggered by introducing a very small perturbation only once the flow has reached equilibrium (effective base state). Using other initial conditions, e.g. $\mathbf{u} = (0,\, 0,\, 0)$, $T = \text{-}x/L$, and $p = 0$, only results in more expensive computational efforts to reach the same effective base state.

Wettability effects can also be investigated by defining the contact angle on solid boundaries. The specified angle is then used to calculate the $\mathbf{n}$ for cells contiguous to the walls, which is later used in the computation of both the curvature and the surface tension force. For simplicity, the contact angle is maintained at a constant value in the present work, 90°, leaving more in-depth analysis of wettability effects for future studies.

3.1.4 Numerical method

The governing equations (3.8), (3.9), (3.16) and (3.17) form the set of six Partial Differential Equations (PDEs) with six unknowns (c, u, v, w, p and T). These are solved numerically via the finite-volume method. Derivatives in diffusion terms are approximated by the centred scheme while a second-order upwind scheme is employed for the advection terms. The reconstruction of the interface is accomplished via a classical compressive differencing scheme similar to that of Ubbink [116]. The solution is advanced in time with the implicit second-order backward Euler method. Convergence at each time step is assumed when the root-mean-square (RMS) residual is below the target value $1 \times 10^{\text{-}5}$.

The timestep size is selected so that it is always smaller than the viscous, conductive and Marangoni timescales, i.e. $\Delta\hat{t} < \min(\Delta\hat{x}^2/\hat{\nu}_l,\ \Delta\hat{x}^2/\hat{\alpha}_l,\ \Delta\hat{x}/\hat{u}_0)$. In all the cases presented in this work, the Marangoni timescale, $O(10^{-3}\,\mathrm{s})$, is the leading criterion which is logical given that thermocapillary advection is the system's fundamental driving force. The Marangoni timescale also satisfies the low Courant number criterion necessary for the compressive differencing scheme used. The physical domain is discretized by means of a hexahedral mesh with the scalar variables stored in the cells' centres and the velocities at the cells' faces (staggered grid). Special attention is paid to the correct resolution of the thermal boundary-layers near the fixed-temperature walls. To that end, a biased element distribution with finer resolution near the end-walls is employed. The effects of deficiently resolved boundary-layers are illustrated in more detail section 3.2 along with the mesh dependency test.

3.2 Base State

The dynamics of the system are first investigated by considering whether a steady-state can be attained for the case of a thin liquid layer with $Pr = 13.9$ and a quiescent gas. The geometrical domain is defined by $L = 30$, $W = 50$ and $H = 3$. Tests were also carried out with $H = 4$ and 6 revealing that the results were independent of the domain height for $H \geq 3$. The remaining dimensionless parameters are: $Re = 755$, $Fr = 58.2$, $We = 27.1$, $Bo_d = 0.142$, $\Gamma_\rho = 688$, $\Gamma_\mu = 44.6$, $\Gamma_k = 3.85$, $\Gamma_{cp} = 1.71$ and $\Gamma_\beta = 0.4$. Note that these values correspond to the same stable case studied experimentally by Riley & Neitzel [40] with a 1-mm liquid layer of 1cSt Dow Corning silicone oil, normal air and $\Delta\hat{T} = 8.16\,\mathrm{K}$. The physical properties of these fluids are available in TABLE 3.1. Smith & Davis [11] predict a critical Marangoni number $Ma_{c,SD} = 295$ for this configuration. It should be bear in mind that this value has been obtained from a stability analysis that disregards the stabilizing effects of gravity and heat loss across the interface. Riley & Neitzel [40] report $Ma_{c,RN} = 366$ for the same system but their critical value is calculated from their experimental work under normal gravity and with the liquid layer open to ambient air. Hence, comparison between $Ma_{c,SD}$ and $Ma_{c,RN}$ gives a quantitative evaluation of the

		1 cSt SO (Liquid)	Air	0.65 cSt SO (Liquid)	0.65 cSt SO (Vapour)
ρ	($\mathrm{kg\,m^{-3}}$)	816	1.18	760	7.51
μ	($\mathrm{Pa\,s}$)	8.16×10^{-4}	1.83×10^{-5}	4.94×10^{-4}	6.15×10^{-6}
k	($\mathrm{W\,m^{-1}\,K^{-1}}$)	0.10	0.01	0.10	0.01
c_p	($\mathrm{J\,kg^{-1}\,K^{-1}}$)	1712	1004	2000	1496
β	($\mathrm{K^{-1}}$)	1.34×10^{-3}	3.36×10^{-3}	1.34×10^{-3}	4.76×10^{-3}
σ	($\mathrm{N\,m^{-1}}$)	1.72×10^{-2}		1.54×10^{-2}	
γ	($\mathrm{N\,m^{-1}\,K^{-1}}$)	7.55×10^{-5}		9×10^{-5}	
Δh_v	($\mathrm{J\,kg^{-1}}$)			2.23×10^{5}	
D	($\mathrm{m^2\,s^{-1}}$)			5.60×10^{-6}	
M	($\mathrm{g\,mol^{-1}}$)		28.96	162.38	

Table 3.1: Physical properties of 1cSt and 0.65cSt silicone oils and normal air at $\hat{T} = 25\,^{\circ}\mathrm{C}$ and $\hat{p} = 1\,\mathrm{atm}$.

effects of the theoretical simplifications on the stability of the flow.

In the initial stages, the flow undergoes an adjustment period in which the originally imposed temperature gradient, $\Delta\hat{T}/\hat{l}_x$, is progressively reduced by the effect of the thermal boundary-layers acting at the walls. Once the boundary-layers have been established completely, the system reaches a steady-state wherein velocity and temperature are essentially constant. The steady streamwise temperature profile at the interface is shown in FIG. 3.2a. At this point, the effective temperature gradient for the core region $\hat{b}_i$ remains constant but is smaller than that initially imposed. It must be noted that Smith & Davis [11] did not encounter this due to their unbounded infinite domain. To correctly interpret the results, $\hat{b}_i$ is obtained *a posteriori* and then used in (3.5). Here, it is found that $Ma = 214$, which is lower than $Ma_{c,SD}$ and therefore corresponds to a stable configuration whose liquid bulk flow should be similar to the basic state presented in [11].

TABLE 3.2 shows that convergence is achieved upon mesh refinement. The simulations are run for large number of timesteps, $t \sim 4 \times 10^5$, before crucial system parameters, such as superficial velocity and effective Marangoni number, are read. Due to the small relative difference in these parameters between $73^x \times 121^y \times 59^z$ and $61^x \times 101^y \times 49^z$, 1.33% for u and 2.01% for Ma, the latter mesh is chosen for further simulations.

Grid	Surface velocity	Effective gradient
$73^x \times 121^y \times 59^z$	$u = 5.6 \times 10^{-3}$	$Ma = 218$
$61^x \times 101^y \times 49^z$	1.33%	2.01%
$51^x \times 84^y \times 41^z$	7.23%	3.56%
$43^x \times 70^y \times 34^z$	9.42%	5.58%

Table 3.2: Mesh dependency test for the case presented in section 3.2.

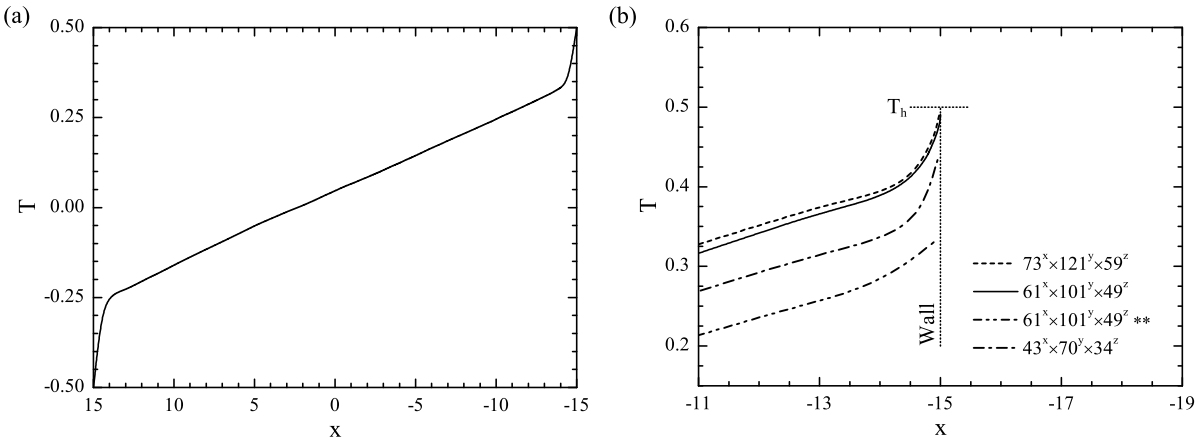

Figure 3.2: (a) Steady surface temperature distribution and (b) resolution of the thermal boundary-layer with $Pr = 13.9$, $Re = 755$, $Fr = 58.2$, $We = 27.1$, $Bo_d = 0.142$, $\Gamma_\rho = 688$, $\Gamma_\mu = 44.6$, $\Gamma_k = 3.85$, $\Gamma_{cp} = 1.71$ and $\Gamma_\beta = 0.4$. The double asterisk (**) denotes a uniform element distribution, i.e. no grid refinement near the walls.

Obtaining well-resolved thermal boundary-layers is vital. FIG. 3.2b illustrates the thermal boundary-layer with mesh refinement. At low mesh densities, it is observed that the temperature of the liquid right next to the hot wall drops from the fixed value, $T = 0.5$. The opposite behaviour is detected near the cold end. This is indicative of a poorly computed boundary-layer resulting in a lower effective thermal gradient at the centre. It was noted that for coarse resolutions, the interior gradient reaches a constant value unaffected by $\Delta\hat{T}$, incorrectly preventing the system from going beyond the critical point and, therefore, from being subjected to any instability mode. The most efficient way to overcome this difficulty is by refining the mesh near the walls. Here, the mesh refinement is such that there are at least 6-9 computational points within the boundary regions.

Although the full 3D case is computed, the resulting flow is independent of the span-wise direction as expected. FIG. 3.3 compares the numerically-obtained base velocity, FIG. 3.3a, and flow-induced temperature, FIG. 3.3b, in the liquid with those from the

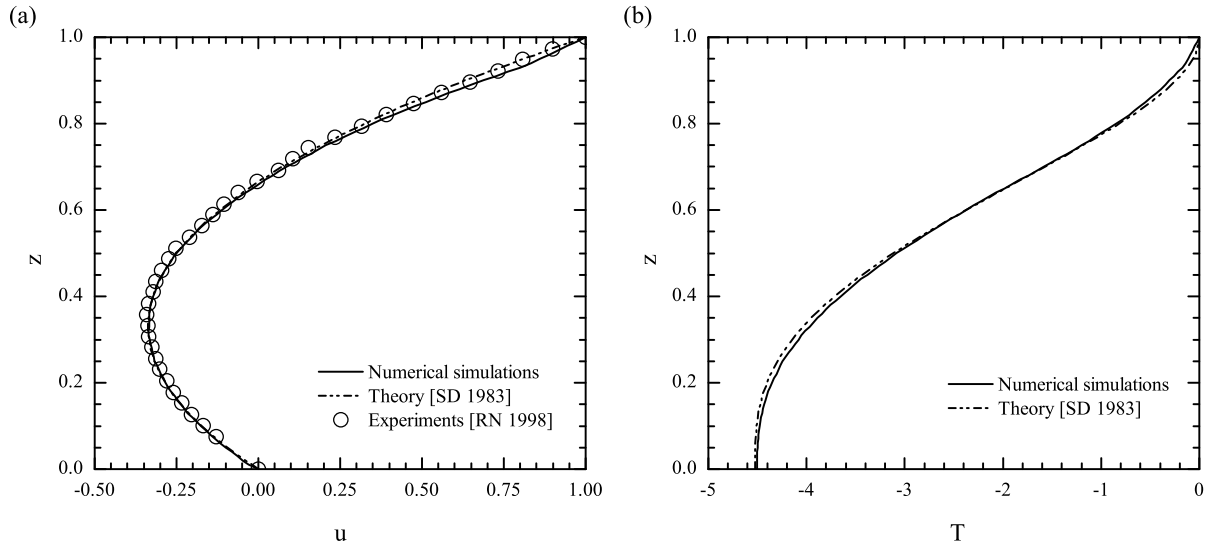

Figure 3.3: Basic-state profiles for the liquid at $(x, y) = (0, 0)$; (a) streamwise velocity (b) flow-induced temperature. The parameters are the same as in FIG. 3.2.

experiments [40], and those used in the stability analysis [11]. This is done at the domain's centre, $y = 0$. Following [40], the velocity profile in FIG. 3.3a has been scaled by the interface value as opposed to the thermocapillary velocity scale. The predicted steady state is, thus, in good agreement for both the velocity and the temperature fields. These results serve as a good validation of the steady properties of the code allowing to continue with a more thorough study of the stability characteristics and the dynamics of this system.

3.3 Hydrothermal Waves

A liquid layer with $Pr = 0.75$ is considered now. This is subjected to a temperature difference between the end-walls large enough to make sure that the effective thermal gradient is supercritical, i.e. the flow is within the unstable regime. The geometrical domain is comparatively smaller only in the spanwise direction, $W = 15$. To allow direct comparison with Smith & Davis [11], the adiabatic-interface case is first investigated. To that end, a specially large thermal conductivity ratio is selected for now, $\Gamma_k = 10^{10}$, which effectively means that the air acts as a thermal insulator. The remaining dimensionless parameters are $Re = 11900$, $Fr = 1720$, $We = 748$, $Bo_d = 0.111$, $\Gamma_\rho = 640$, $\Gamma_\mu = 14$, $\Gamma_{cp} = 2$ and $\Gamma_\beta = 0.4$. These result from considering a 1-mm layer of a liquid similar

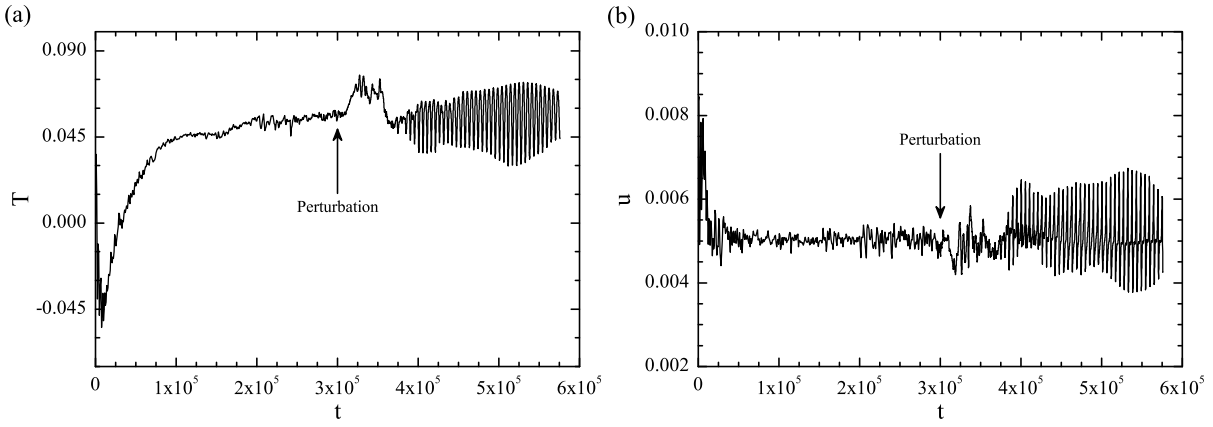

Figure 3.4: Instantaneous (a) interface temperature and (b) flow speed for the adiabatic-interface case with $Pr = 0.75$, $Re = 11900$, $Fr = 1720$, $We = 748$, $Bo_d = 0.111$, $\Gamma_\rho = 640$, $\Gamma_\mu = 14$, $\Gamma_k = 10^{10}$, $\Gamma_{cp} = 2$ and $\Gamma_\beta = 0.4$. The monitoring point $P_o = (0,\, 0,\, z_i)$ is located at the centre of domain on the interface. Insets showing the dynamics of the oscillatory stage are available in FIG. 3.9.

to 0.65 cSt silicone oil, see TABLE 3.1, with the exception of $\hat{\mu}_l = 2.63 \times 10^{-4}$ Pa s and $\hat{k}_l = 0.7$ W m^{-1} K^{-1}. The thermal gradient is $\Delta\hat{T} = 12\,^{\circ}$C. Pure HTWs are only found for capillary flows in which surface tension is dominant over gravity; this condition is met when Bo_d approaches zero or, in dimensional terms, when $\hat{d}$ is smaller than the capillary length. Riley & Neitzel [40] report HTWs for $Bo_d \leq 0.222$ and in the case presented here $Bo_d = 0.111$, thus the same instability mode is expected. The time-step size and the grid resolution are 0.823 and $101^x \times 61^y \times 49^z$, respectively.

3.3.1 Temporal evolution

The overall transient evolution of the system is analysed by recording the time history of the principal variables for the interface, T and $\mathbf{u}$, at the mid-point P_o $(0,\, 0,\, z_i)$ as shown in FIG. 3.4. z_i denotes the interface height. Given the deformable interface, $z_i = z(P_o)$, is part of the transient solution corresponding to the vertical location where $c = 0.5$ with $x(P_o) = y(P_o) = 0$.

FIG. 3.4a shows the instantaneous temperature distribution at the centre of the interface. The capillary flow first undergoes a strong transient period, $t < 10^5$, wherein its surface temperature initially decays but then quickly recovers, reaching a practically steady-value around $T = 0.045$. This minor deviation, 4.5% of the temperature difference between the end-walls, is attributed to confinement effects and is related to the adjustment from the imposed initial conditions presented in equation (3.21) to the numerically-

generated 'base state' wherein the thermal boundary-layers have been established. From $t = 1.6 \times 10^5$ to 3×10^5 no noteworthy change is observed in the flow. At this point, a perturbation of the form $\xi' = A(\xi)\cos(k_x x + k_y y)$ is introduced in the effective base state for T and $\mathbf{u}$. Here, $A(\xi)$ denotes the amplitude for the generic variable ξ, $k_x = k_y/\tan\psi$ and $k_y = k[1+(\tan\psi)^{-2}]^{-0.5}$ are the wavenumbers in x and y, respectively, k is the overall wavenumber and ψ is the angle of propagation. T and $\mathbf{u}$ are perturbed with a dimensionless amplitude of $\Delta\hat{T}/10^3$ and $u_{P_0}/10^3$, respectively. The angle of propagation ψ and overall wavenumber k are those reported by Smith & Davis [11] for the critical mode. In practice, this leads to amplitudes of 5.1×10^{-6} ($\mathbf{u}$) and 10^{-3} (T), $k = 1.52$ and $\psi = 57°$. No distinguishable mode manifests itself until $t = 3.7 \times 10^5$, at which time the effects of the HTWs are first captured. The flow then enters the progressively-growing oscillatory state characteristic of an unstable regime.

Similar conclusions can be drawn from the study of the instantaneous evolution of the velocity for the same point. FIG. 3.4b shows the magnitude of $\mathbf{u}$ throughout the numerical simulation. In this case, it is more difficult to identify the same stages as those reported from the temperature profile. The transient period for the speed is approximately 20% of the thermal and it is followed by a quasi-steady state, from $t = 10^5$ to 3×10^5, in which the velocity experiences small deviations from its mean value $u = 0.0051$. The conversion of this average value to the dimensionless framework by Smith & Davis [11] yields $u = 0.22$ which is in good agreement with the superficial velocity reported by the authors, $u = 0.25$. In this period the spanwise component of the flow velocity does not follow any dominant pattern and it is at least two orders of magnitude smaller than the streamwise component, i.e. no random perturbation has led to the unstable oscillatory regime yet.

FIG. 3.5a illustrates the interface temperature distribution at the centre of the planar geometry, $y = 0$, in the streamwise direction for $t = 5.572 \times 10^5$. At this instant, the flow has already gone deep into the oscillatory phase and has reached a quasi-steady-state wherein the prevailing HTW mode is fully-developed throughout the liquid layer. The thermal boundary-layer is more prominent near the cold wall where it causes a sudden temperature drop of approximately 0.25, double the temperature jump existing near the

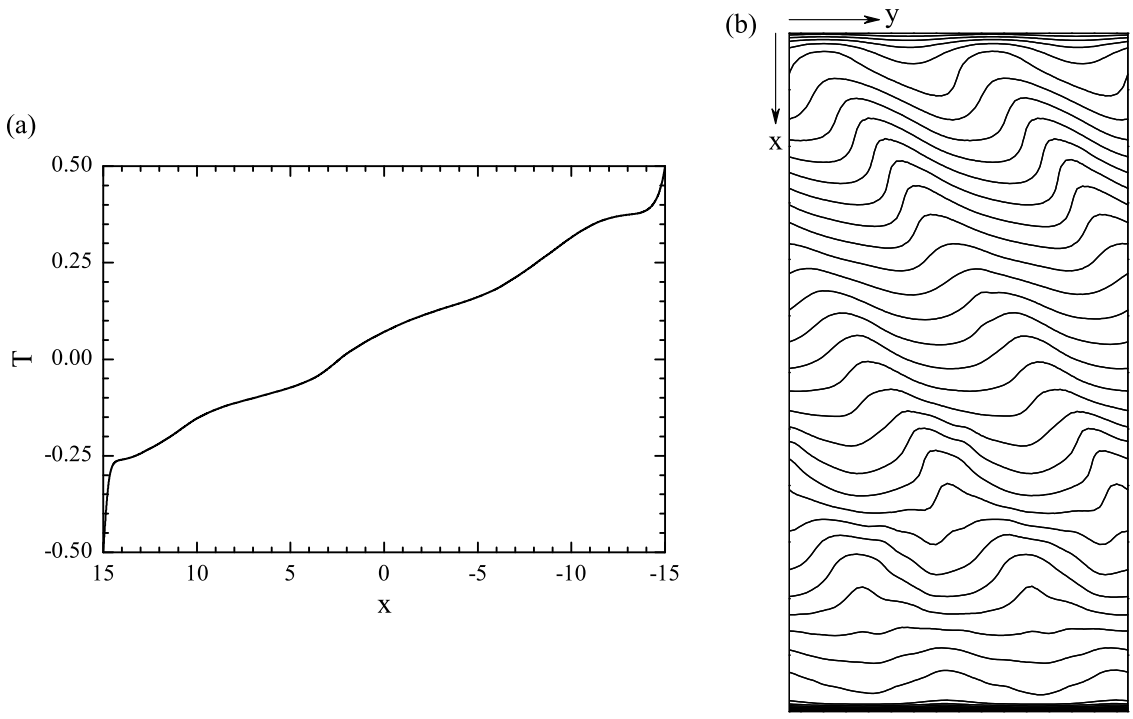

Figure 3.5: (a) Streamwise temperature distribution along the interface for $y = 0$; (b) interface isotherms showing HTWs travelling from the lower-left (cold wall) to the upper-right (hot wall) corner. ($t = 5.572 \times 10^5$). The parameters are the same as in FIG. 3.4.

hot boundary. This difference in extension is provoked by surface flow of hot fluid being transported towards the cold wall due to the Marangoni effect. The temperature profile in the core region presents three wave-like deviations from its average linear value.

The effective Marangoni number is $Ma = 211$, which is higher than the critical value reported by Smith & Davis [11], $Ma_{c,SD} = 96$, for the same liquid and $B = 0$ (adiabatic interface). The corresponding superficial temperature distribution is shown in FIG. 3.5b. The isotherms clearly resemble the shape of the HTWs presenting an oblique pattern. The perturbations travel from the lower-left (cold) towards the upper-right corner (hot) in FIG. 3.5b which is consistent with the results from stability theory that predict HTWs propagating upstream [11, 32].

The HTWs are travelling thermal fluctuations about/around the base state. Thus, to study their transient characteristics, they need to be separated from this state. To that end, for a generic variable $\xi = T$, u, v, w, ω or z_i, the local value of its disturbance ξ',

deviation from the base state, is computed as,

$$\xi' = \xi - \frac{1}{W}\int_{-\frac{W}{2}}^{+\frac{W}{2}} \xi \, \mathrm{d}y. \tag{3.22}$$

The spatial growth of the instabilities is illustrated by several snapshots in FIG. 3.6. Initially, a group of well-defined HTWs grow near the hot wall propagating in the negative x- and y-directions, FIG. 3.6a. This mode, hereafter referred to as *first* HTW mode, is directly related to the most unstable mode in the linear regime predicted by Smith & Davis [11]. These HTWs span around 25% of L when they reach their maximum size and propagate with $\psi = 56°$ with respect to the negative x-axis. Meanwhile the rest of the domain is subject to much weaker disturbances, which are essentially parallel to the x axis. After a certain time, the amplitude of the disturbances grows and the system enters in the non-linear regime. The first HTW mode interacts with other unstable modes leading to a new front of HTWs that appears near the centre of the liquid layer travelling from the lower-left to the upper-right corner of the domain, FIG. 3.6b. At first, these new HTWs grow against the first mode, not being strong enough to disrupt it significantly. However, after a while their amplitude grows and the new waves start to overwhelm the first as shown in FIG. 3.6c. Eventually, the latter perturbation mode dominates the former and the flow reaches an oscillatory state wherein the new HTWs fill the domain completely, FIG. 3.6d. This new group of HTWs, hereafter termed as *prevailing* HTW mode, propagates at $\psi = 55°$ from the negative x-axis.

HTWs can be characterised by their angle of propagation ψ, overall wavenumber k and phase-speed c_R. Smith & Davis [11] obtain these parameters from their linear stability analysis. For the current case, the resulting values are listed in TABLE 3.3 along with those found for the *first* and *prevailing* HTW modes discussed in FIG. 3.6. There is generally good agreement for both cases, particularly for ψ.

It is important to analyse the implications of having periodic boundary conditions in the spanwise direction. This type of condition is employed to minimise the effects of the sidewalls but its use restricts the number of possible HTWs in the y-direction to an integer value. For the case under consideration, the wavenumber in the spanwise

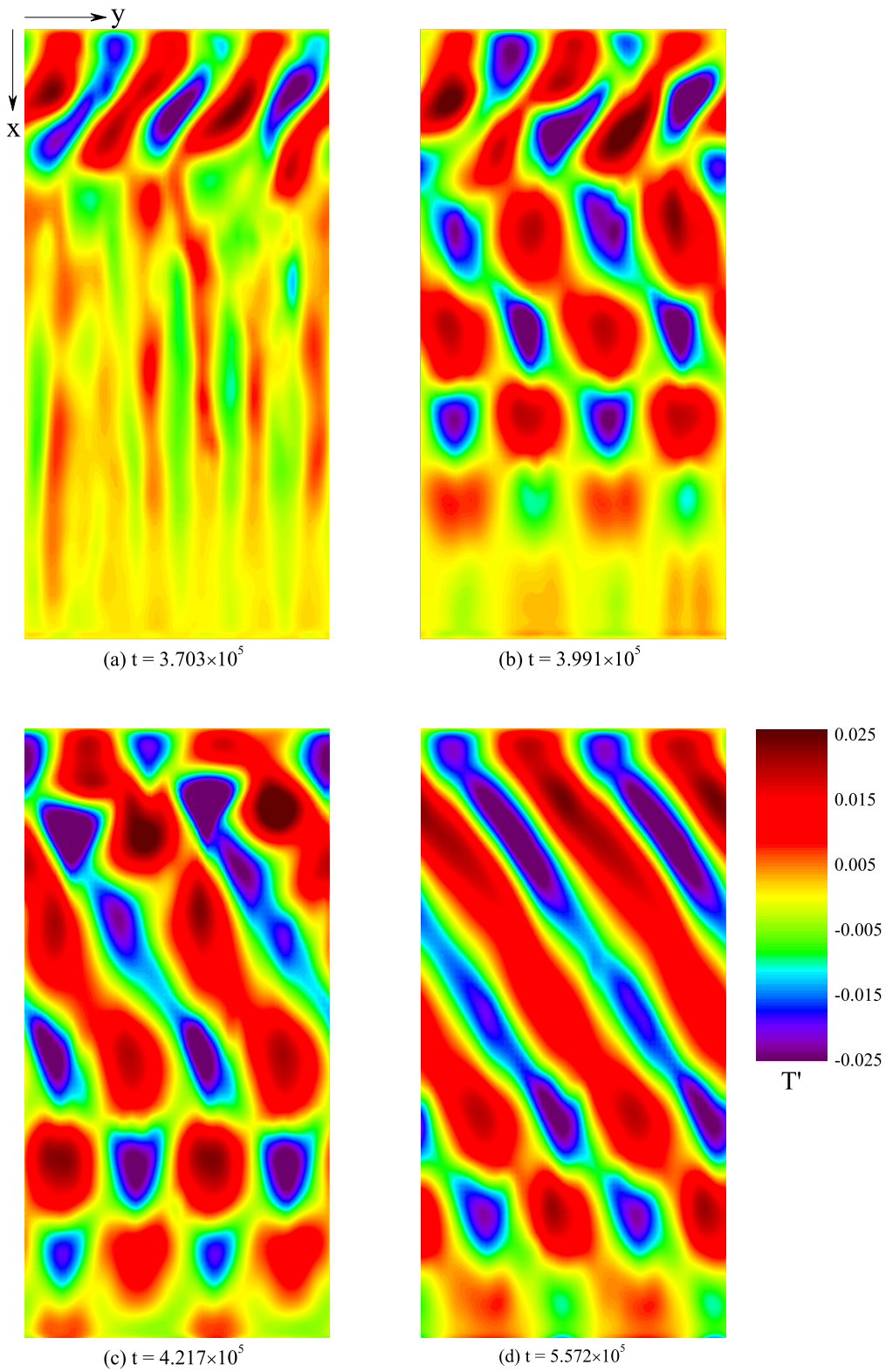

Figure 3.6: Contour plots of interface temperature disturbance T' computed at various points in time showing the spatio-temporal growth of the HTWs. (a) First HTW mode near the hot wall, $t = 3.703\times10^5$; (b) prevailing HTW mode growing stronger in the centre of the domain, $t = 3.991 \times 10^5$; (c) prevailing HTW mode disrupting the first mode, $t = 4.217 \times 10^5$; (d) prevailing HTW mode fully developed propagating towards the upper-right corner at $\psi = 55°$ with respect to the negative x axis, $t = 5.572\times10^5$. The parameters are the same as in FIG. 3.4.

	ψ	k	c_R
Smith & Davis [11]	57°	1.52	0.060
First HTW mode	56°	1.55	0.090*
Prevailing HTW mode	55°	1.04**	0.099*

Table 3.3: Comparison between the HTWs predicted by Smith & Davis [11] and those found in the present investigation for $Pr = 0.75$. First and prevailing modes are those shown in FIG. 3.6. (*Smith & Davis's dimensionless framework, ** This is a non-linear wave).

direction according to Smith & Davis [11] is $\beta = 1.27$, which corresponds to a wavelength of $\lambda_y = 4.95$. The width of the domain is selected so that three of these HTWs can exist, i.e. $W = 3\lambda_y$. The good agreement observed for the first mode indicates that this group of waves are exactly those reported by Smith & Davis [11]. However, as the flow evolves into the non-linear regime, the number of waves in the spanwise direction is only two for the prevailing mode; the overall wavenumber becomes $k = 1.04$ as opposed to 1.52 expected from the linear theory. Although *a priori* conceivable, given that [11] is not rigorously valid within the non-linear stage, the fact that only a discrete set of wavenumbers is possible could indicate that this difference might not be the same for the infinite case. To ensure independence from the boundary conditions and domain's width, the same physical system is computed with $W = 6\lambda_y$. The resulting number of waves for this extended layer is exactly double for both the first and the prevailing modes, FIG. 3.7, confirming independence of the spanwise periodicity. Garnier *et al.* [8], for instance, noted this same effect in their investigation with annular geometries.

In addition to the detailed validation against Smith & Davis [11] as shown above, a brief summary of comparisons against some quasi-numerical studies reported in literature is presented here. Parmentier *et al.* [35] carried out a stability analysis analogous to that of Smith & Davis but including the effect of buoyancy. This is characterised by the Rayleigh number, Ra. For cases with $Pr = 0.1$ and 1 and with $Ra = 23.4$, which corresponds to the configuration considered here, the wavenumber is expected to be between $k \sim 0.7$ for $Pr = 0.1$ and $k \sim 1.1$ for $Pr = 1$. These values suggest an approximate wavenumber $k \sim 1$ for $Pr = 0.75$, which compares better with the prevailing mode than the linear mode suggested by Smith & Davis [11]. The authors also report $\psi \sim 80°$ for $Pr = 0.1$

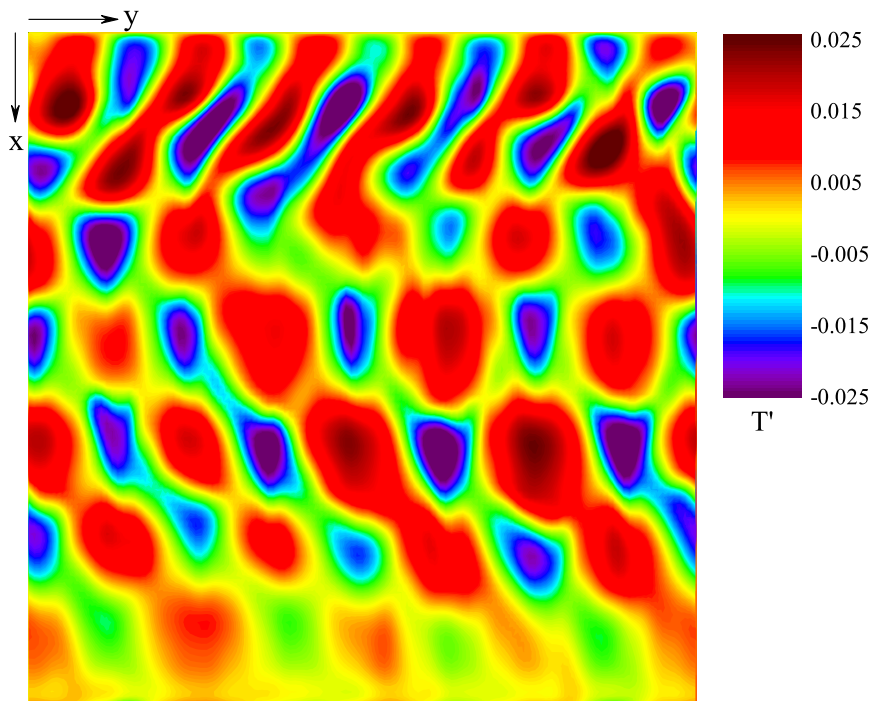

Figure 3.7: First and prevailing HTW modes observed in a wider domain, $W = 30$, with $t = 4.169 \times 10^5$. The rest of the parameters are the same as in FIG. 3.4.

and $\psi \sim 52°$ for $Pr = 1$ resulting in an estimated value of $\psi \sim 60°$ for our liquid; this is in good agreement with the results by Smith & Davis [11] and those presented in this work. Garr-Peters [34] also discussed the effect of gravity for liquids with $0.01 \leq Pr \leq 10$, this time by means of Bo_d. As in the previous case, k and ψ are assessed with the help of the curves available for the two closest liquids for which $Pr = 0.023$ and 2.22. The wavenumber ranges from $k \sim 0.35$ for $Pr = 0.023$ to $k \sim 1$ for $Pr = 2.22$ with an estimated value of $k \sim 0.6$ for $Pr = 0.75$. The angle of propagation is expected to be within the range $\psi \sim 64°$ for $Pr = 2.22$ to $\psi \sim 77°$ for $Pr = 0.023$. Mercier & Normand [36] only considered the case of $Pr = 7$ and controlled the relative importance of buoyancy and thermocapillarity with the ratio $W = Ma/Ra$; here $W = 9$. Comparisons between their analysis and Smith & Davis [11] reveal a slight increment in the wavenumber and a noticeable reduction in the angle of propagation when the effect of gravity is weak. Smith & Davis report $k = 2.58$ and $\psi = 27°$ for $Pr = 7$ and $W = \infty$, gravity is neglected, while Mercier & Normand [36] compute $k = 2.62$ and $\psi = 46°$ for the closest case, $W = 8$. Though the transition between stationary and oscillatory modes experimentally observed by Daviaud & Vince [117] was correctly reproduced by these authors, the angle

of propagation, $\psi \cong 80°$, was not. It must be noted that the cases above ignore the presence of full gas phase dynamics, unlike this work, and mainly deal with much higher Pr than the focus of this investigation. Hence, a detailed comparison with other semi-numerical work is not possible. We now present an in-depth analysis of the linear and non-linear growth of the thermocapillary and interfacial instabilities.

3.3.2 Oscillatory regime

The study of the instability's growth is restricted to the prevailing HTW mode, given that any other linear mode is dominated by it sooner or later. To that end, T' and z_i' are instantaneously computed along the spanwise section at $x = 0$ (midway between the end-walls). In general, the maximum amplitude for either T' or z_i' will be located somewhere alongside this section. The maxima of these disturbances are captured by performing an instantaneous Fast Fourier Transform (FFT) analysis along the mentioned cross-section to make sure that the amplitude of the fundamental mode is captured independently of the spatial location of the maxima. The instantaneous amplitudes for the fundamental sinusoidal modes are presented in FIG. 3.8. Initially, the amplitudes of the three leading modes for both T' and z_i' is approximately equal, FIG. 3.8a-c, denoting that there is no well-defined sinusoidal mode acting in the layer. This behaviour changes at the HTW's onset, around $t = 3.7 \times 10^5$, when the signals start shifting to particular modes. Once the flow is fully-developed, the HTWs are essentially coupled thermal perturbations and interface deformations.

Of most interest is the HTW's growth phase shown in detail in FIG. 3.8b and d. The third mode, least relevant, has been left out for the sake of clarity. FIG. 3.8b and d show regions of linear growth for both sinusoidal modes from T' and z_i'. The actual growth rate for each mode is calculated by fitting exponential functions of the type,

$$\varphi(t) = \varphi_0 \, e^{\eta_t t}. \tag{3.23}$$

The growth rates for first and second modes are $\eta_{tT}^{I} = 1.4 \times 10^{-4}$ and $\eta_{tT}^{II} = 3.23 \times 10^{-5}$ for T' and $\eta_{tz}^{I} = 1.2 \times 10^{-4}$ and $\eta_{tz}^{II} = 2.6 \times 10^{-5}$ for z_i', FIG. 3.8b-d. Calculation of

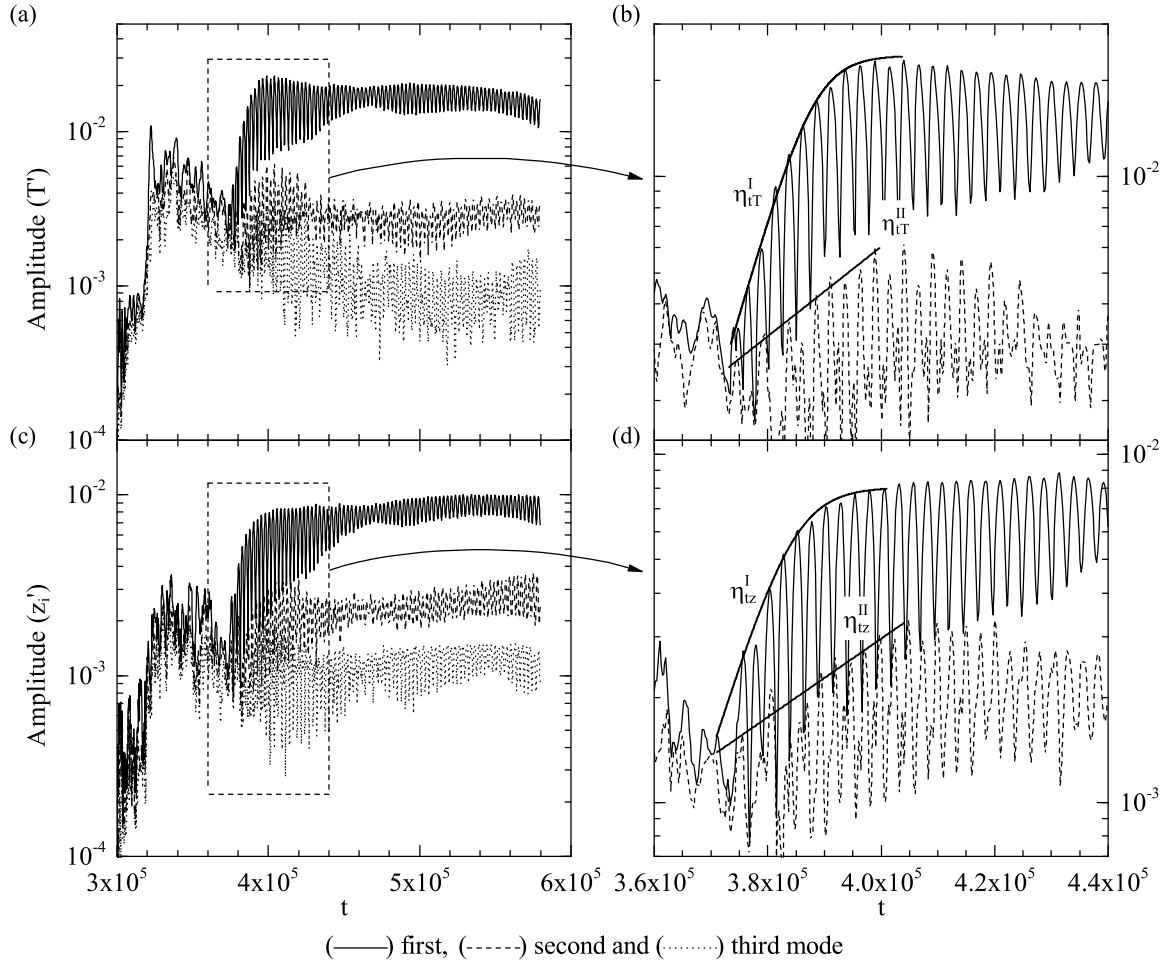

Figure 3.8: Instantaneous FFT analysis of the (a) temperature T' and (c) interface height z_i' disturbances for the spanwise section with $x = 0$. Graphs (b) and (d) show a detailed view of the HTWs' growth phase. The linear growth rates are represented by η_{tT}^{I} and η_{tT}^{II} for T' and by η_{tz}^{I} and η_{tz}^{II} for z_i'. The parameters are the same as in FIG. 3.4.

their respective ratios yields $\eta^I_{tT}/\eta^{II}_{tT} = 4.3$ and $\eta^I_{tz}/\eta^{II}_{tz} = 4.6$ which are remarkably close suggesting that the temperature and interfacial waves are strongly connected. Overtones are enslaved to the fundamental mode.

The study of the HTWs' spatial growth is continued by plotting the instantaneous T' and z'_i at P_o and at two additional monitoring points P_c and P_h situated near the cold and hot wall, respectively. The horizontal coordinates of these new locations are $(x_{P_c}, y_{P_c}) = (13.5, 0)$ and $(x_{P_h}, y_{P_h}) = (-13.5, 0)$. FIG. 3.9 reveals that the HTWs do not grow uniformly in either space or time. The prevailing mode is first observed in P_h, P_o and P_c at $t = 3.4\times10^5$ (approx.), 3.7×10^5 and 4.1×10^5, respectively, which confirms that the HTWs spatially grow in the opposite direction to that they propagate. Towards the hot wall both the disturbance growth rate and its final amplitude are larger. FIG. 3.9b shows the instantaneous interface height disturbance at the same points. The gas-liquid interface presents its largest deformations at the domain's centre. From these graphs it is also evident the existence of a direct relationship between the growth of T' and z'_i.

The FFT analyses of the T' signals, illustrated in FIG. 3.9a, result in the plot shown in FIG. 3.10a. The temperature disturbance captured by the monitoring locations are essentially a sinusoidal function of frequency $f = 1.88\times10^{-4}$. Conversion of this frequency to the Smith & Davis' dimensionless framework results in $f = 7.66\times10^{-3}$ which is roughly half of the value reported by these authors [11] for the critical mode, $f_c = 14.3\times10^{-3}$. In all three cases, the second most important mode is less that 10% of the fundamental. The corresponding amplitudes are 1.85×10^{-2}, 1.42×10^{-2} and 2.87×10^{-3} for P_h, P_o and P_c respectively which is in accordance with the observations made in FIG. 3.6d or FIG. 3.9, i.e. increasing HTW strength towards the hot end-wall. A similar plot is obtained when the FFT is performed for the z'_i signals, FIG. 3.10b. In this case, the leading modes act at the same frequency but the strongest is found at the centre of the layer, P_o, with an amplitude of 6.73×10^{-3}. The maximum interface deviations for P_h and P_c are 2.65×10^{-3} and 1.27×10^{-3}, respectively.

The conclusions drawn from the Fourier analysis are strengthened when the instantaneous T' and z'_i are plotted together for one of the points, P_o. FIG. 3.11 shows a few perturbation cycles. T' and z'_i are out-of-phase, i.e. a positive thermal perturbation is

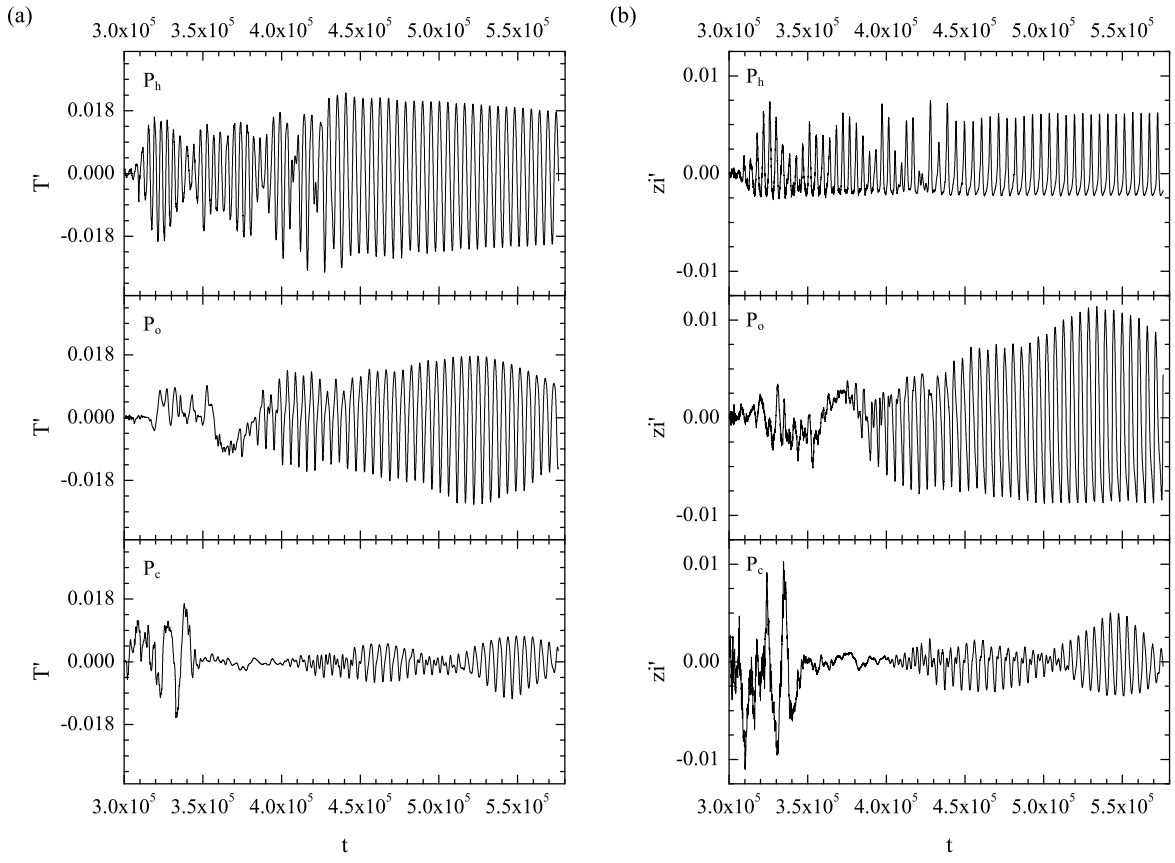

Figure 3.9: Instantaneous evolution of the (a) temperature T' and (b) interface height z_i' disturbances at monitoring points near the hot wall (P_h), centre of the layer (P_o) and near the cold wall (P_c). The parameters are the same as in FIG. 3.4.

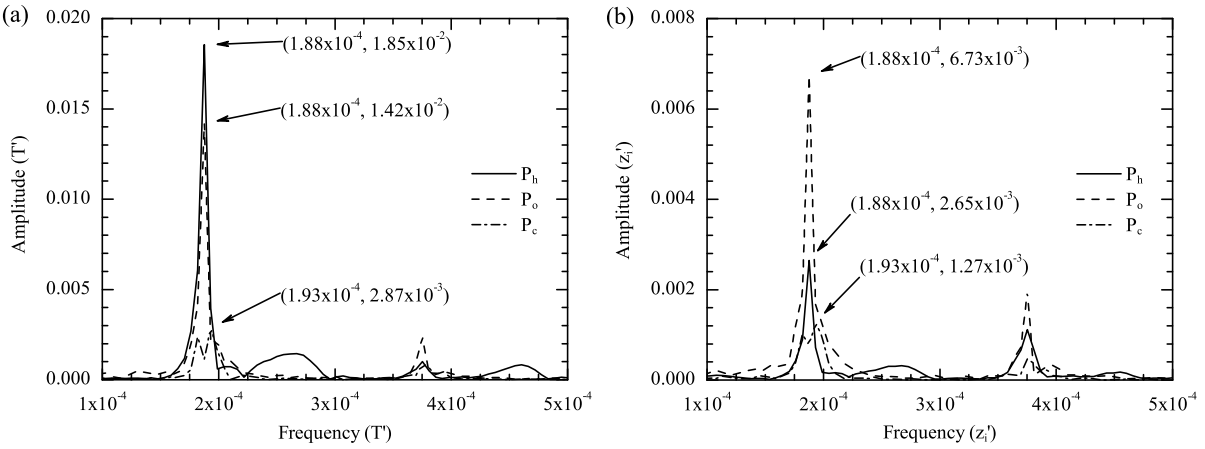

Figure 3.10: Frequency/amplitude diagram resulting from the FFT analysis performed over the (a) thermal disturbance T' (b) interface-height disturbance z_i' shown in FIG. 3.9. The parameters are the same as in FIG. 3.4.

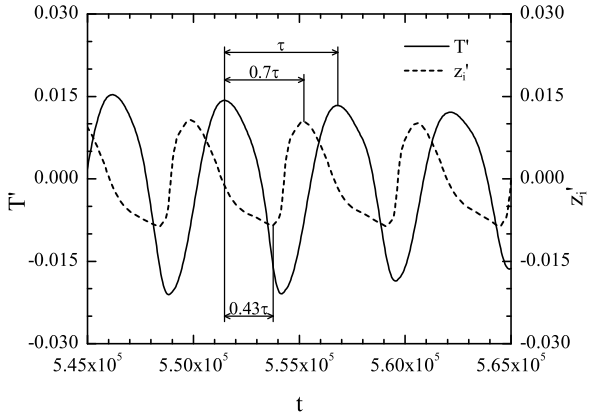

Figure 3.11: Instantaneous temperature T' and interface height z_i' disturbances at the centre of the liquid layer within the oscillatory stage, monitoring point P_o. The parameters are the same as in FIG. 3.4.

immediately followed by an interface depression after $t = 0.43\tau$. As it will be explained in more detail when the bulk flow is presented, the relationship between T' and z_i' illustrated in Fig. 3.11 results from the Marangoni effect for liquids, like the ones considered in the present work, for which the surface tension is inversely dependent on T. A hot spot in the interface corresponds to a location with lower surface tension than its surroundings. This results in the liquid being dragged away from the warm region with the subsequent local level depression becoming deeper. A similar effect is also observed in the case of surfactant-driven thin-film flows in which the surface tension is a decreasing function of the surfactant concentration [118].

FIG. 3.12 illustrates the interface disturbance z_i' at the same instant within the oscillatory regime to that presented in FIG. 3.5 or FIG. 3.6d, i.e. $t = 5.572 \times 10^5$. Comparing FIG. 3.12 with FIG. 3.6d reveals that the physical interface deformations follow the HTW pattern, travelling with the same angle of propagation ψ and phase-speed c_R from the lower-left corner (cold wall) towards the upper-right end (hot wall). Thus, it is concluded that the HTWs are not only travelling temperature perturbations but they also entail interfacial waves.

3.3.3 Bulk flow

The bulk flow within the non-linear regime for both liquid and gas phases is investigated by considering three vertical sections: one parallel to the yz-plane (spanwise section),

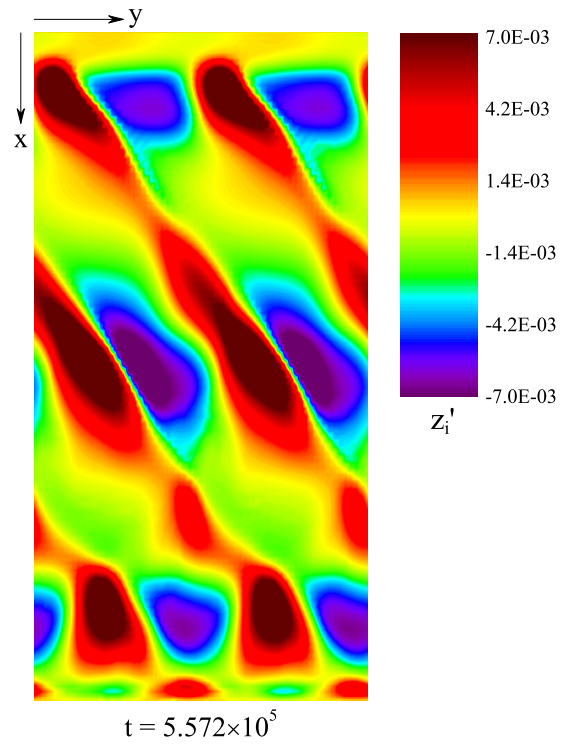

Figure 3.12: Interface-height disturbance z_i' within the oscillatory regime. The point in time is the same as that of FIG. 3.6d. The parameters are those shown in FIG. 3.4.

another parallel to the xz-plane (streamwise section) and a third section perpendicular to the HTW front, FIG. 3.13, FIG. 3.15 and FIG. 3.16, respectively. These sections are slightly closer towards the hot boundary where the HTWs are better defined. FIG. 3.13 shows (a) the temperature and interface-height disturbance, (b) the tangential velocity field, (c) the streamlines and (d) the isotherms for the spanwise section at x = -6 and $t = 5.572 \times 10^5$. FIG. 3.13a reveals two fully-formed HTWs travelling in the positive y direction and an equal number of interface deformations following them. The interface deformations are characterised by sharp crests with wide and nearly horizontal troughs whereas the thermal perturbations are more sinusoidal. The wavenumber in the spanwise direction is $\beta = 0.84$, which is fairly close to the critical value reported by Smith & Davis [11], $\beta_c = 1.27$, even though the flow is in the non-linear regime. The spatial delay between T' and z_i' follows the same ratios as those reported in FIG. 3.11. For example, from FIG. 3.13a one can see that the delay between subsequent T' and z_i' crests is approximately 0.7 times the wavelength in the spanwise direction, which is in agreement with the temporal delay observed in FIG. 3.11.

The spanwise bulk velocity field is presented in FIG. 3.13b. The average velocity in

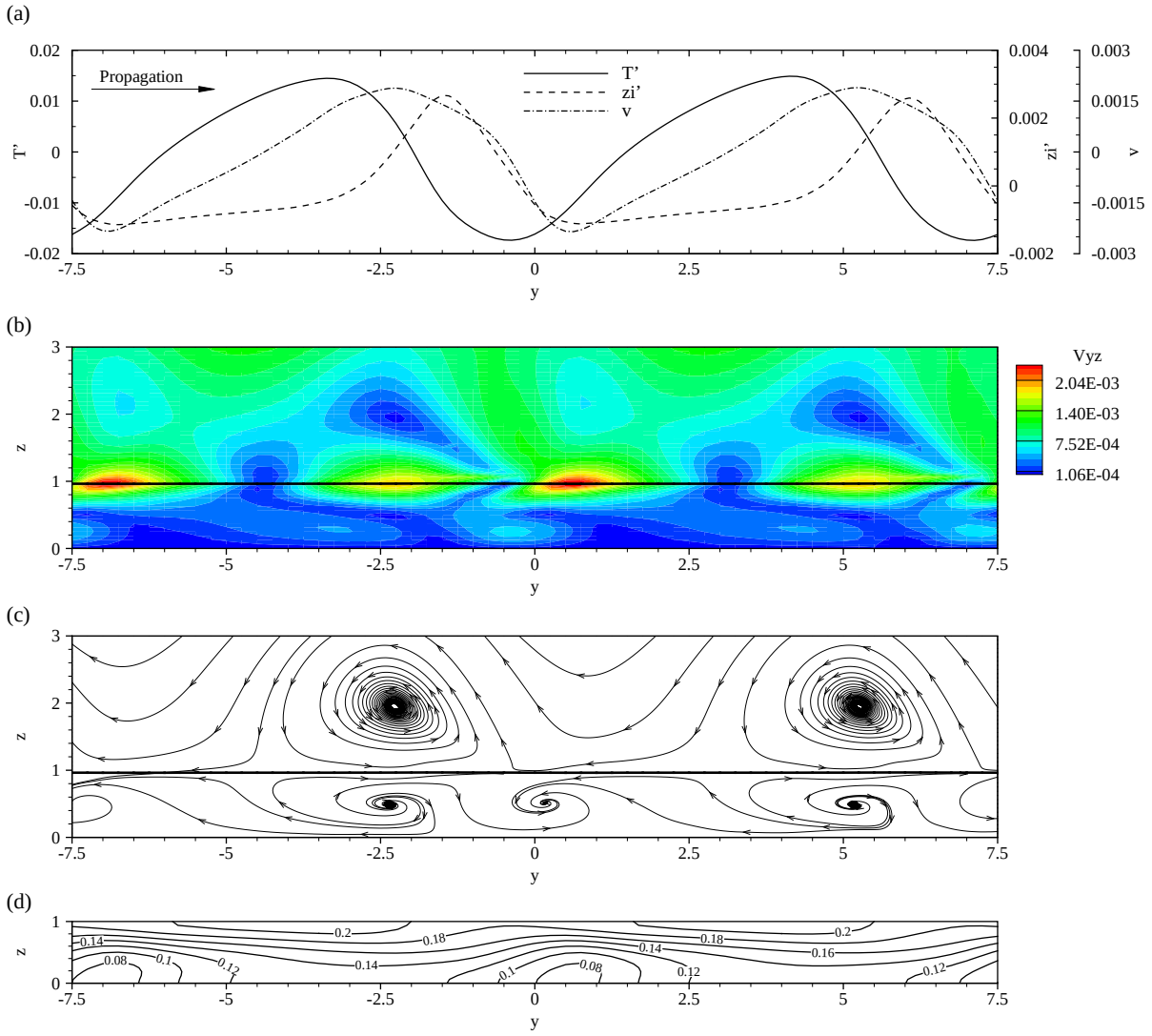

Figure 3.13: Spanwise section with $x = -6$ and $t = 5.572 \times 10^5$; (a) thermal and interface-height perturbations and interface velocity; (b) tangential velocity; (c) streamlines; (d) isotherms. The parameters are the same as in FIG. 3.4.

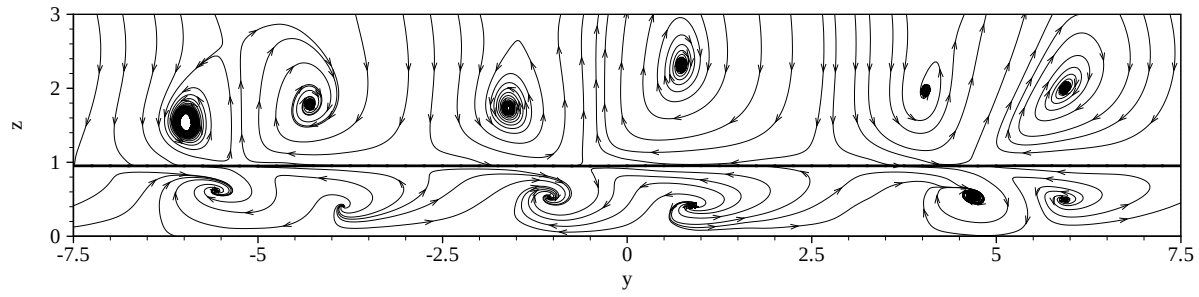

Figure 3.14: Streamlines at $t = 3.703 \times 10^5$ for a spanwise plane with x = -10. The point in time is the same as in FIG. 3.6a; the HTWs propagate towards the negative y direction. The parameters are the same as in FIG. 3.4.

the gas is larger than in the liquid. At the interface the flow is being pulled due to the Marangoni effects towards cold spots, min T', from both sides. This causes these points to be locations where opposite fluid streams collide and, consequently, where the velocity is minimum. The interface velocity of the fluid travelling towards the cold spots in the negative y direction, opposite to the HTW propagation, is higher than in the contrary case. These velocity inequalities result from energy imbalances around the cold regions. More thermal energy is transported from the hot spots towards their downstream cold points, negative y direction, than from the hot spots to their preceding cold ones. The net result is that the temperature at cold spots rises as the following hot spots become colder and the HTWs propagate spatially in the positive y. FIG. 3.13c shows the streamlines for both phases. Very well formed rolls rotating counter-clockwise are observed in the gas phase. These rolls follow the HTWs at the same velocity and their centre is located $0.24\lambda_y$ and $0.11\lambda_y$ after the points of minimum T' and maximum z_i' respectively. The streamline sources and sinks observed in the liquid are nothing but the projection of oblique rolls travel with the HTWs. These are explained in detail in FIG. 3.15 and FIG. 3.16.

FIG. 3.14 shows the spanwise streamlines for the first HTW mode found at $t = 3.703 \times 10^5$, FIG. 3.6a. This mode exists for a relatively long period of time before is suppressed by the prevailing disturbance; however, it bears similarities to the prevailing HTWs. Here, three pairs of counter-rotating rolls in the gas are observed travelling with the HTWs. As the simulation evolves, the size of the rolls rotating in one direction grows while the gap available for the second set becomes smaller. The result is that one set of rolls remains next to the interface and the other is pushed upwards. This behaviour and the shape of the velocity field between rolls in FIG. 3.13 suggests that there is a second layer of rolls in the gas phase rotating clockwise and located between those shown in FIG. 3.13. The flow in the liquid phase is comparatively slower and it also presents a characteristic pattern composed of swirls' pairs travelling with the HTWs, FIG. 3.13c.

FIG. 3.15 illustrates the streamwise section, at $y = 0$. The HTWs travel upstream, and the delays between T' and z_i' signals maintain the ratios reported in FIG. 3.11 and FIG. 3.13. The wavenumber in the streamwise direction is $\alpha = 0.62$, which compares well with critical wavenumber $\alpha_c = 0.82$ obtained from the linear theory by Smith &

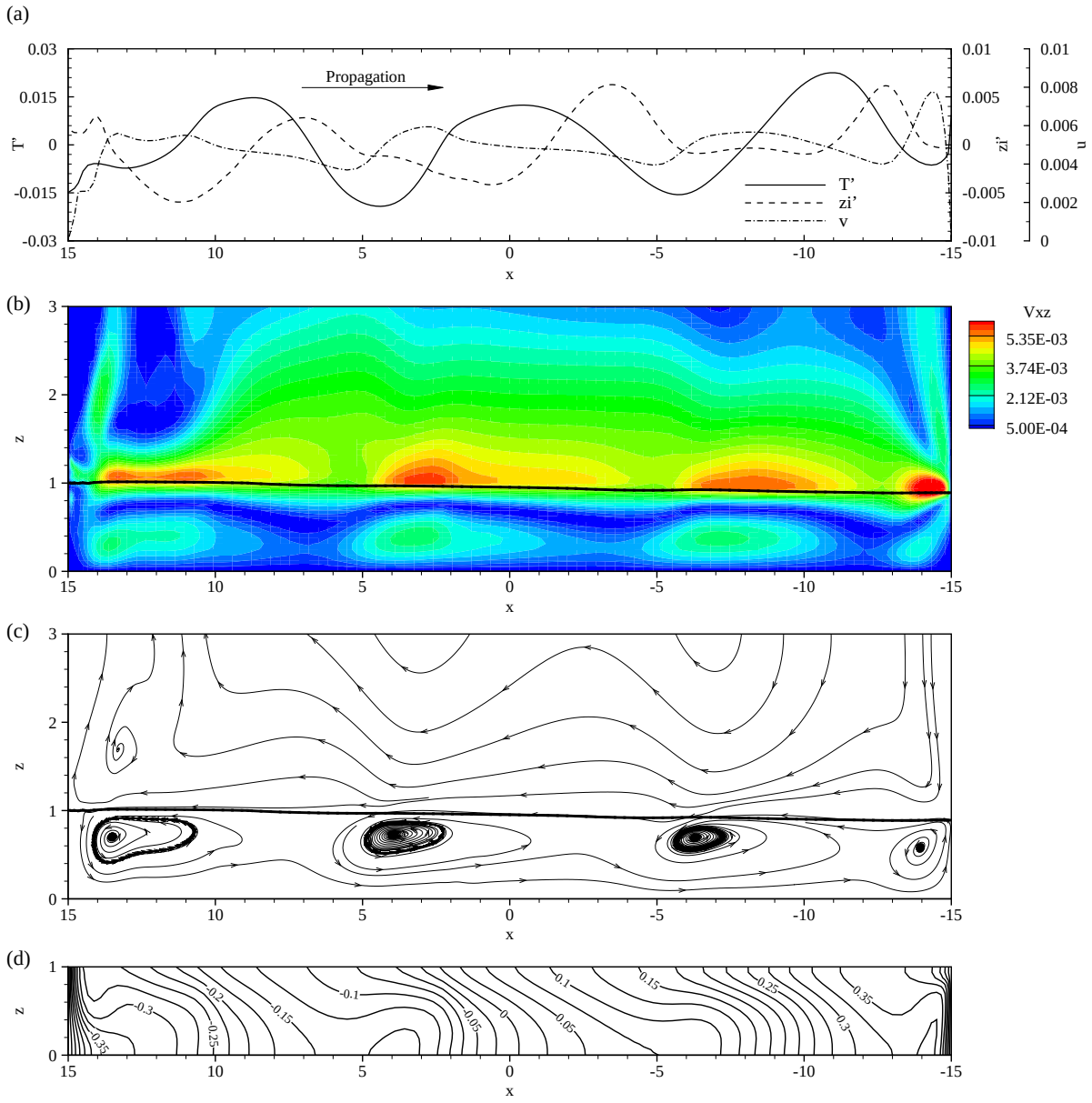

Figure 3.15: Streamwise section across the centre of the domain $y = 0$ with $t = 5.572 \times 10^5$; (a) thermal and interface-height perturbations and interface velocity; (b) tangential velocity field; (c) streamlines; (d) isotherms. The vertical dimension is scaled up by a factor of 3 with respect to x in (b), (c) and (d) for clarity of presentation. The parameters are the same as in FIG. 3.4.

Davis [11]. The interface-deformation profile is again formed by relatively wide valleys and narrower crests. The flow is driven by surface tension gradients at the interface, hence convection is stronger there. The same imbalance between the velocities around cold spots and responsible for the HTW propagation upstream is observed here.

Moving at higher velocity than the liquid, the gas motion presents a wavy pattern, FIG. 3.15c, resulting from the projection of the oblique rolls observed in the spanwise section, FIG. 3.13b, onto the streamwise plane. The main stream enters the domain through the open boundary near the hot wall and leaves it at the cold boundary. Stagnation areas appear near the exit point, where the main flow collides with the solid wall. Alterations to this behaviour are expected for lower Γ_k because buoyancy then will try to drive the gas near the walls in the opposite directions, i.e. buoyancy acts against interfacial convection to drive upwards the hot gas next to the heated boundary. The contrary case should be found near the cold wall. The analysis of the liquid phase reveals two standing rolls at, and parallel to, the vertical walls along with a second pair of oblique rolls across the layer. The former result from the inversion of the flow direction at the solid walls. The latter are parallel to the HTWs and propagate with them towards the heated boundary.

The description of the flow is completed with the study of the section parallel to the direction of propagation across the point $(x,\, y) = (-6,\, 0)$, FIG. 3.16. The data reveals that the amplitude of T' is not constant, but grows in the direction of propagation from 0.0125 to 0.0235. This tendency is also reported by Riley & Neitzel [40] in their experimental investigation and it is most likely to be a result of the finite domain. z_i' presents the opposite behaviour with its amplitude falling from 0.01 to roughly 0.002. The streamline plot, FIG. 3.16c, shows the travelling liquid rolls previously reported. Their centres are located just before the cold spots at a vertical coordinate equal to 2/3 of the local interface height. Note that this position coincides exactly with the point of zero velocity in the base state, FIG. 3.3a. This is not surprising given that the streamwise velocity field in the core region is basically the base state, i.e. return-flow solution, altered by a weaker periodic perturbation . The rotational speed of the rolls rises in the direction of propagation. This is directly derived from the growth of T' observed along the same path which results in larger surface tension gradients (driving force).

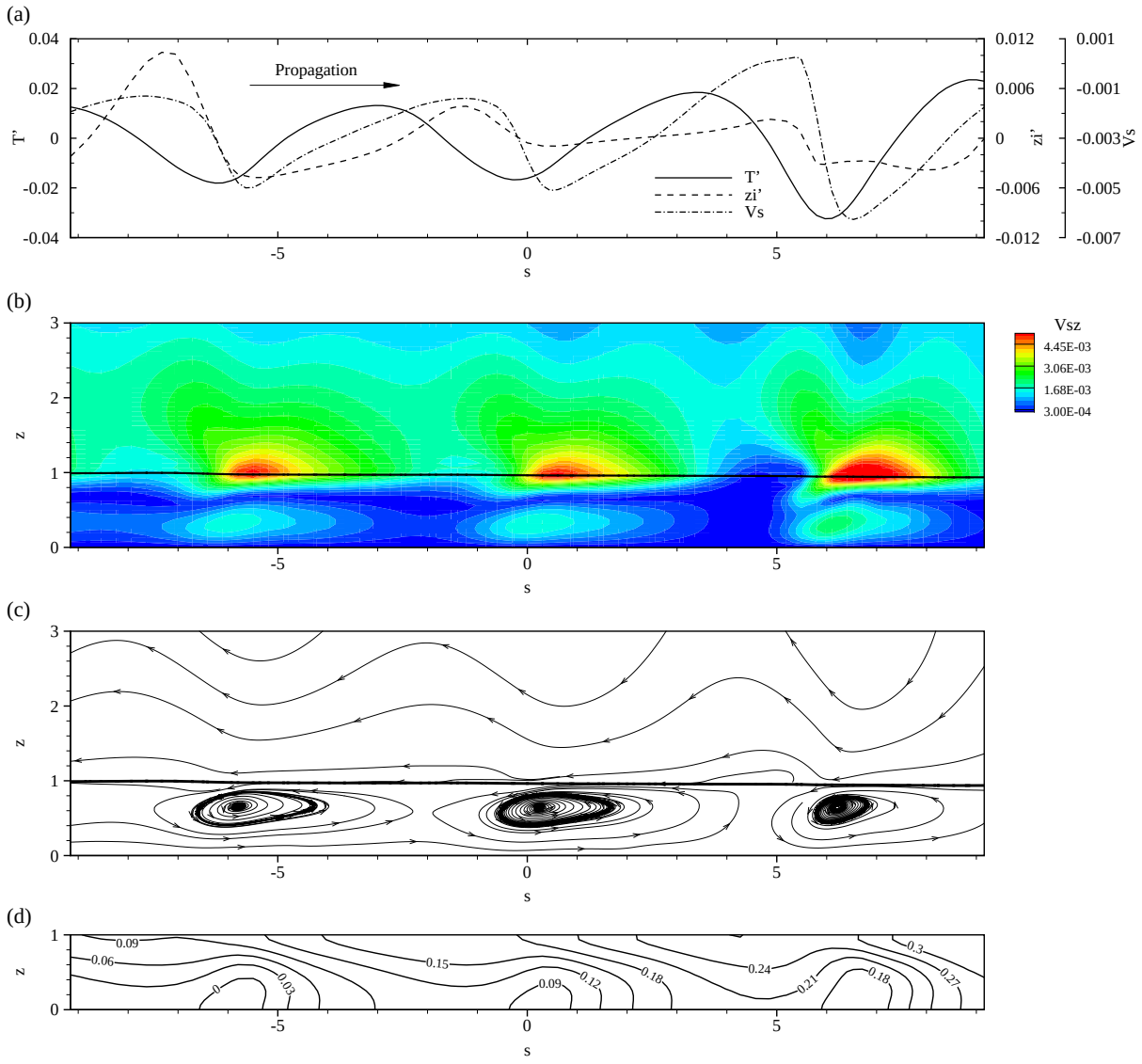

Figure 3.16: Vertical section parallel to the direction of propagation across the point $(x, y) = (-6, 0)$ at $t = 5.572 \times 10^5$; (a) thermal and interface-height perturbations and interface velocity; (b) tangential velocity field; (c) streamlines; (d) isotherms. The parameter s denotes the coordinate along the direction of propagation. The vertical dimension is scaled up by a factor of 1.5 with respect to s in (b), (c) and (d) for visualization purposes. The parameters are the same as in FIG. 3.4.

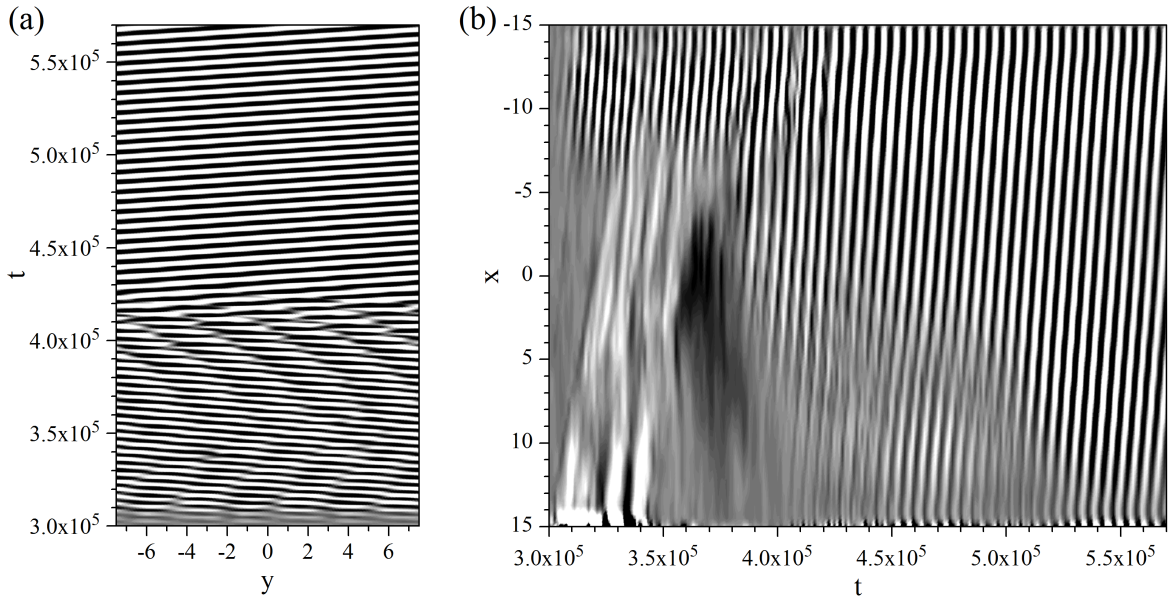

Figure 3.17: Space-time diagram for T' along (a) spanwise section with x =-11 (b) streamwise section with $y = 0$.

3.3.4 Spatio-temporal analysis

It is important to further process the data in order to evaluate the nature of the instability in the system under consideration. By using complex demodulation methods similar to those described in Pelacho *et al.* [119] and Burguete *et al.* [120] (and other references within them), we can determine whether the instabilities are convective (instabilities are growing in at least one moving frame but decaying in a laboratory frame) or absolute (a growing disturbance throughout the domain in the laboratory frame). We briefly describe the method here. Interfacial temperature perturbations (as those shown in FIG. 3.6) are analysed from $3 \times 10^5 \leq t \leq 5.7 \times 10^5$ and presented as spatio-temporal diagrams in FIG. 3.17. FIG. 3.17a shows the initial development of the first mode and how this mode is overwhelmed by the prevailing mode. FIG. 3.17b also shows both modes along with their instantaneous extension along the streamwise direction revealing how the HTWs grow in space from the hot wall towards the cold. The slopes of the bands represent to phase speed c_R in both the streamwise and spanwise directions. Once these bands are developed, their slope does not change which means that the phase speed remains constant. We then recover space-time $(x-t)$ diagrams of $\left(\frac{1}{T'}\frac{\partial T'}{\partial x}\right) = \alpha_x$ and $\left(\frac{1}{T'}\frac{\partial T'}{\partial t}\right) = -\omega$ and space-time $(y-t)$ diagrams of $\left(\frac{1}{T'}\frac{\partial T'}{\partial y}\right) = \alpha_y$ and $\left(\frac{1}{T'}\frac{\partial T'}{\partial t}\right) = -\omega$. We then determine the group velocities $\left|\left\langle\frac{\partial\omega}{\partial\alpha_x}\right\rangle_{xt}\right| = c_x^g \approx 0.0011$ and $\left|\left\langle\frac{\partial\omega}{\partial\alpha_y}\right\rangle_{yt}\right| = c_y^g \approx 0.001$, which are non-zero.

Noting for an instability to be absolute, the group velocity must be exactly zero. For the case under consideration, this provides an initial evidence for the absence of absolute instabilities, confirming that the thermocapillary instabilities are convective in nature. However, it must be emphasised that for a full understanding of the nature of these linear and non-linear thermocapillary instabilities further detailed simulations with varied levels of randomised pulsing are necessary. This is beyond the scope of this work.

3.4 Mechanism of Interface Heat Transfer

To date, thermocapillary instabilities have been numerically investigated by means of single-phase models solely, wherein heat losses across the free surface are computed through the thermal boundary condition acting on it. In most cases, the authors use simple expressions where the heat flux is calculated based on the Biot number $B = \hat{h}\,\hat{d}/\hat{k}$ and the temperature jump between the local temperature and the temperature of the bounding gas far from the free surface $\hat{T}_a$, i.e. $\partial T/\partial z = -B\,(T - T_a)$. Such expressions are approximations required when the gas phase is neglected and imply that the heat-flux distribution across the liquid surface is essentially dictated by the streamwise temperature profile rather than by the normal (local) temperature gradient between the liquid at the interface and the gas right next to it. In this investigation the gas phase dynamics are completely resolved by considering continuity of temperature at the interface, hence there is no need for this type of assumptions. Furthermore, this capability allows investigating the role of the local heat transfer across the interface in the HTW mechanism for the first time.

The same unstable system is considered with the only difference that the gas is not a thermal insulator any more and, therefore, heat transfer between phases is permitted. To that end, the conductivity ratio is reduced to a reasonable value, $\Gamma_k = 70$, while the remaining dimensionless groups along with the geometrical domain, mesh and marching time are maintained the same. To save computational time, the simulation is started from the results of the case previously presented at an instant after the adjustment period, FIG. 3.4. For the sake of simplicity, this instant is set as the reference, $t = 0$.

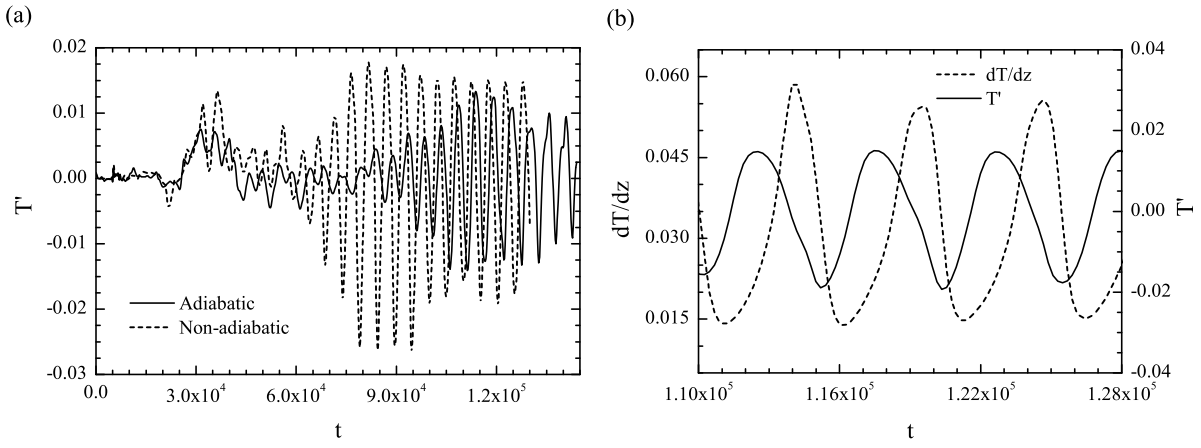

Figure 3.18: Instantaneous distribution of (a) T' for the adiabatic and non-adiabatic interface cases; (b) T' and the vertical temperature gradient $\partial T/\partial z$ for the non-adiabatic interface case within the prevailing oscillatory regime; Monitoring point P_o. Parameters: $Pr = 0.75$, $Re = 11900$, $Fr = 1720$, $We = 748$, $Bo_d = 0.111$, $\Gamma_\rho = 640$, $\Gamma_\mu = 14$, $\Gamma_k = 70$, $\Gamma_{cp} = 2$ and $\Gamma_\beta = 0.4$.

FIG. 3.18a shows the temporal evolution of T' at P_o for both the adiabatic and non-adiabatic interface cases. The non-adiabatic system exhibits a similar transient progress to the adiabatic layer, same stages, but the prevailing HTW mode develops in a shorter period of time. Ma, direction of propagation, wavenumber and phase-speed are essentially the same as those reported for the adiabatic system: $Ma = 210$, $\psi = 55°$, $k = 1.05$ and $c_R = 0.098$. However, it is evident that the heat transfer across the interface has increased the instability's growth rate and maximum amplitude, FIG. 3.18a.

For these observations to be consistent with previous investigations [11], which reported a stabilizing effect of heat loss across the free surface, the gas should warm the liquid. The local net heat flux between phases is given by q_{net} = -$(\mathbf{n} \cdot k\nabla T)$, however, when the interface is horizontal, which is essentially the case, only the vertical component of Fourier's law is relevant, i.e. $q_{net} \approx$ -$k(\partial T/\partial z)$. The computation of the vertical temperature gradient at the interface reveals that $\partial T/\partial z \geq 0$ everywhere. Thus, it is confirmed that the heat energy indeed flows from the gas to the liquid. The gradient distribution is highly transient and follows the HTW pattern. The maximum values are observed next to the solid walls, where the different extensions of the thermal boundaries layers for the liquid and the gas provoke the largest gradients. These findings agree with the experimental observations by Schwabe *et al.* [14] in which the authors also report heat input to the free surface in an analogous annular system.

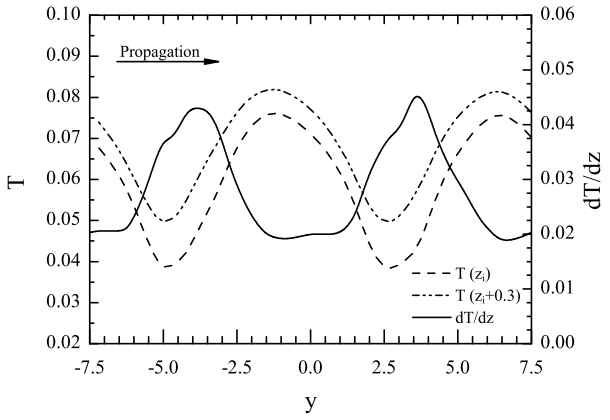

Figure 3.19: Spanwise section at $x = 0$ showing the temperature profile for the interface, $T(z_i)$, for the gas just above the interface, $T(z_i + 0.3)$, and the resulting vertical gradient $\partial T/\partial z$. The parameters are the same as in FIG. 3.18.

FIG. 3.18b illustrates the highly transient behaviour of the local heat flux across the interface. The maximum gradient does not coincide with the coldest locations, there is a temporal delay of roughly 0.35τ between the hot spots and the subsequent $\partial T/\partial z$ maxima. Note that these findings are again in contradiction with the results obtained with single-phase models which predict the largest energy fluxes at extreme-temperature locations, either crests or troughs depending on the choice of T_a. The disturbances in the temperature field provoked by the HTWs experience a delay as they propagate into the gas phase. FIG. 3.19 shows the spanwise temperature profile for interface, $T(z_i)$, and the gas just above, $T(z_i + 0.3)$, at $t = 1.543 \times 10^5$. The plot denotes that temperature field in the gas is subjected to oscillatory fluctuations due to the HTWs. The temperature signals are slightly offset with the gas disturbances following the HTWs at the interface. This delay explains why the maximum heat fluxes occur between temperature crests. The amplitude of the temperature perturbations becomes weaker as they propagate away from the interface until a point where they are completely dissipated. This spatio-temporal delay leads to the oscillatory behaviour of the heat flux, FIG. 3.18b.

3.5 Conclusions

The HTW instability, first predicted by Smith & Davis [11], has been investigated by means of DNS of laterally-heated shallow liquid layers surrounded by saturated environments. To that end, a novel two-phase model base on the VOF method in 3D has

been employed. The numerical results have been validated against the original linear theory [11] and the experimental work by Riley & Neitzel [40]. Obliquely-travelling HTWs have been reported for a liquid with $Pr = 0.75$ and a gas acting as a thermal insulator. The HTWs' angle of propagation, wavenumber and phase-speed have been computed and compared to the values predicted by Smith & Davis [11] obtaining good consonance. The complex spatio-temporal onset and growth of this type of instability have been described extensively.

Unstable systems give rise to not only thermal disturbances, i.e. HTWs, but also induce interface deformation, i.e. physical waves. The latter follow the HTW pattern travelling with the same angle of propagation but with a phase-lag. The ratios between the growth rates of the fundamental modes to the first overtones follow the same ratio for both the thermal and the physical waves. This suggests that there is a strong connection between the two and also that the overtones are enslaved to the fundamental mode. To the best of our knowledge, this is the first time that interface deformations coupled with HTWs have been reported. The main features of the bulk flow for both liquid and gas phases have also been described using the principal vertical sections, i.e. spanwise, streamwise and perpendicular to the HTWs' front. Convective rolls appear in both phases showing a coupled behaviour with the interface temperature and deflections through the Marangoni effect.

The last section of this chapter has been devoted to the investigation of the mechanism of heat transfer across the interface. Single-phase or one-sided approaches, that model this phenomenon via the temperature gradient between the interface and a constant reference temperature, provide imprecise results. The travelling nature of the HTWs leads to a delay in the propagation of thermal perturbations towards the gas resulting in maximum heat fluxes not at the points of extreme temperatures but somewhere in between.

Chapter 4

Effects of Phase Change

To date, investigations of HTWs have always ignored the effects of phase change. This is a simplification seldom encountered in experiments or real-life applications wherein liquid layers are frequently open to unsaturated atmospheres and, therefore, subject to evaporation. It is well known that even in the absence of an externally-imposed temperature gradient, evaporating thin films may become unstable due the spontaneous development of temperature gradients, e.g. Merkt & Bestehorn [51], Mancini & Maza [52], Sultan *et al.* [54], Guo & Narayanan [58], Kanatani & Oron [57]. Other examples, this time specifically involving HTWs, where the importance of evaporation has been pointed out are the ground-based experiments conducted by Schwabe *et al.* [41] and Riley & Neitzel [40] or the μ-gravity investigation by Schwabe *et al.* [14]. However, there is no work available in the literature which provides any notion regarding the effect of phase change on these thermocapillary instabilities.

Assumptions common to previous investigations addressing evaporation in other contexts have always included the use of the so-called "one-sided" or "1.5-sided" approaches. In these approaches, rather than attempting full DNS of both phases, the authors employ the arguments of negligible gas viscosity and/or thermal conductivity to decouple both phases and to justify concentrating in the liquid only. As it has already been shown in Chapter 3, this simplifications can be very restrictive and, in the particular case of the HTWs, lead to erroneously depicting the mechanism of heat transfer across the interface. The same problems arise with the evaporation flux in cases wherein this is modelled by

means of rudimentary mass transfer coefficients or by the traditionally-used strategy based on the solution of Laplace's equation for the vapour field. The latter disregards the convective transport of vapour which, as this chapter will show, may be completely incorrect for certain thermocapillary flows. To illustrate all these concepts, the two-phase model previously presented in chapter 3 is extended in section §4.1 to account for phase-change and the general advection-diffusion vapour-concentration transport.

The investigation presented in this chapter is also reported in Sáenz *et al.* [121].

4.1 Mathematical Formulation

4.1.1 Phase change model

The new model with phase change follows that presented in the previous chapter. The reader is referred to section §3.1 for some basic explanations that will not be repeated here. The schematic of the layer is the same as that shown in FIG. 3.1. The change of variables employed in the dimensional analysis remains unaffected, see (3.2). The liquid is again a pure Newtonian fluid whose physical properties are denoted by $\hat{\rho}_l$, $\hat{\mu}_l$, $\hat{k}_l$, $\hat{c}_{pl}$ and $\hat{\beta}_l$. The gas, on the other hand, is now a mixture of two components, inert gas and vapour (hereafter referred to with subscripts 1 and 2 respectively), whose mixture properties $\hat{\rho}_g$, $\hat{\mu}_g$, $\hat{k}_g$, $\hat{c}_{pg}$ and $\hat{\beta}_g$ depend on the relative amount of each component. The properties of the gas and vapour are included in the dimensionless description of the problem via the ratios,

$$\Gamma_\chi = \frac{\chi_l}{\chi_{g1}} \qquad \text{and} \qquad \Omega_\chi = \frac{\chi_l}{\chi_{g2}}, \tag{4.1}$$

with $\chi = \hat{\rho}$, $\hat{\mu}$, $\hat{k}$, $\hat{c}_p$ or $\hat{\beta}$ on both sides of each expression. Note that (4.1) is merely a concise way to represent a set of ten ratios ($\Gamma_\rho = \hat{\rho}_l/\hat{\rho}_{g1}$, $\Gamma_\mu = \hat{\mu}_l/\hat{\mu}_{g1}\ldots$, $\Omega_\rho = \hat{\rho}_l/\hat{\rho}_{g2}$, etc.). Assuming incompressibility for all the primary components; it can be shown that the gas-mixture density ρ_g is,

$$\rho_g = \left[\Gamma_g\left(1-\omega\right) + \Omega_g\omega\right]^{-1}, \tag{4.2}$$

where ω represents the vapour mass fraction defined as the mass of vapour divided by the total mass of gas mixture. The rest of the mixture properties are approximated according to relative amount of vapour and inert gas as follows,

$$\begin{aligned} \mu_g &= (1-\omega)/\Gamma_\mu + \omega/\Omega_\mu, \\ k_g &= (1-\omega)/\Gamma_k + \omega/\Omega_k, \\ c_{pg} &= (1-\omega)/\Gamma_{cp} + \omega/\Omega_{cp}, \\ \beta_g &= (1-\omega)/\Gamma_\beta + \omega/\Omega_\beta. \end{aligned} \tag{4.3}$$

Following a reasoning similar to that adopted in other relevant works [20, 91, 18, 79, 78, 122], it is considered that the diffusion of the vapour into the gas phase is the rate-limiting mechanism for phase change. In one-component systems, where the gas phase is the vapour of the liquid, kinetic theory indicates that the transfer rate across the interface is characterised by a time scale $O\,(10^{-10}\text{s})$ [74]. This crossing time is substantially shorter than the vapour-diffusion time scale $(\hat{l}_z - \hat{d})^2/\hat{D}$, $O\,(10^{1}\text{s})$, characteristic of liquids evaporating into normal atmospheres. $\hat{D}$ denotes the binary coefficient of mass diffusion in the gas mixture. Hence, in the evaporation process liquid molecules interchange rapidly between the surface and the adjacent air, so that this air is saturated with vapour [20]. As the air far away from the interface is not saturated, the vapour diffuses away from the interface. Previous sharp-interface approaches to evaporation, e.g. [20, 18, 79, 78], traditionally assume that the vapour distribution satisfies Laplace's equation, i.e. $\nabla^2\omega = 0$, and compute the local evaporation flux $\hat{J}$ based on Fick's law of mass diffusion, i.e. $\hat{J} = -\hat{\rho}_g\hat{D}\nabla\omega$. As it will be shown in this work, the use of Laplace equation with ω is an oversimplification for thermocapillary flows, since it does not take into account any transient phenomena or the convective transport of vapour in the gas phase. The suggested model, based on equation (4.22), is more general and takes all these effects into account. In addition, in the spirit of the VOF method, which regards the interface as a region of finite thickness, it is more convenient to formulate the interface mass transfer by virtue of a source term per unit volume S rather than by a mass flux per unit interface area.

Let us start by considering an arbitrary control volume within the interface area. In general, this infinitesimal region of volume V_C will contain some mass of liquid m_l and gas $m_g = m_{g1} + m_{g2}$. The volumes occupied by each phase are denoted by V_l and V_g respectively, with $V_C = V_l + V_g$. It follows that the gas-mixture density ρ_g computed as shown in equation (4.2) is,

$$\rho_g = \frac{m_g}{V_g}. \tag{4.4}$$

Hence, the vapour mass concentration $\mathcal{C}$ at the control volume can be obtained by,

$$\mathcal{C} = \frac{m_{g2}}{V_g} = \rho_g \omega. \tag{4.5}$$

To express the amount of vapour in the control volume as per unit total volume rather than per unit volume of gas phase, it is required the ratio of volume of gas to total volume, i.e.,

$$\frac{V_g}{V_C} = 1 - c. \tag{4.6}$$

Multiplying equation (4.5) by (4.6) leads to,

$$\frac{m_{g2}}{V_C} = (1 - c)\, \rho_g \omega, \tag{4.7}$$

which indicates that the term $(1 - c)\, \rho_g \omega$ represents the *actual* mass of vapour *per unit total volume* in the interface control volume.

As it was mentioned above, when the diffusion of vapour in the gas mixture is the rate-limiting process, it is assumed that the interface is saturated with vapour. Thus, the explanation proceeds working out the *theoretical* mass of vapour required in the control volume for it to be saturated. Considering that the gas is an ideal mixture and using Raoult's law and Dalton's law of partial pressures, the saturation mole fraction x_s is given by,

$$x_s = \mathscr{P}\, p_s, \tag{4.8}$$

where $\mathscr{P} = \hat{\gamma} \Delta \hat{T} / (\hat{p}_r \hat{d})$ is a new dimensionless group including the absolute (reference) pressure denoted by $\hat{p}_r$ and $p_s = p_s(T)$ is the saturation pressure at the local temperature.

The saturation mole fraction is converted to mass fraction as follows,

$$\omega_s = \frac{x_s}{x_s + \frac{(1-x_s)}{\mathscr{M}}}. \tag{4.9}$$

Here, $\mathscr{M} = \hat{M}_{g2}/\hat{M}_{g1}$ is the ratio between the molar masses of the vapour $\hat{M}_{g2}$ to the gas $\hat{M}_{g1}$. Similarly to what it was done in (4.7), equation (4.9) is multiplied by $(1-c)\,\rho_g$ leading to,

$$\frac{m_{g2s}}{V_C} = (1-c)\,\rho_g \omega_s, \tag{4.10}$$

where $(1-c)\,\rho_g\omega_s$ represents the mass of vapour per unit total volume that the control volume should contain to be at saturation conditions. Thus, if the interface is effectively saturated, it should be found matching results with (4.7) and (4.10) at any instant at any point along the interface.

Assuming that the interface is initially saturated with vapour, there are two ways by which this saturation condition can be lost as time goes by. On one hand, some vapour will be transported away from the interface by diffusion and/or convection. Unless this mass loss is replaced by new vapour, the actual interface vapour concentration $(1-c)\,\rho_g\omega$ will naturally decrease. On the other hand, the vapour pressure varies with T which means that any transient change in the thermal field will alter the local vapour pressure. For instance, if the local temperature rises due to some transient phenomenon (e.g. the HTWs), the local vapour pressure will be higher and the liquid should supplement more vapour to reach the new thermodynamic equilibrium. It is important to empathise once again that the evaporation process is relatively very slow, which makes the equilibrium approximation valid.

Making use of (4.7) and (4.10), it follows that all the above requirements are simultaneously met when the volumetric interface mass transfer S is computed as,

$$S\,t_s = (1-c)\,\rho_g\,[\omega_s - \omega]\,. \tag{4.11}$$

The sign convection is that positive S represents evaporation, and condensation the contrary case. Here, t_s is a measure of the phase change rate, small enough to maintain the

interface saturated. We choose the marching timestep for this. The relevant timescales in the system are the viscous, conductive, convective, molecular diffusivity and evaporative timescales. Thus, the marching time selected is smaller than all of them, i.e.

$$t_s = \Delta t < \min(\Delta\hat{x}^2/\hat{\nu}_l,\, \Delta\hat{x}^2/\hat{\alpha}_l,\, \Delta\hat{x}/\hat{u}_0,\, \Delta\hat{x}^2/\hat{D},\, \Delta\hat{x}\hat{\rho}_g/\hat{S}_{\max})/\hat{t}_0. \tag{4.12}$$

The first term in (4.11) makes sure that any transient deviation in the local vapour pressure due to the thermal effects is corrected while the second addend enforces the replacement of vapour lost due the species transport addressed by (4.22). It should be noted that (4.11) essentially states that the driving force of phase change is the difference between the saturation and the actual vapour concentration. Hence, we can rewrite (4.11) in terms of ω and p_s, with (4.8) and (4.9) and minor rearrangements, as follows,

$$S = \frac{(1-c)\,\rho_g}{t_s}\left(\frac{p_s}{p_s + \frac{1}{\mathscr{M}}\left(\frac{1}{\mathscr{P}} - p_s\right)} - \omega\right), \tag{4.13}$$

where the computation of S is restricted to the interface region only.

The vapour pressure is considered to vary with T according to the Antoine equation:

$$\log_{10}(\hat{p}_s) = \hat{A} - \frac{\hat{B}}{\hat{C} + \hat{T}} \tag{4.14}$$

where $\hat{A}$, $\hat{B}$ and $\hat{C}$ are empirical coefficients given in TABLE 4.1.

4.1.2 Governing equations

Accounting for phase change requires several new terms in the transport equations (3.8), (3.9), (3.16) and (3.17). The governing equation for liquid volume fraction c, (3.8), represents nothing but the liquid mass balance in the system. When phase change is neglected, this mass is conserved throughout the simulations. Obviously, this consideration is not valid for the evaporating scenario. The amount of liquid should decrease (increase) gradually due to evaporation (condensation). Thus, the governing equation for c becomes,

$$\frac{\partial c}{\partial t} + \nabla\cdot(c\mathbf{u}) = -S. \tag{4.15}$$

where the source term S, calculated according to (4.13), denotes the volumetric phase change rate accounting for the interface mass transfer. The sign convection for S, i.e. $S > 0$ corresponds to evaporation and $S < 0$ to condensation, explains the negative sign on the RHS of (4.15).

The flow is divergence-free in the bulk of the liquid and gas phases but not at the interface. Since incompressibility is assumed for all constituents, any mass transport between phases is accompanied by the corresponding volume conversion, the latter being dictated by the liquid-vapour density ratio. Hence, the continuity equation requires an additional term to account for any interface mass transfer,

$$\nabla \cdot \mathbf{u} = -S\left(1 - \Omega_\rho\right). \tag{4.16}$$

In the bulk of either the liquid or the gas, $S = 0$, and the divergence-free condition is recovered. In general, Ω_ρ is $O\left(10^3\right)$ and $S > 0$ which means that -$S(1 - \Omega_\rho) > 0$, i.e. when flow undergoes evaporation the RHS of (4.16) acts as a source of volume accounting for the liquid-to-vapour expansion. In the hypothetical case of matching densities, the system is divergence-free independently of any change of phase.

The general form of the momentum equation remains unaffected, i.e.,

$$\begin{aligned} \frac{\partial\left(\rho\mathbf{u}\right)}{\partial t} + \nabla \cdot \left(\rho\mathbf{u}\mathbf{u}\right) &= \frac{1}{Re}\left[-\nabla p + \nabla \cdot \mu\left(\nabla\mathbf{u} + \nabla\mathbf{u}^T\right)\right] - \rho\left(\frac{1}{Fr} - \frac{Bo_d}{Re}\beta T\right)\mathbf{e_z} \\ &\quad + \left(\frac{1}{We}\sigma\kappa\mathbf{n} - \frac{1}{Re}\nabla_{\mathrm{s}} T\right)\delta. \end{aligned} \tag{4.17}$$

with the exception of the one-fluid form of the physical properties ρ, μ and β. It should be noted that we assume that σ is a stronger function of T than of ω and, therefore, its constitutive equation remains also unaffected, i.e. $\sigma = 1 - Ca\,T$. Since the gas is a two-component mixture, these become,

$$\begin{aligned} \rho &= c + \rho_g\left(1 - c\right), \\ \mu &= c + \mu_g\left(1 - c\right), \\ \beta &= c + \beta_g\left(1 - c\right), \end{aligned} \tag{4.18}$$

where ρ_g, μ_g and β_g are the mixture properties computed with (4.2) and (4.3). For the same reason, k and c_p are computed as follows,

$$\begin{aligned} k &= c + k_g\,(1-c)\,, \\ c_p &= \frac{c + \rho_g c_{pg}(1-c)}{c + \rho_g(1-c)}. \end{aligned} \tag{4.19}$$

The new energy equation is,

$$\frac{\partial\,(\rho c_p T)}{\partial t} + \nabla\cdot(\rho c_p T\mathbf{u}) = \frac{1}{RePr}\nabla\cdot(k\nabla T) - \frac{1}{Ja}S. \tag{4.20}$$

The last term accounts for the energy loss/gain associated with evaporation/condensation (sensible heat). This additional term results in that a new dimensionless group arises, namely the Jakob number,

$$Ja = \frac{\hat{c}_{pl}\Delta\hat{T}}{\Delta\hat{h}_v} \tag{4.21}$$

where $\Delta\hat{h}_v$ denotes the specific latent heat.

The set of governing equations forming the model is completed with the full advection-diffusion equation employed to handle the transient evolution of the vapour field. Species transport is only solved for the gas phase and thermodiffusion (Soret effect) is disregarded. Hence, the diffusion flux is basically modelled by Fick's law and the species conservation equation becomes,

$$\frac{\partial\,[\rho_g\,(1-c)\,\omega]}{\partial t} + \nabla\cdot[\rho_g\,(1-c)\,\omega\mathbf{u}] = \frac{1}{ReSc}\nabla\cdot[\rho_g\,(1-c)\,\nabla\omega] + S. \tag{4.22}$$

Here, Sc is the Schmidt number defined as,

$$Sc = \frac{\hat{\nu}_l}{\hat{D}}. \tag{4.23}$$

This mathematical problem is closed with the boundary and initial conditions. The boundary and initial conditions for p, T and $\mathbf{u}$ are the same as those described in section 3.1.3. The additional boundary conditions for the new field, ω, are impermeability

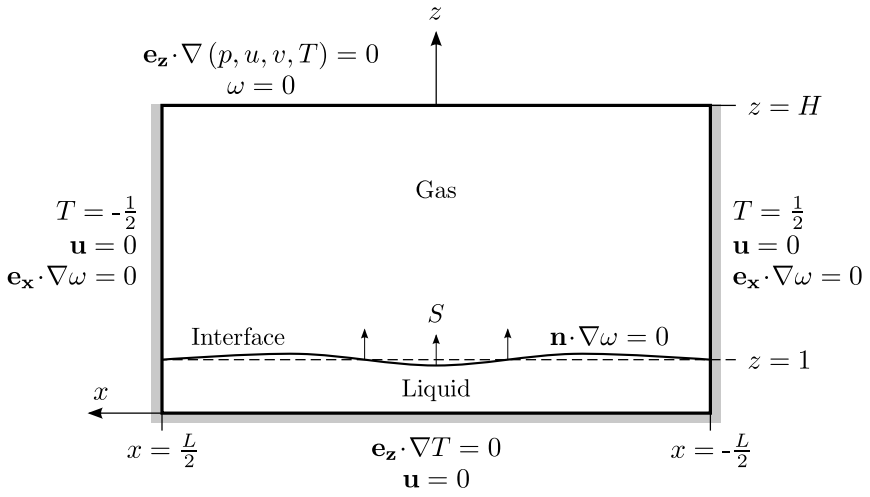

Figure 4.1: Schematic of the flow highlighting the boundary conditions.

at the bottom and vertical walls, i.e.,

$$\mathbf{e_x}\cdot\nabla\omega=0 \qquad \text{at} \qquad x=\mp\frac{L}{2}, \tag{4.24}$$

$$\mathbf{e_z}\cdot\nabla\omega=0 \qquad \text{at} \qquad z=0. \tag{4.25}$$

At the opening ω is fixed in accordance with the assumptions that the boundary is far enough so that vapour concentration equals zero, i.e.,

$$\omega=0 \qquad \text{at} \qquad z=H. \tag{4.26}$$

This is also consistent with experimental setups involving the continuous removal of vapour-laden gas so as to prevent build-up of vapour. Since the interface position is part of the solution, ω also requires the implicit imposition of the impermeability condition at the liquid-gas interface, i.e.,

$$\mathbf{n}\cdot\nabla\omega=0. \tag{4.27}$$

A summary of the boundary conditions is shown in FIG. 4.1.

To conclude, the initial conditions presented in (3.21) are completed considering that the vapour mass fraction at the beginning is,

$$\omega=1-(1-\omega_i)\left(\frac{1-\omega_t}{1-\omega_i}\right)^{\left(\frac{z-1}{H-1}\right)} \qquad \text{at} \qquad t=0, \tag{4.28}$$

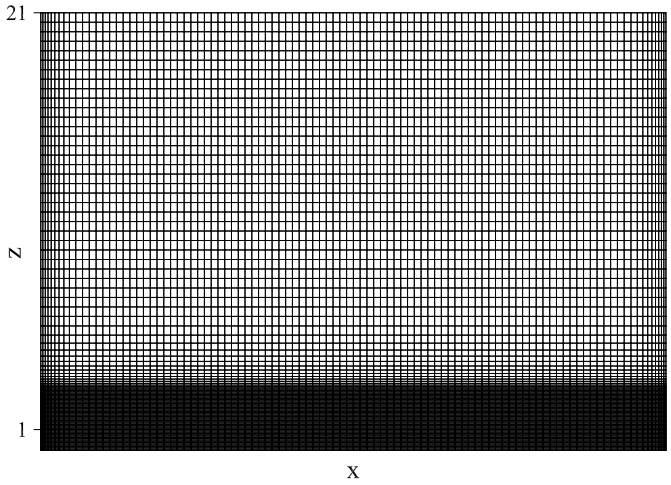

Figure 4.2: Mesh distribution along the xz-plane (streamwise section) for the reference case $101^x \times 61^y \times 97^z$. The grid spacing is uniform in the y-direction.

where $\omega_i = \omega_i(T)$ and ω_t are the vapour mass fraction at the interface and at the open boundary, respectively. This concentration profile represents a modified solution to the case of isothermal steady-state diffusion of vapour through stagnant gas with the liquid-gas interface level fixed. In accordance with the fundamental physics of a typical evaporating system, (4.28) enforces a non-uniform species distribution with increasing vapour concentration towards the hot region. As it was mentioned earlier, for sake of simplicity this work is restricted to the case with $\omega_t = 0$ and, therefore, (4.28) reduces to,

$$\omega = 1 - (1 - \omega_i)^{\left(\frac{H-z}{H-1}\right)} \qquad \text{at} \qquad t = 0. \tag{4.29}$$

In summary, the simultaneous solution of the governing equations (4.15), (4.16), (4.17), (4.20) and (4.22) with the interface mass-transfer rate calculated according to (4.13) will elucidate the dynamics of the two-phase, phase-change problem considered here. The numerical strategy is the same as that described in section 3.1.4. The physical domain is discretized by non-uniform mesh distribution in the xz-plane. The grid resolution is concentrated near the walls and at the liquid and gas above it for an accurate resolution of the boundary-layers and the dynamics around the interface region, respectively, (FIG.4.2). The mesh spacing is uniform in the y-direction. The final grid employed for the main case examined in the body of this paper (below, termed *reference case*) is $101^x \times 61^y \times 97^z$, see FIG.4.2. The marching time for the reference case is 0.823.

$\hat{A}$	$\hat{B}$	$\hat{C}$
9.418	1509	241.6

Table 4.1: Empirical coefficient for the Antoine equation $\log_{10}(\hat{p}_s) = \hat{A} - \hat{B}/(\hat{C} + \hat{T})$ for 0.65cSt silicone oil with $\hat{p}_s$ in (Pa) and $\hat{T}$ in (°C).

4.2 Experimental Validation

To ensure that the upgraded model, which takes into account phase change, also provides physically meaningful results, further validation work has been undertaken. Zhu & Liu [123] recently conducted experiments in rectangular test cells of similar characteristics. The subject liquid is again silicone oil with three different levels of viscosity, namely 0.65, 1.5 and 5 cSt. The horizontal thermal gradients range from $\Delta\hat{T} = 0$ to 14 °C, while the layer depth is varied from $\hat{d} = 1$ to 2 mm. The vertical position of the liquid surface is tracked via a laser confocal displacement meter with an accuracy of 0.3 μm and the overall evaporation rate $M(t)$ is reported by computing the rate of change in the mean layer height $\bar{z}_i$, i.e. $M(t) = \text{-d}\bar{z}_i/\text{d}t$.

One of the above mentioned cases is simulated here: 1-mm liquid layer of 0.65 cSt silicone oil with $\Delta\hat{T} = 10$ °C. This configuration is chosen for being the one closest to the range of parameters considered in the body of this work. The physical properties of the liquid, vapour and gas are available in TABLE 3.1. The Antoine coefficients for the vapour pressure can be found in TABLE 4.1.

In the dimensionless description of the problem, this case is represented with $Pr = 10$, $Re = 2800$, $Fr = 340$, $We = 164$, $Bo_d = 0.11$, $Sc = 0.12$, $Ja = 0.09$, $\mathscr{P} = 8.90 \times 10^{-6}$, $\mathscr{M} = 5.6$, $\Gamma_\rho = 640$, $\Gamma_\mu = 27$, $\Gamma_k = 10$, $\Gamma_{cp} = 2$, $\Gamma_\beta = 0.4$, $\Omega_\rho = 100$, $\Omega_\mu = 80$, $\Omega_k = 9.4$, $\Omega_{cp} = 1.34$ and $\Omega_\beta = 0.3$. Zhu & Liu [123] do not report any noticeable effect resulting from the spanwise direction, thus the validation is restricted to 2D. Nonetheless, tests were also carried out in 3D confirming that the results are the same. The streamwise length is $L = 40$. As far as the domain's height H is concerned, the reader should note that this parameter has a significant effect on the overall evaporation rate, given that it determines the length over which the vapour concentration goes from saturation (at the interface) to zero (at the upper boundary). H is initially selected following the work on

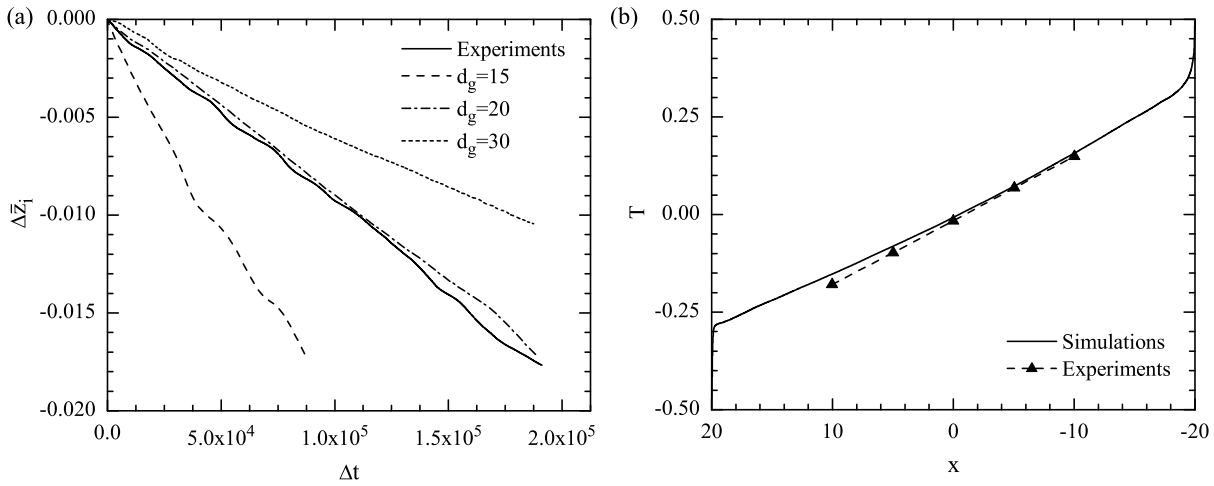

Figure 4.3: (a) Average evaporation rate and (b) streamwise temperature, $d_g = 20$, for a 1-mm liquid layer of 0.65 cSt silicone oil with $\hat{l}_x = 40$ mm and $\Delta\hat{T} = 10$ °C. The dimensionless groups are $Pr = 10$, $Re = 2800$, $Fr = 340$, $We = 164$, $Bo_d = 0.11$, $Sc = 0.12$, $Ja = 0.09$, $\mathscr{P} = 8.90 \times 10^{-6}$, $\mathscr{M} = 5.6$, $\Gamma_\rho = 640$, $\Gamma_\mu = 27$, $\Gamma_k = 10$, $\Gamma_{cp} = 2$, $\Gamma_\beta = 0.4$, $\Omega_\rho = 100$, $\Omega_\mu = 80$, $\Omega_k = 9.4$, $\Omega_{cp} = 1.34$ and $\Omega_\beta = 0.3$. The experimental data has been obtained from [123].

droplets by Hu & Larson [18]. This suggests that, in processes of free evaporation, the vapour concentration is comparable to the infinite value at a distance 20 times the droplet radius. Hence, the domain's height is initially set to $H = 21$ so that the dimensionless gas depth $d_g = H - 1 = 20$. Two additional cases in this range are also contemplated, namely $d_g = 15$ and 30.

The resulting evaporation rates are compared with the experimental in FIG. 4.3a. Evaporation becomes stronger for smaller d_g. In all cases the evaporation rates are essentially linear, which is in qualitative agreement with the experimental observations. Excellent quantitative agreement is additionally found between the experiments and the curve for $d_g = 20$. The slopes denote that the evaporation rate measured in the laboratory is $M(t) = 9.27 \times 10^{-8}$ ($0.169\ \mu\mathrm{m\,s^{-1}}$ in dimensional form) while the computations predict 8.92×10^{-8} ($0.163\ \mu\mathrm{m\,s^{-1}}$). With $d_g = 15$ and 30, the corresponding $M(t)$ are 1.93×10^{-7} ($0.352\ \mu\mathrm{m\,s^{-1}}$) and 5.19×10^{-8} ($0.094\ \mu\mathrm{m\,s^{-1}}$).

Furthermore, the experimental and numerical streamwise temperature profiles along the interface are compared in FIG. 4.3b. The model accurately reconstructs the thermal enforcing responsible for the flow motion. The numerical interior temperature gradient $\hat{b}_i$ is $155\ \mathrm{K\,m^{-1}}$ which is close to $164\ \mathrm{K\,m^{-1}}$ reported experimentally. The fact that not only $\hat{b}_i$ but also the temperature level matches the observations in the laboratory indicates that

the thermal boundary-layers at the end-walls are also accurately solved.

4.3 Effects on the Base State

The stability of the flow is intimately related to the base state. No HTW exists unless $\hat{b}_i$ is larger than certain critical value, which mainly depends on Pr for shallow layers. When the liquid undergoes phase change, the cooling effect of evaporation might lead to a lower interface temperature which could alter $\hat{b}_i$ and, therefore, the stability of the liquid layer. To check this, a new case is defined with the subsequent parameters: $Pr = 0.75$, $Re = 11900$, $Fr = 1720$, $We = 748$, $Bo_d = 0.11$, $Sc = 0.06$, $Ja = 0.11$, $\mathscr{P} = 1.07 \times 10^{-5}$, $\mathscr{M} = 5.6$, $\Gamma_\rho = 640$, $\Gamma_\mu = 14$, $\Gamma_k = 70$, $\Gamma_{cp} = 2$, $\Gamma_\beta = 0.4$, $\Omega_\rho = 100$, $\Omega_\mu = 43$, $\Omega_k = 66$, $\Omega_{cp} = 1.34$ and $\Omega_\beta = 0.3$. This configuration essentially corresponds to the main system investigated in chapter 3 but with the additional groups required to account for phase change. The domain is horizontally delimited by $L = 30$ and $W = 15$ and vertically by $H = 21$ ($d_g = 20$). The experimental validation suggests this domain's height as optimum to account for evaporation of the same intensity as that found in the laboratory. Henceforth, this configuration is referred to as the *reference case*. For illustrative purposes, an additional scenario undergoing stronger phase change is also examined, namely $d_g = 10$. Note that, as the gas depth decreases, the overall vapour mass-fraction gradient between the interface (saturated) and the opening (dry air) increases.

Initially the system goes through an adjustment period as that described in section §3.2, from the initial conditions to the effective numerical base state with the thermal boundary-layers at the end-walls. Before any conclusion is drawn, the simulations are run for very long times, $t > 4 \times 10^5$, to make sure that the dynamics are beyond this transient stage. The final streamwise T profiles are shown in FIG. 4.4a along with that for the same case without phase change. As expected, T decreases with d_g. This effect is more noticeable towards the warm region given the higher local evaporation rate found there. The hot thermal boundary-layer becomes larger while the cold one remains essentially unaffected. The T profile seems to pivot around the latter. The effective thermal gradient $\hat{b}_i$ is consequently smaller with evaporation but no more than 1.5% for the cases here

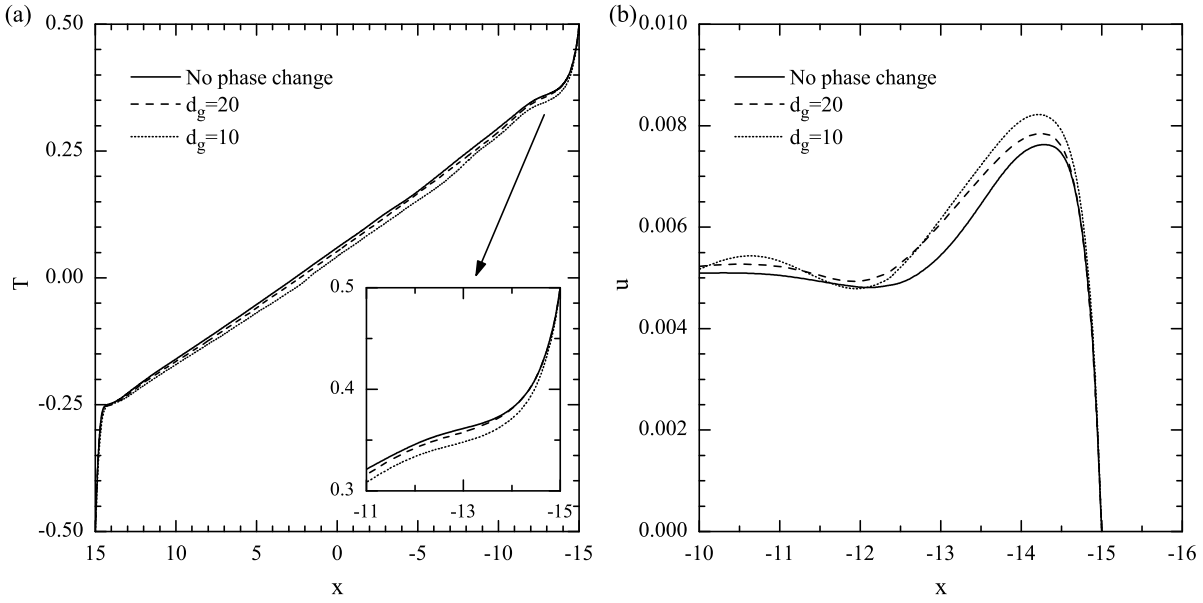

Figure 4.4: Effects of phase change in the effective base state. (a) Streamwise temperature, (b) Interface velocity near the warm wall. The inset in (a) shows accentuated thermal boundary layer due to phase change. The parameters are $Pr = 0.75$, $Re = 11900$, $Fr = 1720$, $We = 748$, $Bo_d = 0.11$, $Sc = 0.06$, $Ja = 0.11$, $\mathscr{P} = 1.07 \times 10^{-5}$, $\mathscr{M} = 5.6$, $\Gamma_\rho = 640$, $\Gamma_\mu = 14$, $\Gamma_k = 70$, $\Gamma_{cp} = 2$, $\Gamma_\beta = 0.4$, $\Omega_\rho = 100$, $\Omega_\mu = 43$, $\Omega_k = 66$, $\Omega_{cp} = 1.34$ and $\Omega_\beta = 0.3$.

studied, $\hat{b}_i = 0.68\Delta\hat{T}/\hat{l}_x = 272\ \mathrm{K\,m^{-1}}$. Therefore, the liquid flow (return-flow solution in Smith & Davis [11]) is not significantly altered. FIG. 4.4b shows the streamwise interface velocity near the hot wall. The fact that evaporation results in a more pronounced thermal boundary-layer (see inset in FIG. 4.4a) leads to larger velocity overshoots. The streamwise gradient $\mathrm{d}T/\mathrm{d}x$ and therefore the driving force responsible for the resulting flow is stronger. The maximum velocity is 2.5% ($d_g = 20$) and 7.6% ($d_g = 10$) higher than that without phase change, $u = 7.65 \times 10^{-3}$. The overshoots observed are consistent with the LDV measurements and calculations performed by Villers & Platten [124] and by Riley & Neitzel [40] for flows of acetone ($Pr = 4.2$) and silicone oil ($Pr = 13.9$) respectively.

These findings suggest that evaporation plays only a minor role in the liquid base state. This is not surprising given that the thermal gradient is strongly enforced by the fixed-temperature walls. For a liquid with a relatively low vapour pressure such as the one examined here (comparable to ethanol), the latent energy required is simply provided through the walls with little impact for the streamwise temperature signature. This might not be the case in more volatile liquid, for example at reduced pressure.

4.4 Effects on the Instabilities

The effective Marangoni number as defined in (3.5) is computed to be $Ma = 201$. Therefore, the configuration under consideration corresponds to a linearly unstable regime. Following the strategy presented in chapter 3, an infinitesimal perturbation is then introduced in the effective base state for T and $\mathbf{u}$. The perturbation amplitudes, wavenumber and angle of propagation are the same as those used for the non-evaporating case, i.e. $A(\mathbf{u}) = 5.1 \times 10^{-6}$ and $A(T) = 10^{-3}$, $k = 1.52$ and $\psi = 57°$. For sake of simplicity, the point in time when the perturbation is introduced is reset to $t = 0$.

4.4.1 Overall behaviour

In the absence of phase change, it was observed that perturbation is initially enhanced near the warm wall (*first* HTW mode). Nonetheless, after some time other modes begin interacting with the first and eventually suppress it in favour of a stronger non-linear group of HTWs (*prevailing* HTW mode). With time, the prevailing mode grows downstream until it spans the entire domain. Although this general behaviour is found to be qualitatively similar in the presence of phase change, evaporation introduces noticeable effects. The overall HTW development (with and without phase change) is compared in FIG. 4.5 via space-time diagrams for T'. The spanwise section is located closer to the hot wall to record linear and non-linear HTW modes. FIG. 4.5a,c,e reveal the inhibiting effect of evaporation in the development of the prevailing mode throughout the layer. For instance, by $t = 9 \times 10^4$ the HTWs have already reached the cold wall when phase change is left out, FIG. 4.5a. However, for decreasing d_g, the instabilities have barely filled $2/3\,L$ (FIG. 4.5c, $d_g = 20$) and $1/2\,L$ (FIG. 4.5e, $d_g = 10$) after the same period of time. In the latter case, the wave pattern is less distinct and subjected to perceptible distortions indicating a weakened non-linear mode. The slopes of the bands in FIG. 4.5a,c,e, indicating phase-speeds, denote that all HTW modes (linear and non-linear) propagate upstream in agreement with the mechanism described by Smith [32]. The first HTW modes can be observed near the hot boundary (top) extending up to $1/4\,L$.

No preferred direction of propagation is detected along the spanwise axis. Sometimes

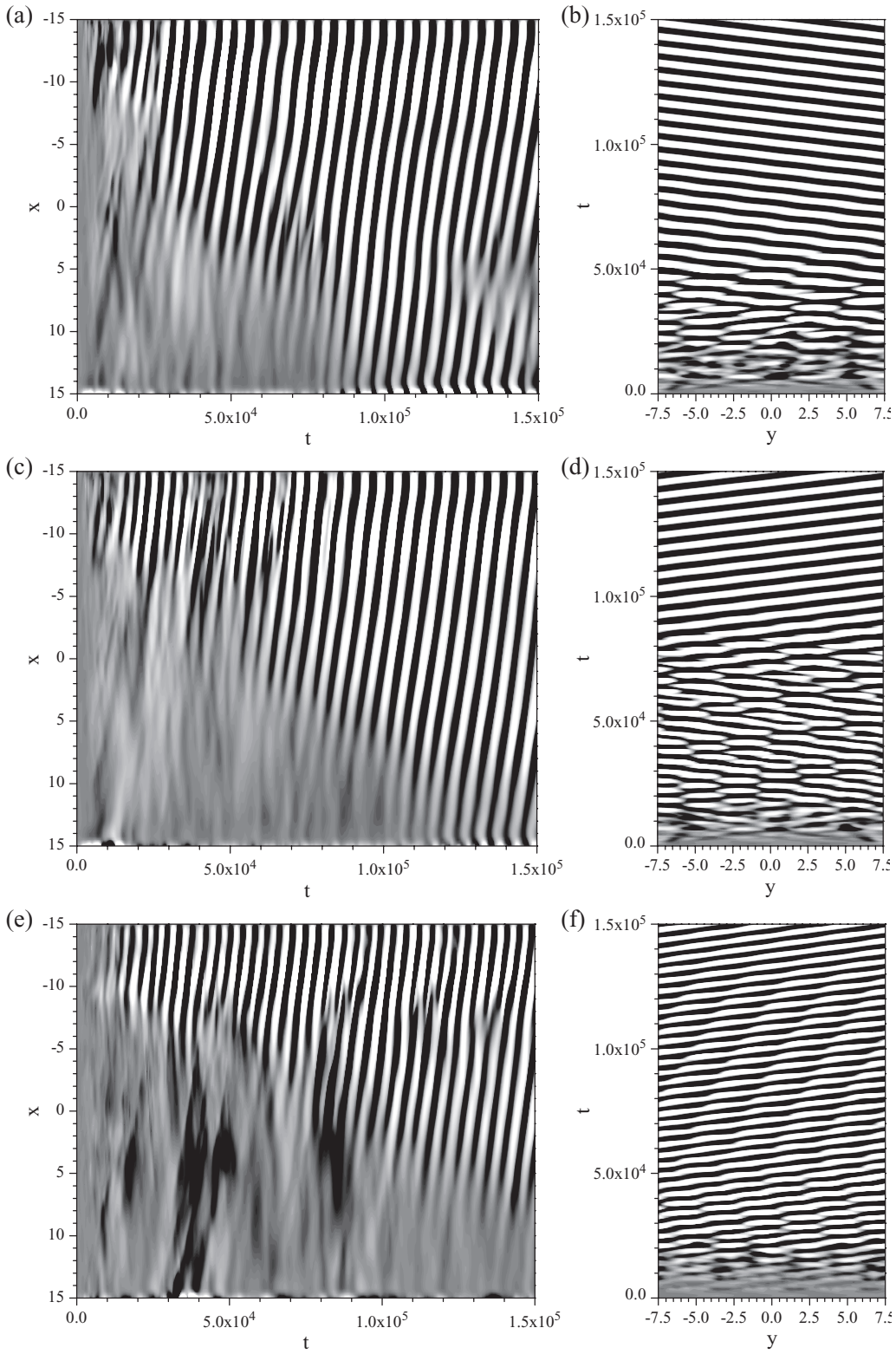

Figure 4.5: Space-time diagrams for T' along the central streamwise section (left) and along the spanwise section at $x = -11$ (right). (a) & (b) case without phase change; (c) & (d) with phase change and $d_g = 20$; (e) & (f) with phase change and $d_g = 10$. The parameters are those in FIG. 4.4.

the HTWs travel in the negative y-direction (FIG. 4.5b and f) and others in the opposite (FIG. 4.5d). The results reveal that evaporation tends to delay the onset and evolution of the prevailing mode. FIG. 4.5b shows that the mode transition is completed by $t \cong 5\times10^4$ when phase change is disregarded. In the reference evaporating case (FIG. 4.5d), the prevailing mode requires more time to dominate the first, $t \cong 8 \times 10^4$. If the evaporation rate increases further (FIG. 4.5f), it is found that after the time span presented ($t \cong 1.5 \times 10^5$), the prevailing mode has not yet been able to suppress the first at the spanwise section under consideration. The non-linear mode keeps strengthening but both groups of HTWs still coexist as shown in FIG. 3.6. Thus, the pattern in FIG. 4.5f corresponds to the first mode solely, the bands are noticeably thinner if compared to those shown in FIG. 4.5b or d.

4.4.2 Constant layer depth

Preliminary comparisons between equivalent evaporating and non-evaporating systems revealed that the addition of phase change results in weaker T' but more pronounced z_i'. The direct link between HTWs and physical waves observed in non-evaporating layers, see FIG. 3.8, suggests that, in the evaporating case, there must be counteracting mechanisms absent for negligible evaporation. Otherwise, weaker HTWs should be accompanied by a flatter interface. To elucidate the physical mechanisms involved, we first consider a situation in which the layer depth remains constant rather than letting it decrease due to evaporation. This is not an unreasonable scenario, in an similar attempt to maintain a constant filling level, Schwabe *et al.* [14] put in place several countermeasures in their experiment MAGIA. From the theoretical point of view, the same effect is achieved setting $S = 0$ in equation (4.15), but not for the rest of the governing equations. This study is restricted to the prevailing mode, given than any linear mode is dominated by it sooner or later. To that end, T' and z_i' are instantaneously computed along the spanwise section at $x = 0$. Following the strategy described in chapter 3, a FFT is performed over the signals to ensure the correct capture of the maximum amplitudes. These are presented in FIG. 4.6.

In accordance with FIG. 4.5, FIG. 4.6 confirms that evaporation delays the onset of

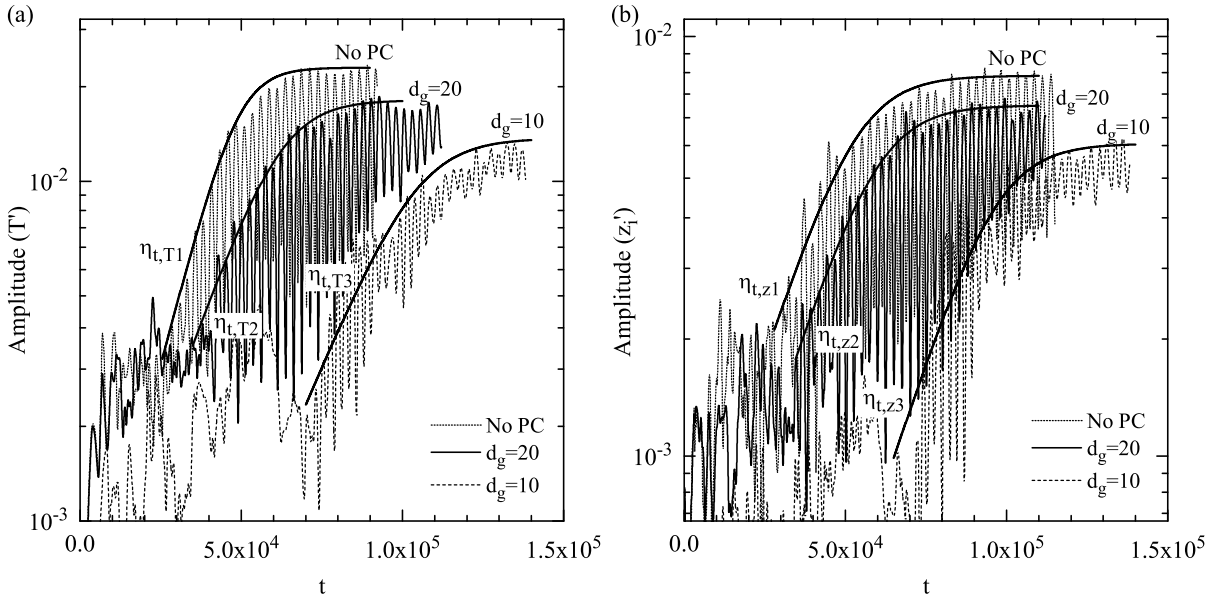

Figure 4.6: Instantaneous FFT analysis showing the amplitude of the fundamental mode for (a) the temperature T' and (b) the interface-height z_i' disturbances along the spanwise section at $x = 0$. The same case without phase change (No PC) is compared with others with increasing strength of evaporation, ($d_g = 20$ and 10). For the evaporation cases, $S = 0$ in equation (4.15) so that the liquid level is the same in the three cases. The parameters are the same as in FIG. 4.4.

the non-linear instabilities. Increasing the significance of evaporation leads to oscillatory modes of smaller amplitudes for both T' and z_i'. The maximum (saturation) amplitude for T' are $A(T')_{\mathrm{NoPC}} = 2.159 \times 10^{-2}$, $A(T')_{d_g=20} = 1.723 \times 10^{-2}$ and $A(T')_{d_g=10} = 1.323 \times 10^{-2}$ for the non-evaporating case, $d_g = 20$ and $d_g = 10$ respectively (FIG. 4.6a). In case of z_i', the corresponding amplitudes are $A(z_i')_{\mathrm{NoPC}} = 8.079 \times 10^{-3}$, $A(z_i')_{d_g=20} = 6.847 \times 10^{-3}$ and $A(z_i')_{d_g=10} = 5.529 \times 10^{-3}$ (FIG. 4.6b). The ratio of maximum amplitude in the evaporating case to that in the non-evaporating scenario yields $A(T')_{d_g=20}/A(T')_{\mathrm{NoPC}} = 0.80$ and $A(z_i')_{d_g=20}/A(z_i')_{\mathrm{NoPC}} = 0.84$ for $d_g = 20$. When phase change is stronger, $d_g = 10$, the same ratios become $A(T')_{d_g=10}/A(T')_{\mathrm{NoPC}} = 0.61$ and $A(z_i')_{d_g=10}/A(z_i')_{\mathrm{NoPC}} = 0.68$. In other words, when $\hat{d}$ is the same, the increasing prominence of evaporation stabilises both the HTWs and the physical waves. The fact that the ratios for T' and z_i' are very similar for $d_g = 20$ and 10 supports the fundamentally direct relationship existing between T' and z_i' suggested in FIG. 3.8.

The temporal growth rates η_t for the fundamental modes are revealed by fitting functions of the type $\varphi(t) = \varphi_0 e^{\eta_t t}$, which correspond to the initial linear segments in FIG. 4.6. It is found that $\eta_{t,T1} = 8.4 \times 10^{-5}$, $\eta_{t,T2} \cong 0.71\eta_{t,T1}$ and $\eta_{t,T3} \cong 0.62\eta_{t,T1}$ for the temperature and $\eta_{t,z1} \approx \eta_{t,z2} \approx \eta_{t,z3} \approx 5.4 \times 10^{-5}$ for the interface deformations. The

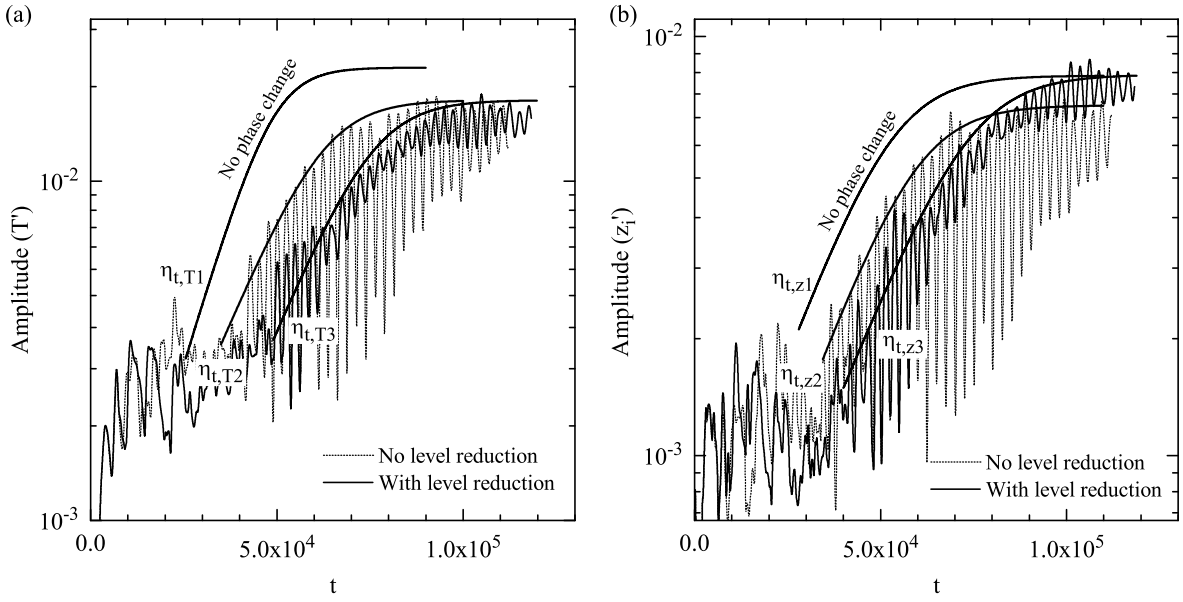

Figure 4.7: Instantaneous FFT analysis showing the amplitude of the fundamental mode for (a) the temperature T' and (b) the interface-height z_i' disturbances along the spanwise section at $x = 0$. The evaporating cases correspond to the reference system, i.e. $d_g = 20$. The parameters are the same as in FIG. 4.4.

conclusion that evaporation has stabilizing effects is therefore reinforced, given that η_t for T' decays for increasing $M(t)$. The growth rate for z_i' seems unaffected in this range.

4.4.3 Effects of liquid-level reduction

The effects brought about by the layer depression are examined by comparing the reference system without liquid consumption (introduced in the previous section) against the same case with transient level reduction, i.e. $S \neq 0$ in equation (4.15). The instantaneous fundamental amplitudes for T' and z_i' in both cases are presented in FIG. 4.7. The curves for the non-evaporating system have been included for reference. FIG. 4.7a reveals that the connection between the growth of HTWs and the actual layer level is minor. The resulting saturation amplitude is essentially the same in both cases, 1.723×10^{-2}, as well as the growth rates $\eta_{t,T2}$ and $\eta_{t,T3}$, 6×10^{-5}. The onset of the prevailing mode occurs slightly later in the new system. No conclusive behaviour can be deduced in this respect given that the period before the inception of the HTWs is very chaotic and exposed to numerous random non-linearities.

On the contrary, the interface deflections are noticeably more significant when the layer depth changes, FIG. 4.7b. The new maximum amplitude, 8.068×10^{-3}, is 18 %

larger than that for constant filling level. The fact that this amplitude is essentially the same as in the non-evaporating system is a mere coincidence found in this situation. In preliminary tests we observed cases subjected to stronger evaporation rates in which the interface deformations clearly overshoot those found in the equivalent non-evaporating system. The temporal growth rates are found to be unaffected again. Thus, the liquid-level reduction does not seem to impact the HTWs but it clearly enhances the physical waves. The experiments with spreading liquid films carried out by Kavehpour *et al.* [125] also reveal that the relative amplitude of the interface waves increases as the film thickness becomes smaller. This is due to the fact that a reduction in the layer thickness due to evaporation reduces the relative significance of gravity, which plays a stabilising role. It is therefore seen that phase change plays a dual role: it stabilises the flow by inhibiting the HTWs waves, while amplifying interfacial disturbances. The overall effect, however, is a stabilising one.

Showing a linear behaviour as in the model validation, the resulting evaporation rate, or rate of change of the mean interface height, $M(t)$ is 5.78×10^{-8} ($0.237\ \mu\mathrm{m\,s^{-1}}$) which is similar to the value measured in the experiments of Zhu & Liu [123] carried out with a slightly larger cavity. For $\Delta\hat{T} = 12\,^{\circ}\mathrm{C}$, figure 3 in [123] suggests an experimental $M(t)$ $O(0.18\text{-}0.19\ \mu\mathrm{m\,s^{-1}})$. The small deviation could be a result of the different aspect ratio of the test cell or, most probably, from the slightly different properties of the liquid.

A summary with the final characteristics of the HTWs is presented in TABLE 4.2. The slopes of the bands in the space-time diagrams shown in FIG. 4.5 provide c_R along the principal directions, i.e. $c_R^2 = c_{Rx}^2 + c_{Ry}^2$ with $c_{Rx} = \mathrm{d}x/\mathrm{d}t$ and $c_{Ry} = \mathrm{d}y/\mathrm{d}t$. Phase change does not have a significant impact on this parameter: $c_R = 1.71 \times 10^{-3} \pm 0.6\,\%$ was obtained for the evaporating and non-evaporating cases. The linear analysis by Smith & Davis [11] suggests $c_R = 1.36 \times 10^{-3}$ (converted to our dimensionless framework via the factor $\hat{b}_i\hat{d}/\Delta\hat{T}$). Regarding ψ, evaporation results in a slight increment, from $\psi = 55^{\circ}$ found when there is no phase change to $\psi = 58^{\circ}$ observed for the reference case. Smith & Davis [11] predict $\psi = 57^{\circ}$. To conclude, the wavenumber registers a small decrease, from $k = 1.02$ to 0.99 when the layer is undergoing evaporation in the reference case, while Smith & Davis [11] report $k = 1.52$. Thus, there is a good agreement even though this

	ψ	k	c_R
Smith & Davis [11]	57°	1.52	$1.36 \times 10^{-3*}$
Non-evaporating layer	55°	1.02	1.71×10^{-3}
Evaporating layer	58°	0.99	1.71×10^{-3}

Table 4.2: Effects of phase change on the characteristics of prevailing HTWs and comparison against the liner theory by Smith & Davis [11] (*Converted to our dimensionless framework). The phase speed is calculated from the slopes of bands in FIG. 4.5.

validation compares results from linear theory [11] against the prevailing mode once this is well-developed.

4.5 Gas Dynamics in the Unstable Regime

In section 4.3 it was shown that phase change has little effect on the liquid base state. Thus, no noteworthy alteration is found in the dynamics of bulk of the lower phase. The reader is referred to section 3.3.3 for more details in this respect. For the gas phase, on the other hand, the work presented in chapter 3 can be improved here. This was conducted with a more modest H, without evaporation and, consequently, without the non-uniform vapour distribution considered in this investigation. Especially interesting is the local evaporation mechanism, which is significantly altered by the HTWs. FIG. 4.8a shows the disturbance signals for the temperature T', evaporation flux S' and vapour mass fraction ω' along the same spanwise section as that considered in FIG. 4.5, i.e. x = -11. The results presented correspond to the reference case, $d_g = 20$. To provide more illustrative results, S' is expressed as a flux J' per unit horizontal area ($\mathrm{kg\,s^{-1}\,m^{-2}}$) taking into consideration the fact that the interface is essentially flat: $\mathrm{d}V = \mathrm{d}x \times \mathrm{d}y \times \mathrm{d}z$ and $\mathrm{d}A = \mathrm{d}x \times \mathrm{d}y$, therefore $J' = S'\,\mathrm{d}V/\mathrm{d}A$ with $\mathrm{d}V/\mathrm{d}A = \mathrm{d}z$. T' and ω' are intimately related in accordance with the prerequisite that the interface should remain saturated at the local temperature. According to our model, in order for evaporation to take place the instantaneous local pressure should be slightly lower than the saturation pressure. Otherwise there would not be any interface mass transfer. Indeed it is found that, for the section under consideration, there is a deviation between the actual ω and the saturation ω_s mass fractions, its maximum is less than 0.37% of ω_s. J' also denotes

that the evaporation flux is subjected to the HTW-oscillatory behaviour. The T' and J' signals are spatially delayed approximately 10% of the spanwise wavelength with the latter pursuing the former. The fact that the profiles are out-of-phase suggests that there is a secondary phenomenon involved in the phase change mechanism. It will be shown that this is related to the convective patterns induced by the instabilities in the gas.

The vapour distribution in the gas mixture is presented in FIG. 4.8b. The mass fraction decreases from saturation conditions at the interface to zero at the opening, $z = 21$. The ω-contour lines above $z = 5$ are parallel to the y-direction indicating that the vapour field becomes spanwise-independent above this point. Near the interface, $z < 5$, the contour lines display a wavy pattern which reveals that the HTWs also induce oscillatory features in ω. This pattern propagates with the instabilities in the y-positive direction. Unexpectedly, the high-concentration areas are found above J' and T' minima. For instance, FIG. 4.8a shows that the evaporation flux is minimum around y = -0.2, while FIG. 4.8b indicates that the gas above this point (at around $z > 1.5$) corresponds to a high-concentration region. To explain this, the gas streamlines are presented in FIG. 4.8c. The plot confirms that the HTWs generate pairs of counter-rotating rolls in the upper phase as speculated in section 3.3.3. The actual rolls are oblique, with their axes parallel to the HTW fronts. The midpoints between each pair of rolls correspond to the regions of either maximum or minimum J'. This observation suggests that the phase mismatch between T' and J' observed in FIG. 4.8a is caused by the instability-induced advection in the gas. Taking y = -0.2 as reference to illustrate the mechanism, the streamlines around both sides of this point indicate that there is a significant convection parallel to the interface towards it. Given that the gas phase is a mixture, noteworthy amounts of vapour are being transported with the fluid's bulk motion. This advection transport results in vapour accumulation where the streamlines meet, i.e. y = -0.2, and vapour depressions around the opposite side of the counter-rotating rolls, i.e. $y \cong 3.5$ and -4.5.

A more insightful description of this phenomenon is possible by subtracting the base state so that only ω' and T' are visible, FIG. 4.9. The fluctuations (at $z > 1.5$) are out-of-phase almost by half a wavelength. At and in the immediate vicinity to the interface, ω' is in phase with T'. This is in agreement with the comments regarding FIG. 4.8a and

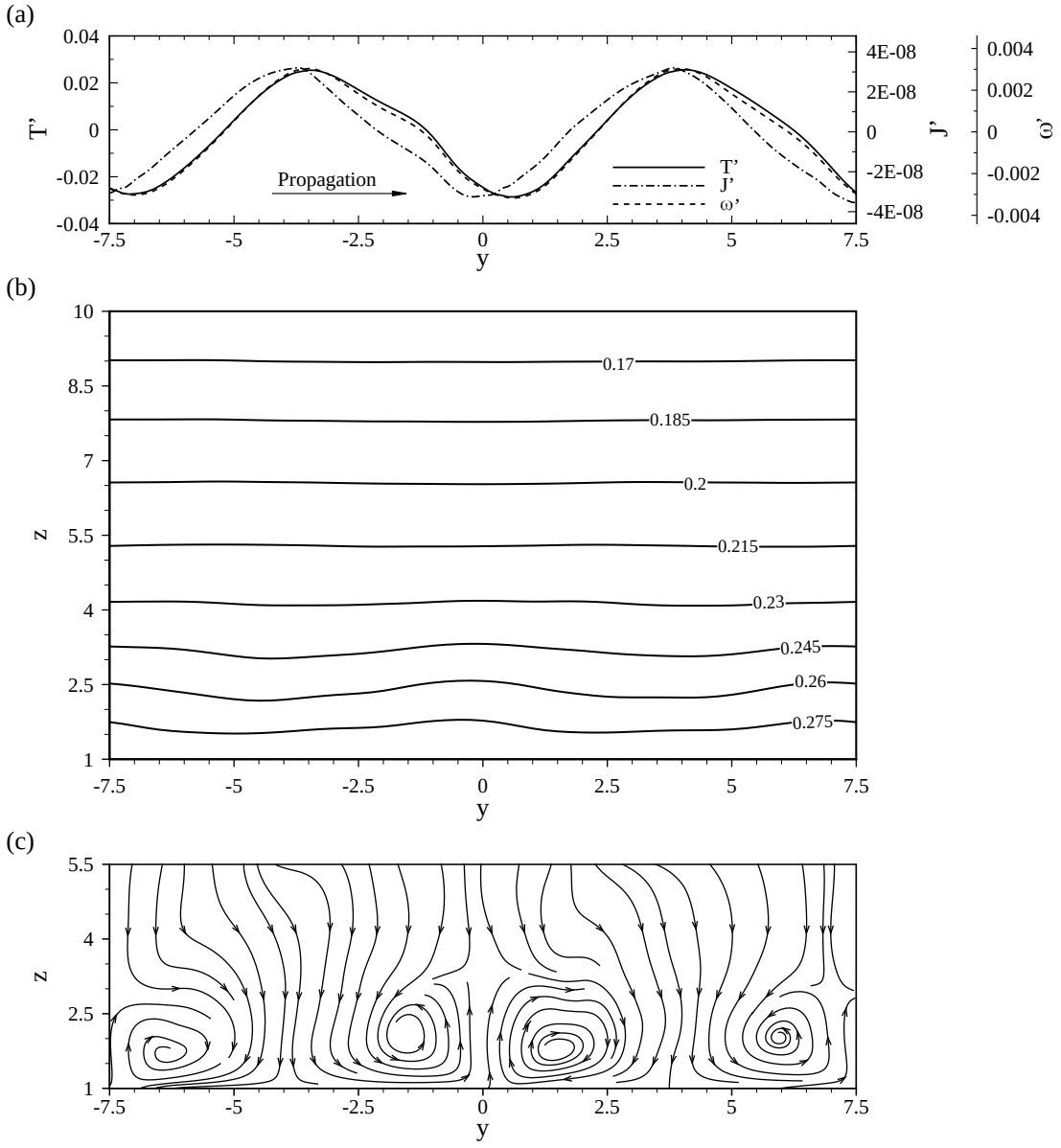

Figure 4.8: Effects of the prevailing mode in the dynamics of the gas phase along the spanwise section with x = -11. (a) Interface temperature T', evaporation flux J' and vapour mass fraction ω' disturbances; (b) vapour distribution ω and (c) streamlines. The results correspond to the reference case, $d_g = 20$, once the prevailing mode is fully developed, $t = 1.54 \times 10^5$. The parameters are the same as in FIG. 4.4.

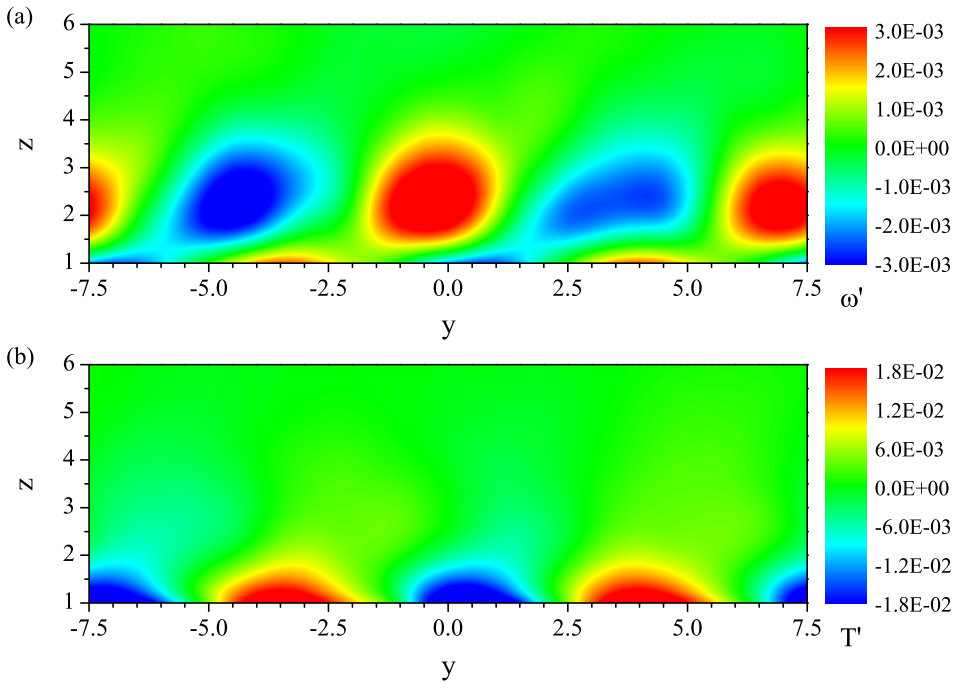

Figure 4.9: (a) Mass fraction ω' and (b) temperature T' disturbances in the gas phase along the section examined in FIG. 4.8. The fluctuations propagate in the y-positive direction.

reinforces the idea that the ω- and T-fluctuations are tightly related at the interface by virtue of p_s. However, as these signals propagate away from the interface, the HTW-induced rolls decouple them and high vapour-concentration regions appear above cold spots as explained in FIG. 4.8. FIG. 4.9 also reveals the disparity between ω' and T' in terms of spatial extension. The fluctuations in ω reach $z \cong 4$ before they dissipate, whereas those in T are negligible beyond $z \cong 2$. Thus, the spatial extension of ω' is roughly two times larger than that of T'. The vapour field is more sensitive to the instabilities than the thermal field in this sense. Given that the underlying flow is the same for ω and T, the origin of these differences is due to the competition between the thermal and molecular diffusivity (represented by the Lewis number) and the competition between the momentum and molecular diffusivity (represented by the Schmidt number). The T'-maximums are located at the interface, $z \cong 1$, while ω'-maximums occur around $z \cong 2.5$ and the former is one order of magnitude smaller that the latter. As shown in FIG. 4.10, the instantaneous FFT analysis of T' and ω' at the interface and for the gas above it ($z = 2.5$), exposes that the temporal development of the oscillatory regime in ω is directly connected to the growth of the instabilities. The two-stage behaviour observed in T' at the interface, corresponding to the first and prevailing modes, is transmitted to

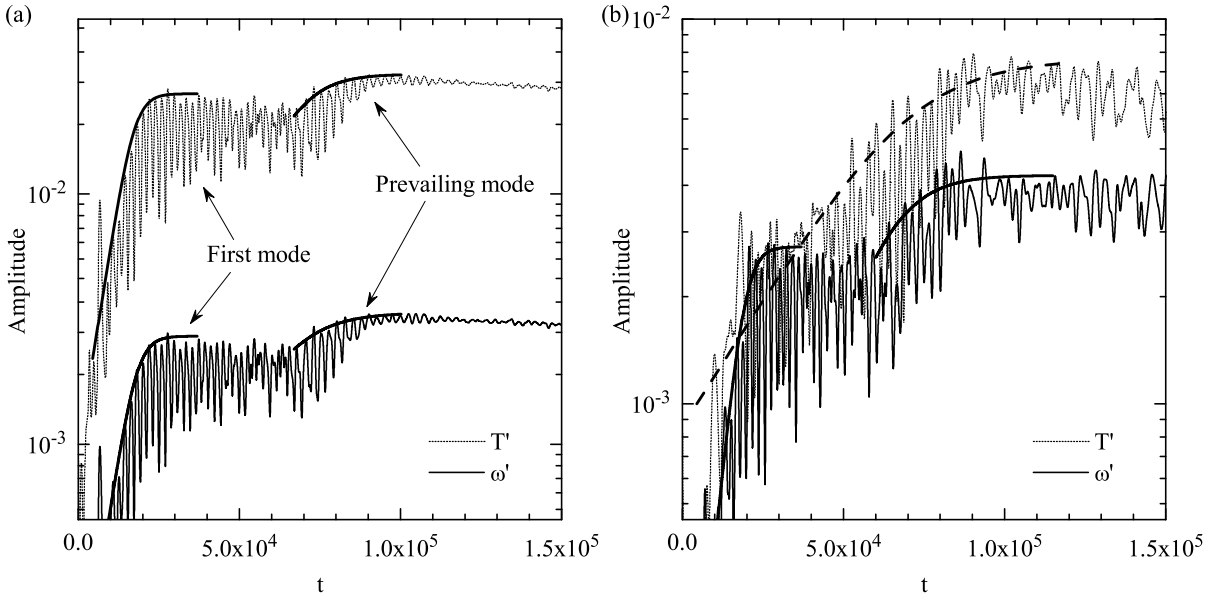

Figure 4.10: Instantaneous FFT analysis showing the fundamental mode for the temperature T' and concentration field ω' disturbances (a) at the interface and (b) in the gas above it ($z = 2.5$). The results correspond to the reference case for the same spanwise section as that examined in FIG. 4.8.

ω' for both locations but not to T' at $z = 2.5$. Thus, the fluctuations in the vapour field in the immediate vicinity to the interface are enslaved to the HTWs. The fundamental amplitude for ω' is of the same order at the interface and in the bulk of the gas but the signal is more inconsistent away from the interface.

These mechanisms are analysed in the streamwise direction with similar figures, i.e. FIG. 4.11 and FIG. 4.12. As it was perceived along the spanwise direction, the ω' and T' along the interface are essentially superposed signals, which highlights their direct relationship, FIG. 4.11a. However, here it is more evident that the connection between the evaporation flux and the interface temperature (or vapour pressure) is not so intimate. The J fluctuations towards the cold wall (positive x) are comparatively weaker and do not follow T' so closely. This effect mainly results from the convective transport of ω in the gas along the interface by other patterns illustrated by the streamlines in FIG. 4.11c. In general, the rolls along this direction are complex because the flow is deep into the unstable non-linear regime. The confinement in the streamwise direction also contributes to the flow disruption. The recirculation of the fluid when this collides against the cold wall is not smooth and results in stagnant areas and other pattern interferences. It should be noted that the projection of the counter rotating rolls reported in FIG. 4.8c is not evident in FIG. 4.11c because the disturbances are masked here by the base streamwise flow

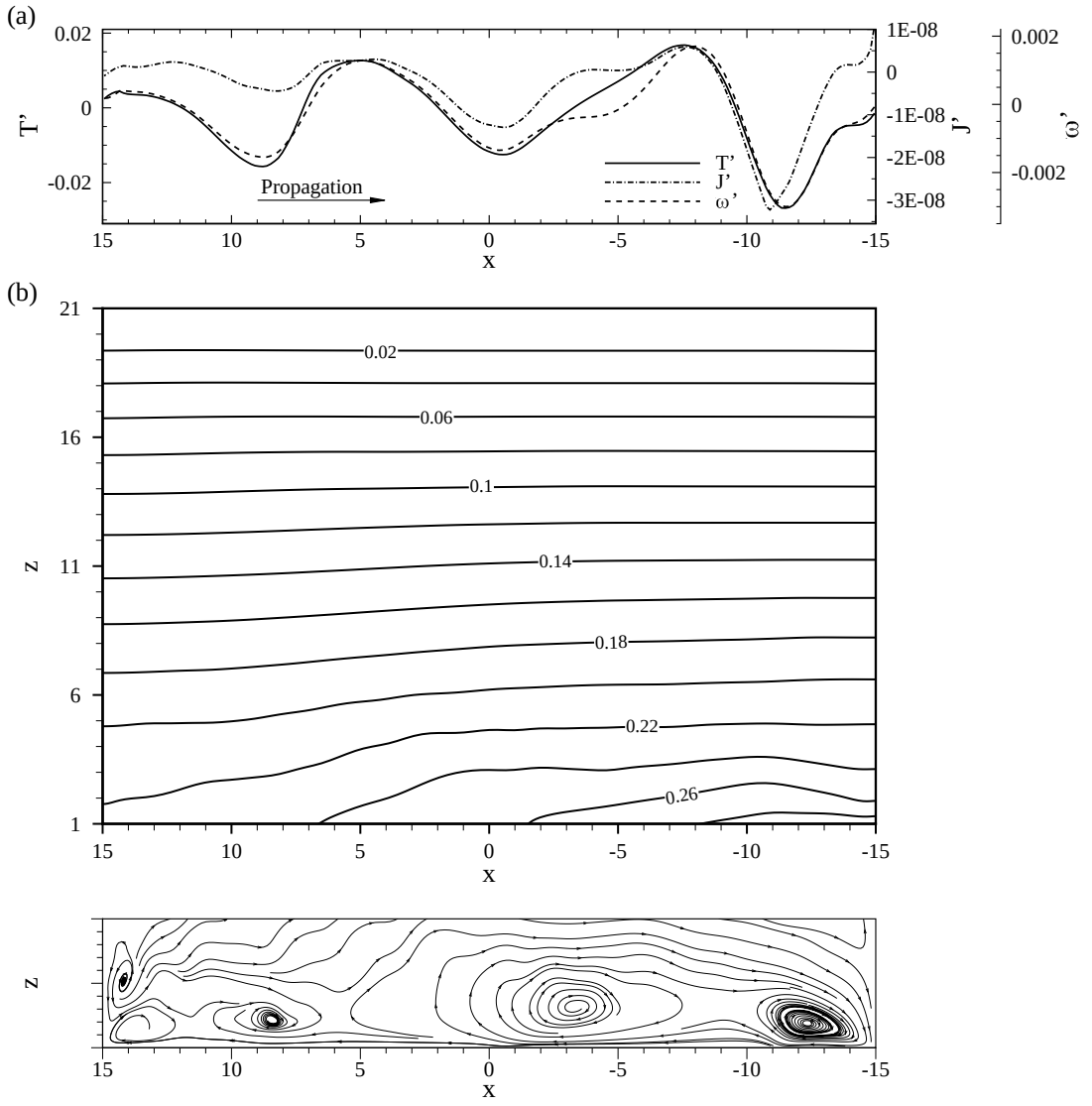

Figure 4.11: Effects of the prevailing mode in the dynamics of the gas phase along the central streamwise section. (a) Interface temperature T', evaporation flux J' and vapour mass fraction ω' disturbances; (b) vapour distribution ω and (c) streamlines. The results correspond to the reference case, $d_g = 20$, once the prevailing mode is fully developed, $t = 1.54 \times 10^5$. The parameters are the same as in FIG. 4.4.

(much stronger). The flow remains motionless for $z > 6$ which supports the assumption made during the model exposition that diffusion is the rate-limiting mechanism for phase change.

Equivalent conclusions to those drawn from FIG. 4.9 can be obtained with ω' and T' along streamwise section presented in FIG. 4.12. The analysis will not be repeated here. It should only be pointed out that the large pattern observed above $0 < x < 5$ is attributed to the disturbances and confinement effects above discussed. The features near the hot wall, where the flow inversion has a weaker disordering influence, resemble more closely those observed in the spanwise direction.

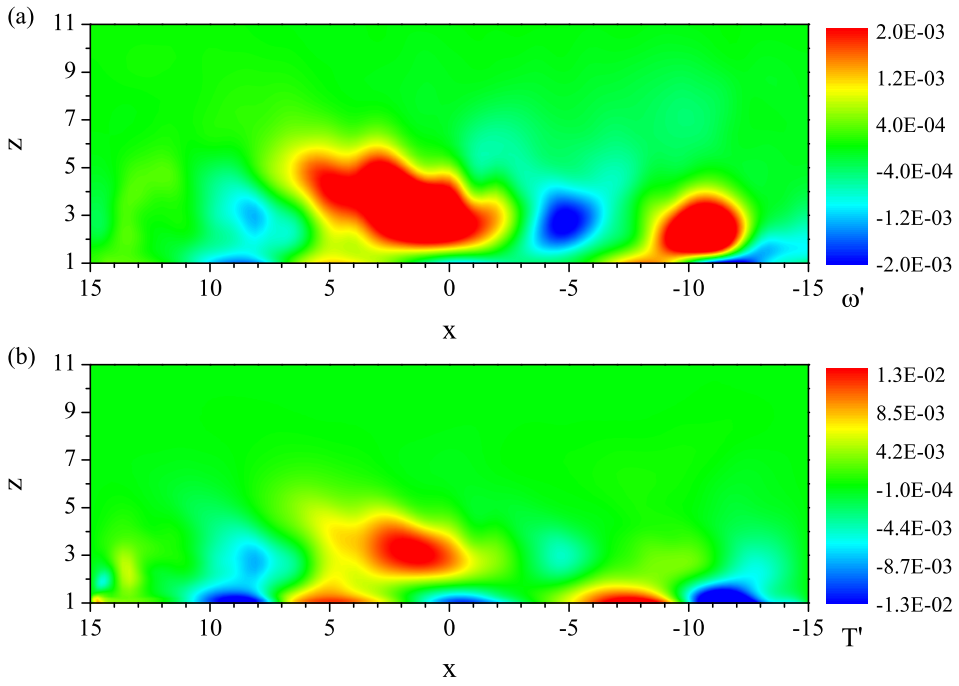

Figure 4.12: (a) Mass fraction ω' and (b) temperature T' disturbances in the gas phase along the section examined in FIG. 4.11. The fluctuations propagate in the x-negative direction.

4.6 Base Evaporation - Stable Regimes

Following the main aim of this investigation, the assessment of the evaporation effects on the HTWs, the phase-change mechanisms have been investigated in previous sections in its disturbance form, equation (3.22). Nonetheless, substantial knowledge can be additionally extracted from examining the base evaporation state, i.e. the phase-change process found in liquid layers without HTWs. Furthermore, to illustrate the effects of the thermocapillary convection on the local evaporation flux J and on the vapour distribution ω, the reference case is compared with an equivalent system in which the Marangoni effect is neglected, i.e. $\hat{\gamma} = 0$. If the minor role of gravity is also disregarded to provide a more insightful comparison, the two-phase flow becomes motionless ($\mathbf{u} = 0$) and diffusion is the only transport mechanism possible for T and ω. In what follows, this configuration is referred to as *diffusion case*.

This new scenario is computed by solving a simplified subset of the governing equation

presented in section 4.1.2:

$$\begin{aligned} \frac{\partial c}{\partial t} &= \text{-}S, \\ \frac{\partial \left(\rho c_p T\right)}{\partial t} &= \frac{1}{Re_d Pr}\nabla \cdot \left(k\nabla T\right) - \frac{1}{Ja}S, \\ \frac{\partial \left[\rho_g \left(1-c\right)\omega\right]}{\partial t} &= \frac{1}{Re_d Sc}\nabla \cdot \left[\rho_g \left(1-c\right)\nabla\omega\right] + S, \end{aligned} \tag{4.30}$$

where the scalings for time and pressure have been redefined to $\hat{\mu}_l\hat{d}/\hat{\sigma}_r$ and $\hat{\sigma}_r/\hat{d}$, respectively, so that the set of equations does not depend on $\hat{\gamma}$. This consideration leads to new definitions of Re and $\mathscr{P}$, namely,

$$Re_d = \frac{\hat{\sigma}_r\hat{d}}{\hat{\mu}_l\hat{\nu}_l} \qquad \text{and} \qquad \mathscr{P}_d = \frac{\hat{\sigma}_r}{\hat{p}_r\hat{d}}, \tag{4.31}$$

which can be related to the original as $Re_d = Re/Ca$ and $\mathscr{P}_d = \mathscr{P}/Ca$. Thus, the parameters for the diffusion case are $Pr = 0.75$, $Re_d = 1.89 \times 10^5$, $Sc = 0.06$, $Ja = 0.11$, $\mathscr{P}_d = 1.70 \times 10^{-4}$, $\mathscr{M} = 5.6$, $\Gamma_\rho = 640$, $\Gamma_k = 70$, $\Gamma_{cp} = 2$, $\Omega_\rho = 100$, $\Omega_k = 66$ and $\Omega_{cp} = 1.34$.

This new case quickly evolves towards a quasi-steady state almost equal to that resulting from pure steady-state diffusion, i.e. $\nabla^2 T = 0$ and $\nabla^2\omega = 0$. The results are exactly the same when the liquid consumption is disregarded. FIG. 4.13a compares ω for the diffusion and reference cases, the latter with thermocapillarity. In both, ω is non-uniform with higher-concentration regions located where the liquid is warmer. Nonetheless, the contour lines for the Marangoni-driven layer (dashed lines) reveal a comparatively vapour accumulation next to the cold wall and a depression next the other boundary. These results are interpreted with the help of base flow induced in the gas by thermocapillarity, FIG. 4.14. Note that this base state is that shown in FIG. 4.11c without the disruptions generated by the HTWs. The relevance of this flow is manifested by its speed, comparable to the maximum found at the interface. The streamlines next to the liquid-gas boundary travel towards the cold wall, where they are inverted generating the recirculation flow presented in FIG. 4.14. $\mathbf{u} \cong 0$ for $z > 6$. This flow is responsible for the vapour accumulations and depressions detected in FIG. 4.13a. There is a major ω advection parallel to the

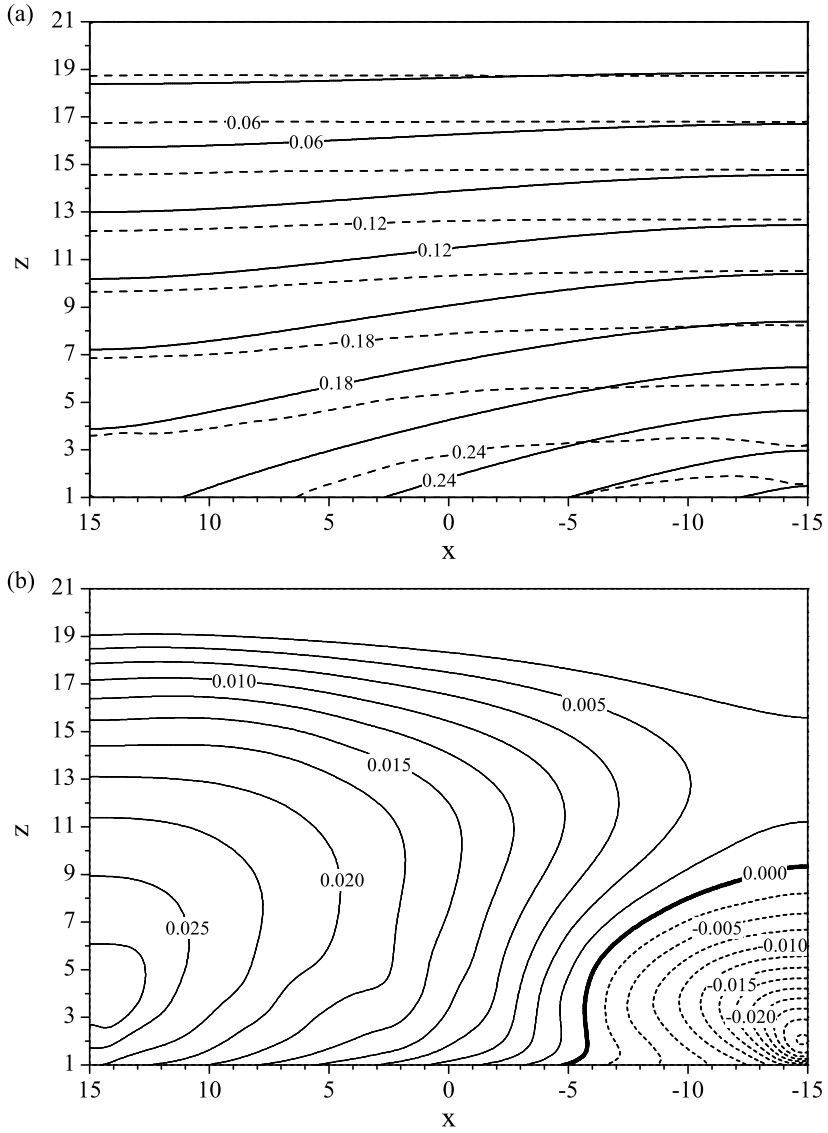

Figure 4.13: Base vapour distribution. (a) ω for the reference case (with thermocapillary convection) (dashed contours) and for the diffusive case (solid contours); (b) Mass-fraction difference (reference minus diffusion). The parameters for the diffusive case are $Pr = 0.75$, $Re_d = 1.89 \times 10^5$, $Sc = 0.06$, $Ja = 0.11$, $\mathscr{P}_d = 1.70 \times 10^{-4}$, $\mathscr{M} = 5.6$, $\Gamma_\rho = 640$, $\Gamma_k = 70$, $\Gamma_{cp} = 2$, $\Omega_\rho = 100$, $\Omega_k = 66$ and $\Omega_{cp} = 1.34$. The parameters for the reference case are the same as in FIG. 4.4.

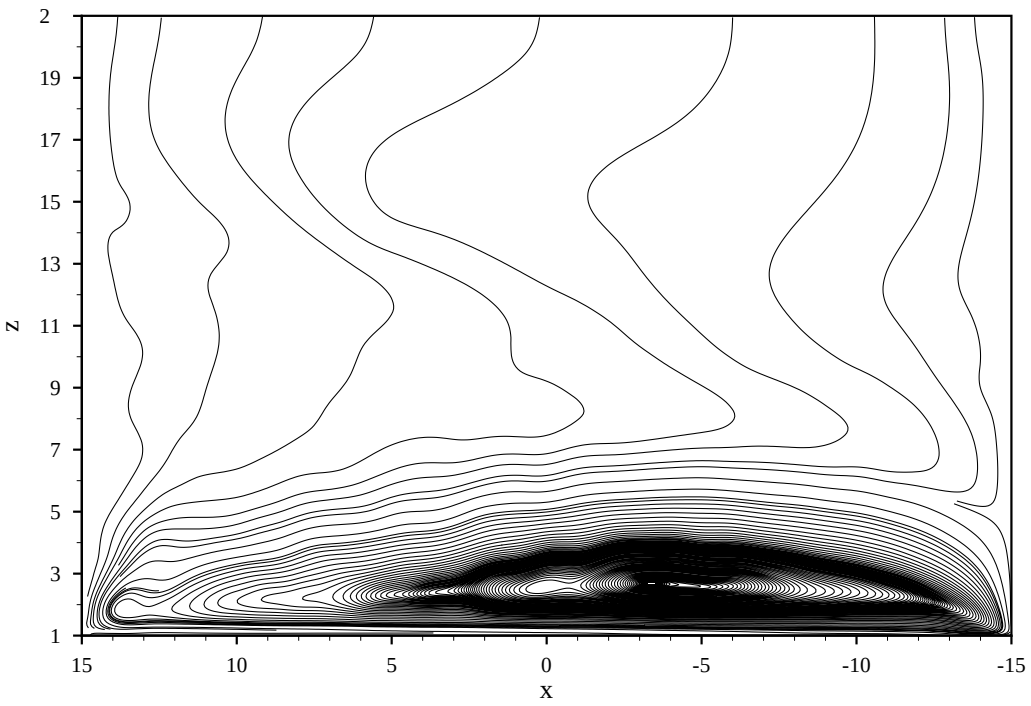

Figure 4.14: Streamlines illustrating the base gas flow induced by the Marangoni effect. The direction of the streamlines right next to the interface is the x-positive. The parameters are the same as in FIG. 4.4.

interface which drags vapour from the hot area and brings it to the cold boundary. Thus, the Marangoni effect leads to the vacuum effect observed next to the hot wall in FIG. 4.13a and to the vapour accumulations found at the cold boundary. A more illustrative notion on how ω compares in the reference and diffusion cases is achieved by subtracting the latter from the former as shown in FIG. 4.13b.

The streamwise J and T profiles are presented in FIG. 4.15. For the diffusion case, FIG. 4.15a, the resulting T is essentially linear, even though the $\Delta\hat{h}_v$ consumption is accounted for, and J grows smoothly with it. The comparatively larger flux found near the hot wall simply appears to compensate the missing diffusive contribution in the x-positive direction impeded by the boundary. The opposite effect explains the almost zero flux near the cold boundary. Leaving out these confinement effects and focusing on the centre of the layer, the important conclusion to extract is that J and T are directly related in the diffusion case, i.e. as the temperature grows, so it does the interface mass-transfer rate. Nevertheless, the same is not observed when there is Marangoni flow as shown in FIG. 4.15b. Here, there are regions in which J decreases even though T grows uniformly in the x-negative direction. The advection transport of ω along the interface results in

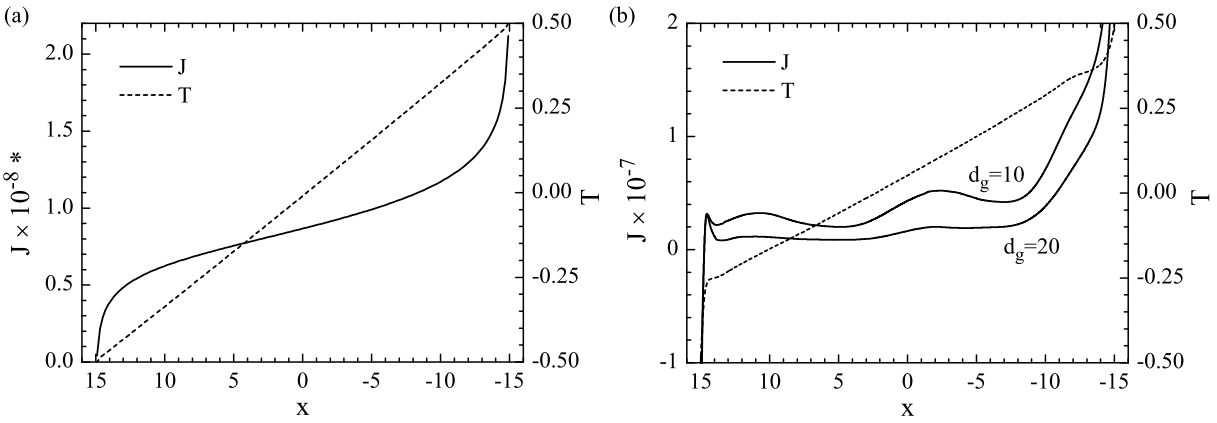

Figure 4.15: Evaporation flux and temperature along the interface for the (a) diffusion and (b) reference cases. ($^*J$ in (a) has been converted to the dimensionless framework of the reference case, via the factor $1/Ca$, to allow direct comparison with (b)). The evaporation flux for $d_g = 10$ has been included in (b) for illustration purposes. The parameters are the same as in FIG. 4.13.

that less new vapour is required downstream to maintain the interface saturated. The extreme cases of this phenomenon are found at the boundaries. J is much larger near the hot wall to compensate this thermocapillary-driven vacuum effect. On the other hand, the amount of vapour transported downstream is so important that the vapour pressure near the wall exceeds p_s leading to the inversion of the phase change, $J < 0$ in FIG. 4.15b, i.e. there are condensation traces at interface next to the cold region. FIG. 4.16 shows the difference between the saturation mass fraction ω_s at the local T and the actual mass fraction ω (dashed contours in FIG. 4.13a) in the bulk of the gas corresponding to the reference case. Near the cold boundary, there is a relatively large region where $\omega > \omega_s$ suggesting that there should be additional condensation along the vertical wall up to roughly $5\hat{d}$, to be exact $z \leq 4.8$. For the diffusion case, $\omega \leq \omega_s$ everywhere in the gas phase and $M(t) = 1.02 \times 10^{-8}$ ($0.042\ \mu\mathrm{m\,s^{-1}}$), which indicates that thermocapillarity also increases the overall strength of the phase-change process.

4.7 Conclusions

The effects of phase change on the HTWs have been investigated for the first time using an upgraded version of the model presented in chapter 3. Typical simplifications in the dynamics of the gas have been obviated by implementing a general advection-diffusion transport equation for the vapour. Phase change models based on steady-state vapour

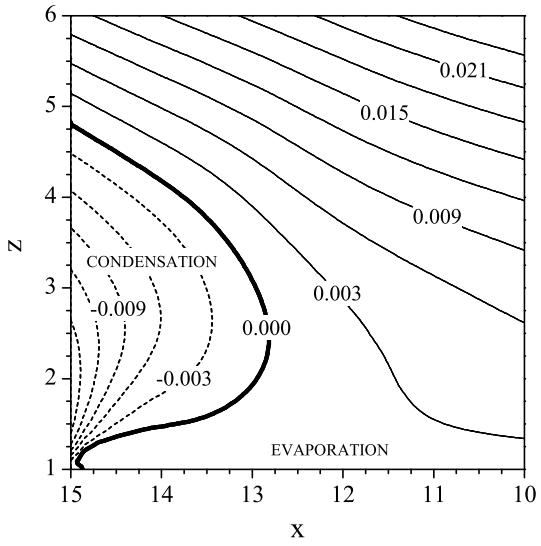

Figure 4.16: Difference between the saturation mass fraction ω_s at the local temperature and the actual mass fraction ω near the cold wall for the reference case. Dashed contours show the region where the actual vapour pressure exceeds the saturation pressure. For the rest of gas phase (not shown here) $\omega \leq \omega_s$. The parameters are the same as in FIG. 4.4.

diffusion, i.e. Laplace's equation, have been widely used in the past which entailed that the species distribution above the interface is unaffected by advection mechanisms. The present work demonstrates that this is insufficient for Marangoni-driven flows, thereby highlighting the deficiencies of previous and more simplified approaches. Thermocapillary convection plays a major role in both the vapour field and the local evaporation flux across the interface. The strength of the model is supported by the excellent agreement (FIG. 4.3) observed with experimental work [123] in addition to the validation presented in chapter 3 against the stability theory by Smith & Davis [11] and the experiments by Riley & Neitzel [40].

The impact of phase change on the liquid base state is minor. The cooling effect of evaporation does not lead to significant alterations in the streamwise temperature signature, given that the thermal field is strongly enforced by the differentially heated end-walls. Nonetheless, phase change does play a substantial role in the development of the hydrothermal waves (HTWs). Focusing on the non-linear regime (prevailing mode), the space-time diagrams reveal the stabilising effect of evaporation in the spatial development of the instabilities throughout the liquid layer. This effect is supported by the analysis of the oscillatory signals for layers subjected to different evaporation strengths. As the mass-transfer rate increases, the saturation amplitude and temporal growth rate of the

HTWs decay. The opposite behaviour is found for the physical waves previously reported. These interfacial deformations travelling with the thermal disturbances are enhanced by evaporation due to the associated level reduction that reduces the stabilising effect of gravity. Thus, it is concluded that evaporation plays a dual role in the stability of thin layers driven by thermocapillarity. The latent energy required during the evaporation process tends to inhibit the HTWs while the accompanying level reduction promotes the physical waves by minimizing the role of gravity.

The dynamics of the gas phase within the unstable regime has also been examined. The interfacial instabilities generate oscillatory features in the local evaporation flux, temperature and vapour concentration above the liquid-gas interface. These are noticeable along the spanwise and streamwise directions. The complexity of the gas dynamics is increased by the pairs of counter-rotating rolls induced by the HTWs. These rolls decouple the vapour concentration at the interface, tightly related to the thermal fluctuations, and that above it. This previously unreported mechanism results in the unanticipated effect that high vapour-concentration regions appear above cold spots and vice versa.

This investigation is concluded by exploring the role of the Marangoni effect in the phase-change dynamics of liquid layers not subjected to any instability, i.e. stable regimes. The evaporating base state has been compared to that of the same system without the temperature-dependence of the surface tension, i.e. diffusion is the only transport mechanism. It is shown that the Marangoni effect has a significant effect on the vapour field above the interface as well as on the local evaporation flux. The thermocapillary convection induces large recirculation currents in the gas which disrupt the steady diffusion distribution resulting in vapour build-ups and depressions near the cold and hot walls, respectively. This Marangoni-driven effect also alters the local evaporation flux along the interface and results in the vapour pressure next to the cold wall exceeding the saturation pressure. In other words, it leads to condensation in an essentially evaporating liquid layer.

Chapter 5

Experiments on Evaporating Drops

In previous chapters, this work focused on examining the dynamics and stability of thermocapillary driven flows encountered in liquid layers vertically bounded by differentially-heated walls. Similar observations are also reported in evaporating sessile droplets. Elucidating the underlying dynamics of the latter has attracted a great deal of attention since they are central to a large number of technological and biomedical applications involving heat and mass transport. A number of examples are given in Chapter 1.

In contrast to what happens in the liquid-pool configuration investigated earlier in Chapters 3 and 4, wherein the interface thermal gradient responsible for the fluid motion is externally imposed and the film thickness is kept constant, here temperature gradients are a natural consequence of the evaporation process. In addition, these vary both spatially and temporally along the interface of the drop with variable thickness (shape). It is important to note that, although spontaneously occurring, the resulting temperature imbalances at the interface can still compromise the stability of the flow within drops. This has been shown recently in the experimental work carried out by Sefiane *et al.* [66] which first revealed self-excited HTWs in ethanol and methanol drops.

The sessile-drop problem is significantly more complex because of the spherical or spheroidal geometry, the nonuniform evaporation flux along the interface and, especially, the intricate contact-line dynamics. In order to gather experimental data on this problem, experiments were performed with evaporating drops placed on heated substrates. To that end, an experimental apparatus is designed which allows measurements of the evolution

and dynamics of these drops as they undergo phase change. These experiments are also used to obtain valuable data which will be later exploited to validate the accompanying numerical work presented in Chapter 6 of this Thesis.

5.1 Experimental Set-up

An experimental apparatus is designed to measure the profile of evaporating drops using optical techniques. A schematic of the experimental set-up is presented in FIG. 5.1. Very small droplets ($\hat{V}_0 \sim 10\,\mu$L) of distilled water are gently deposited on a heated substrate, allowed to evaporate and simultaneously recorded from the side by a CCD camera and from the top by an IR camera. The substrate is a copper cylinder of dimensions 3.8 cm diameter and 3.8 cm length. This is maintained at constant temperature, $\hat{T}_w$, by means of a cartridge heater inserted within the cylinder from below (Omega CSS-10120/120V, 20W, 2.54 cm length and 0.64 cm diameter), a PID controller $\pm 0.2\,^{\circ}$C (Omega CN77544-A2) and a K-type thermocouple located in a small orifice 6 mm below the substrate's upper surface. Copper and the cylinder's dimensions are chosen to provide a substrate with very high thermal conductivity as well as very large thermal mass so that the surface remains faithfully isothermal throughout the evaporation process. To ensure a smooth finish, the copper substrate was progressively ground and polished (with 0.05 μm colloidal alumina suspension in the final stage). The emissivity coefficients for water and polished copper are $\epsilon = 0.96$ and 0.03, respectively, which results in high-contrast IR images wherein the interface temperature is very accurate and the contact line is sharply defined. The size of the droplets is controlled via the pipette tip size, tube diameter and peristaltic pump speed. In order to avoid imprecision in assessing the composition (physical properties) and relative humidity (driving force) of the air surrounding the droplet, the substrate and dossing mechanism are placed within a closed cubic chamber made out of Plexiglass® (dimensions $20\times20\times20$ cm and 0.54 cm wall thickness). This is maintained at atmospheric pressure. A system of valves is attached to this chamber to allow the replacement of the initial normal air by pure Nitrogen (N_2). In addition, the use of a closed chamber guarantees that the evaporation process is not distorted by externally-induced convection

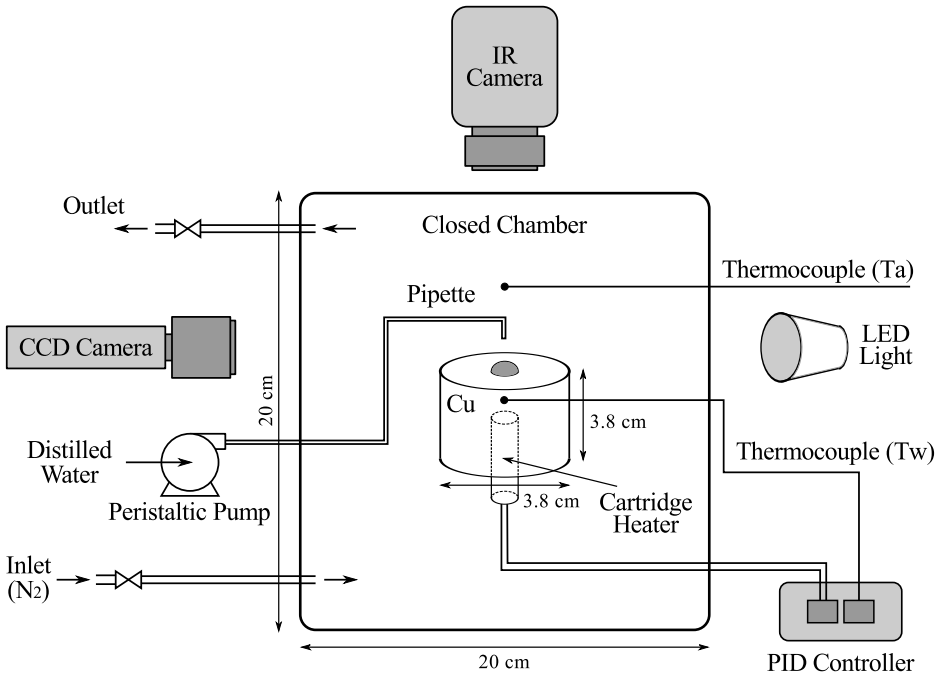

Figure 5.1: Sketch of the experimental test chamber.

currents and that the infra-red readings are not contaminated by any radiation from the surroundings, since plastic is opaque in the spectrum range of our IR camera. Inner reflections are also minimised by spray painting in black the interior of the chamber, except for two small gaps on opposite sides to allow the CCD recording and back-lighting of the drops, respectively.

The droplet profiles are captured with a CCD camera (900×600 pixels), capable of recording up to 30 frames per second, connected to a video-digitizer board (frame grabber). LED back-lighting is employed to improve the video's contrast without raising the temperature. The recorded side images are later post-processed with the help of the software Droplet Shape Analyser from Krüss (DSA v1.9, Krüss GmbH, Hamburgh, Germany) in order to obtain the instantaneous height $\hat{H}$, contact angle θ, base radius $\hat{R}$ and volume $\hat{V}$ throughout the evaporation process. Simultaneously, a mid-wave IR camera mounted directly above the substrate and facing vertically downwards onto the drop (FLIR Silver SC55600, spectrum range 3-5 μm, 640×512 pixels, 100 fps) is used to record the interface temperature field and contact-line dynamics. A cylindrical blackbody as that described in [126] is used to calibrate the infrared readings. Examples of the CCD

and IR recordings are presented in FIG. 5.2 and FIG. 5.3.

Before every new experimental run, N_2 is blown through the chamber for a sufficiently-long period of time to make sure that this is the only gas present within the test cell. After this, the inlet and outlet valves are closed and the system is let to rest until it reaches equilibrium conditions. Steady state is recognised by means of a secondary thermocouple located in the gas, 3.5 cm above the heated substrate, which also provides the real "bulk" or "ambient" temperature, $\hat{T}_a$. Only after the system is at equilibrium, detected when $\hat{T}_a$ becomes steady, a single droplet is released onto the heated surface and the recoding process begins. This procedure is repeated for every drop considered in this investigation to ensure consistency.

5.2 Results and Discussion

5.2.1 Typical evaporation process

The evaporation of water droplets on a heated copper substrate is investigated in the range of temperatures $\hat{T}_w = 35 - 90\,^{\circ}\mathrm{C}$. Special care is taken to release drops of the same characteristics at all times. The average initial height and base radius of the drops are $\hat{H}_0 \sim 1.55\,\mathrm{mm}$ and $\hat{R}_0 \sim 1.86\,\mathrm{mm}$, respectively. This leads to droplets of initial volume $\hat{V}_0 \sim 10\,\mu\mathrm{L}$ forming a contact angle $\theta_0 \sim 80^{\circ}$. Droplets outside this range of parameters were dismissed. For each heat level, the experiment procedure was repeated at least five times to ensure reproducibility of results. The typical evaporation time ranges between 150 - 900 s depending on $\hat{T}_w$.

The role of gravity relative to surface tension is assessed via the capillary length, i.e.,

$$\hat{\lambda}_c = \sqrt{\frac{\hat{\sigma}}{\hat{g}\hat{\rho}_l}}, \tag{5.1}$$

where $\hat{\sigma}$ is the surface tension, $\hat{g}$ denotes the magnitude of the gravitational acceleration and $\hat{\rho}_l$ is the density of the liquid. This quantity represents the spatial extent over which capillary stresses (surface energy) are predominant over gravity forces (bulk energy). For water under normal gravity conditions $\hat{\lambda}_c = 2.73\,\mathrm{mm}$. Since $\hat{H}_0 < \hat{\lambda}_c$, it may be concluded

that gravity effects are negligible for the cases studied here. The droplets essentially take the shape of spherical caps.

Depending on the liquid under consideration, the solid surface properties, the temperature, etc., the evaporation of a sessile droplet may occur following different scenarios. In their pioneering work [78], Picknett & Bexon observed that the evaporation rate (or lifetime) of the drops depends on the initial (equilibrium) contact angle θ_0. In general, for the same θ_0, the lifetime of a drop evaporating in the constant radius (CR) mode, θ decreases with time while $\hat{R} = \hat{R}_0$, is shorter than that of same drop if it were evaporating in the constant angle (CA) mode, $\theta = \theta_0$ while $\hat{R}$ decreases with time. Nonetheless, it is important to note that these two modes are seldom found in their pure forms in practical situations. More recent works such as by Shanahan *et al.* [95], Orejón *et al.* [100] or Nguyen *et al.* [127] show that in the majority of cases the real evaporation mechanism is a combination of the two pure modes. For hydrophilic substrates ($\theta_0 < 90°$) such as the one considered here, a sessile droplet normally evaporates with its contact line initially pinned. After some period of time, the droplet dries out with a receding contact-line. The contact angle may remain constant or not and the movement of the contact line can be smooth or go through abrupt jumps. This evaporation mechanism is often called stick-slip (SS) mode.

A behaviour consistent with these previous works is observed in our experiments. Two stages can be clearly identified during the evaporation process of water drops on copper. This is depicted with several snapshots in FIG. 5.2. All droplets stay initially pinned for most of their lifetime. During this first stage, the evaporation mechanism essentially corresponds to the pure CR mode previously mentioned. Both CCD and IR recordings show that the contact line remains perfectly circular in its original position while $\hat{H}$ and θ progressively decrease. This first stage is followed by a second phase wherein the droplet evaporates according to the SS mode. Once the the contact angle reaches certain critical value $\theta = \theta_c$, the droplet experiences a very sudden readjustment process to regain equilibrium in which its contact surface undergoes a significant reduction, see FIG. 5.2c and d. Normally, a segment of the triple line depins (bottom-right section in FIG. 5.2d) while the rest remains anchored to its original location (top-left section in FIG. 5.2d).

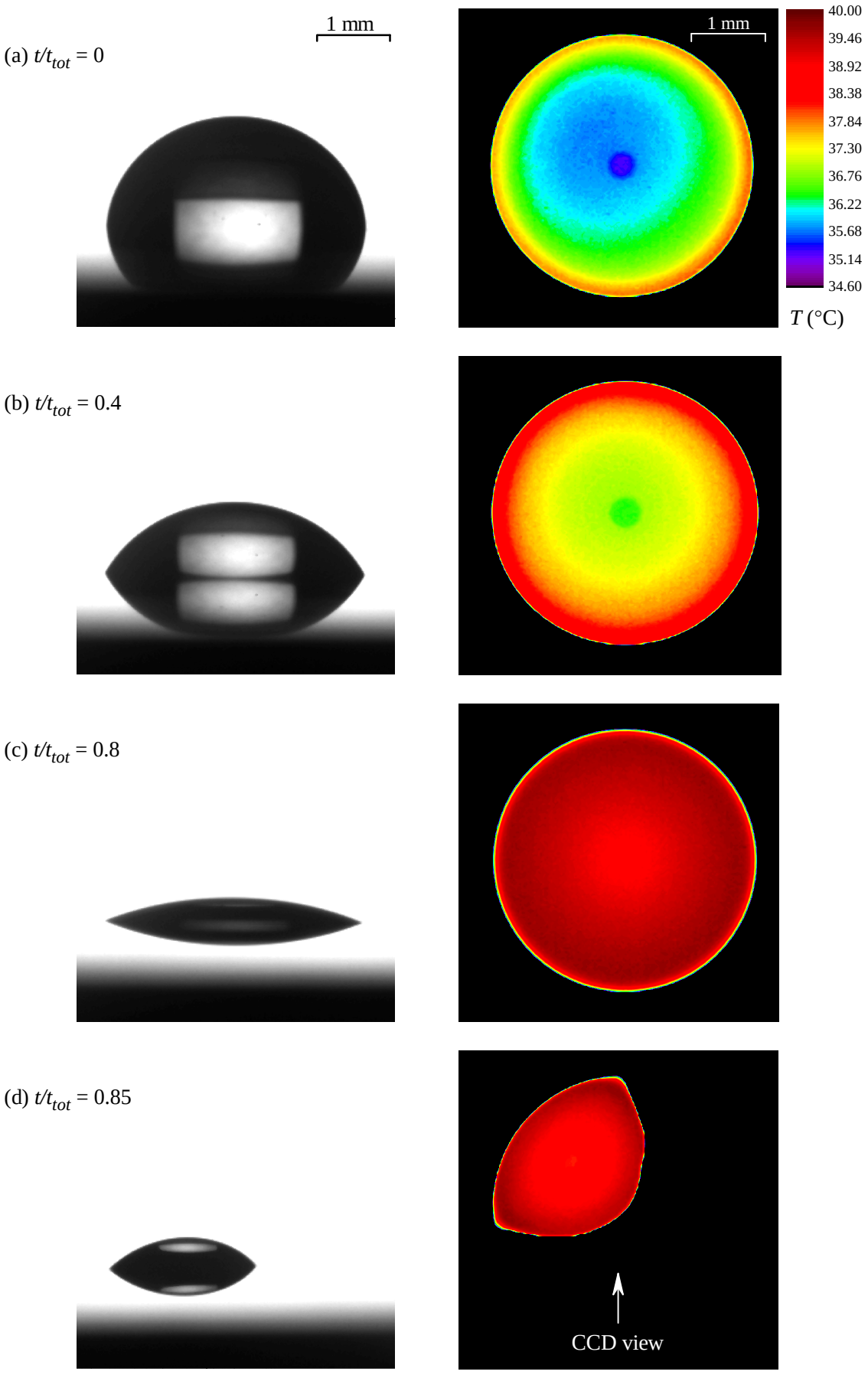

Figure 5.2: Evaporation of a water droplet into N_2 with $\hat{T}_w = 40\,°C$ and $\Delta\hat{T} = 14.5\,°C$ simultaneously recorded with a CCD camera from the side view (left column) and with a IR camera from the top (right column). The typical evaporation time is $\hat{t}_{tot} = 835\,s$.

This stick-slip process usually repeats itself several times before the droplet dries out. Once the depinning of the contact line takes place for the first time, interface sphericity is not guaranteed. The fact that there is a fraction of the contact-line at its original position resisting to form a new perfectly circular contact line (see FIG. 5.2d) reinforces the idea that this phenomenon is closely linked to the solid surface properties (mainly roughness).

The IR recordings reveal that the interface temperature follows a concentric distribution, from $\hat{T}_w$ near the contact line to a colder value at the apex. The dot observed at the centre of the interface is the reflection of the IR camera. No thermal motion in either the azimuthal or the radial direction is observed. This is in agreement with the work by Sefiane *et al.* [66] who discovered significant interface temperature fluctuations in drops of ethanol, methanol and FC-72 but not for water. The difference between the interface and substrate temperature is maximum at the start of the experiment, FIG. 5.2a. As the drop evaporates and $\hat{H}$ decreases, the radial temperature imbalance becomes less pronounced until the interface temperature eventually increases to be $\hat{T}_w$, FIG. 5.2b and c. This suggests that the Marangoni flow within the drop weakens as the drop becomes thinner, given that the radial temperature gradient is the driving force. An analogous behaviour is found for higher levels of heat, e.g. see FIG. 5.3 for $\hat{T}_w = 70\,^{\circ}\mathrm{C}$. The readings of the secondary thermocouple located above the drop indicate that the real temperature of the ambient gas, $\hat{T}_a$, is not constant as it is often assumed, see FIG. 5.4. $\hat{T}_a$ rises with $\hat{T}_w$ which means that the effective temperature difference in the vertical direction, $\Delta\hat{T} = \hat{T}_w - \hat{T}_a$, is in general smaller than when this is evaluated with a fixed room temperature. These readings are later used in the accompanying simulations to impose a more realistic vertical thermal gradient in the drop surroundings. In the simulations the value of $\hat{T}_w$ measured in the lab is imposed as the temperature of the lower boundary, which is modelled as a heated wall, while $\hat{T}_a$ is used in the vertical and upper boundaries to recreate the ambient gas.

5.2.2 Instantaneous drop characteristics

The evolution in time of the contact angle θ, height $\hat{H}$, base radius $\hat{R}$ and volume $\hat{V}$ over the range of $\hat{T}_w$ is illustrated in FIG. 5.5. As expected, FIG. 5.5 shows that $\hat{T}_w$ has an

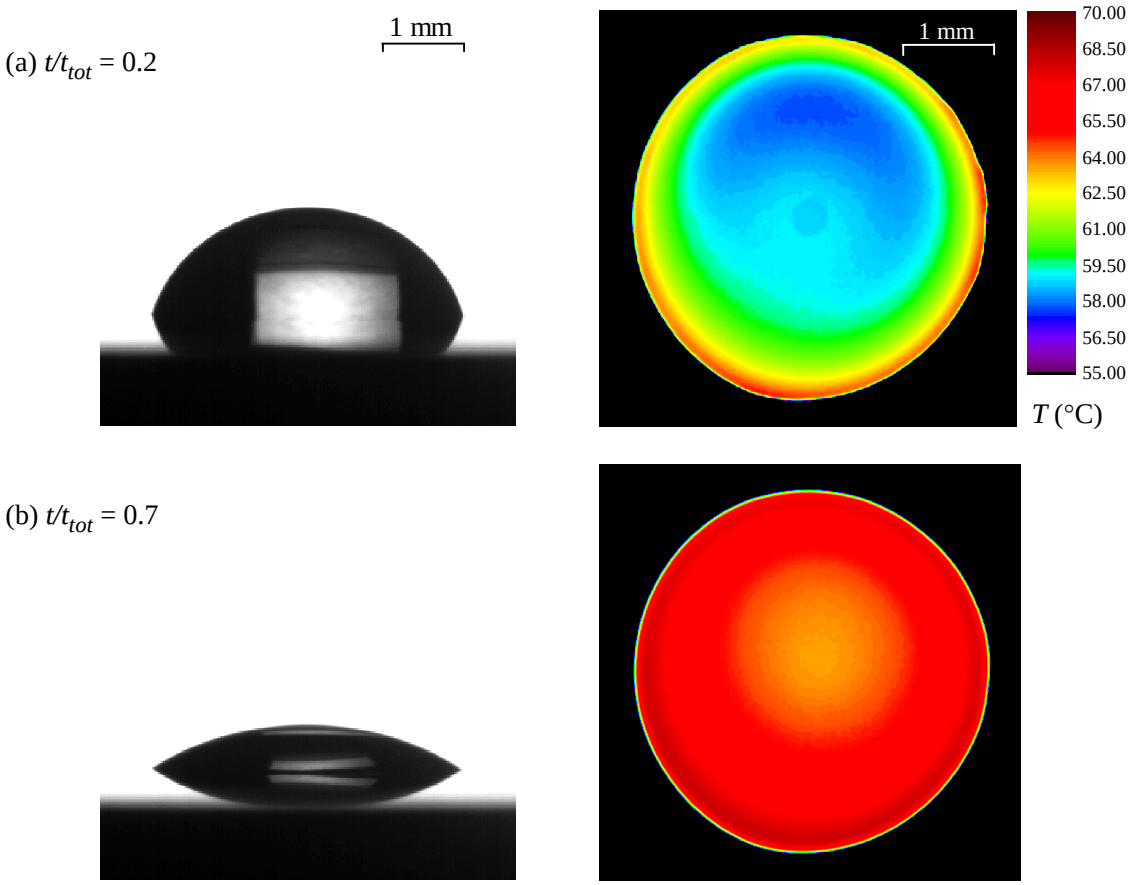

Figure 5.3: Evaporation of a water droplet into N_2 with $\hat{T}_w = 70\,°C$ and $\Delta\hat{T} = 39.8\,°C$ simultaneously recorded with a CCD camera from the side view (left column) and with a IR camera from the top (right column). The typical evaporation time is $\hat{t}_{tot} = 180\,s$.

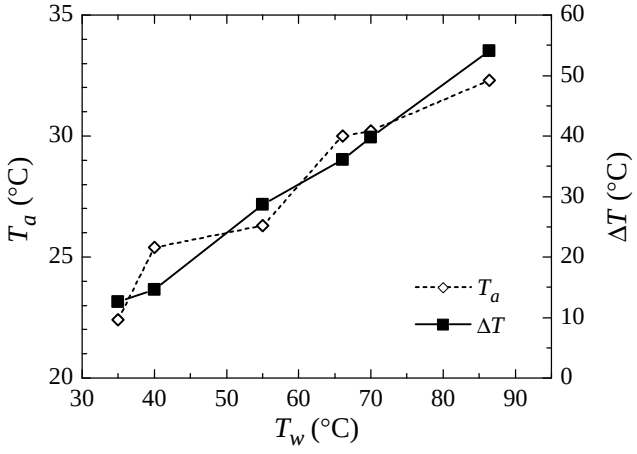

Figure 5.4: Ambient temperature $\hat{T}_a$ and effective temperature difference $\Delta\hat{T}$ at various levels of heat, $\hat{T}_w$.

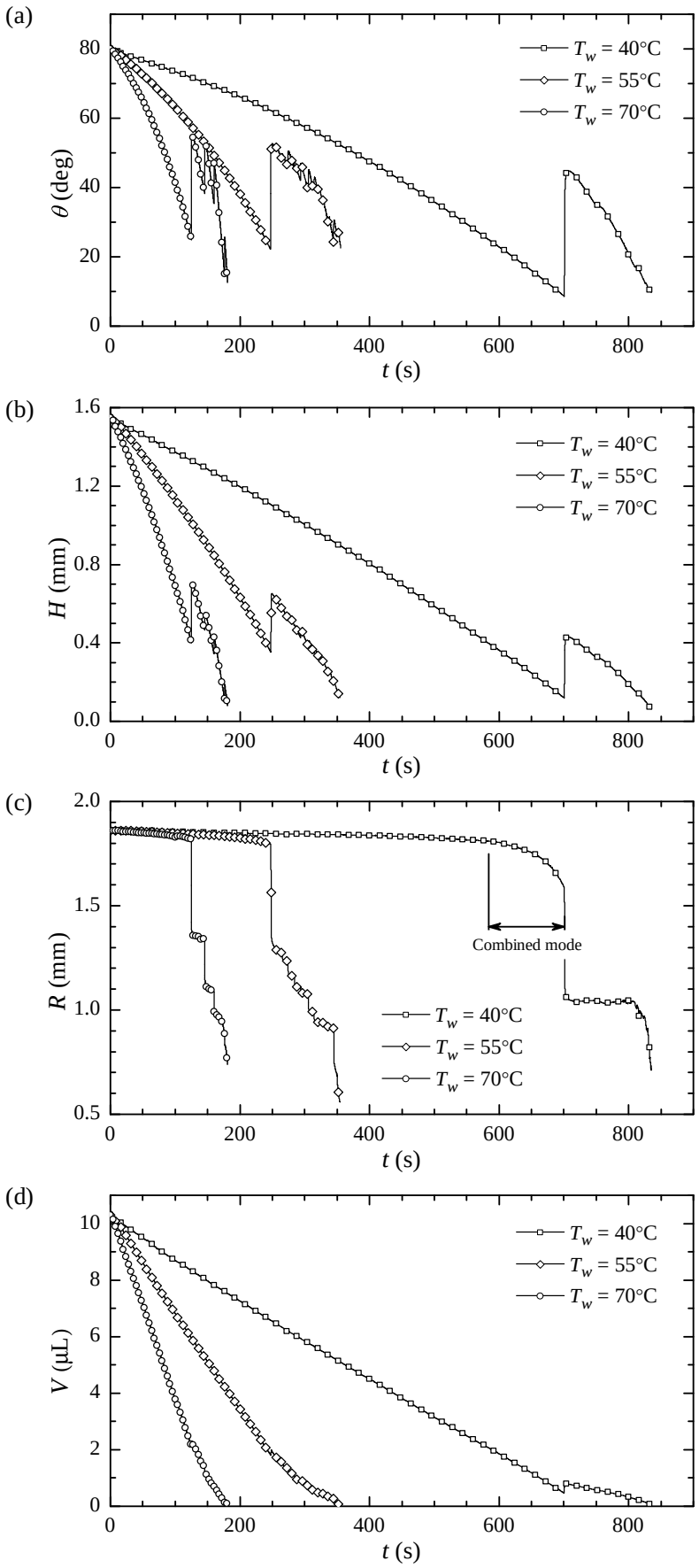

Figure 5.5: Typical evolution of the (a) contact angle θ, (b) maximum height $\hat{H}$, (c) contact radius $\hat{R}$ and (d) volume $\hat{V}$ for a water droplet evaporating into N_2 placed on a heated substrate at various temperatures $\hat{T}_w$. Results normalized according to the average initial drop characteristics: $\hat{H}_0 = 1.55\,\text{mm}$, $\hat{R}_0 = 1.86\,\text{mm}$, $\theta_0 = 80°$ $\hat{V}_0 = 10.4\,\mu\text{L}$.

adverse effect on the lifetime of the drops. The evaporation time until complete dry-out decreases with increasing $\hat{T}_w$. This is $\hat{t}_{tot} = 835$, 354 and 180 s for $\hat{T}_w = 40$, 55 and 70 °C, respectively, with standard deviation $< 7\%$ in all cases. The equilibrium contact angle $\theta_0 = 79° \pm 1°$ seems weakly affected by $\hat{T}_w$ finding slightly larger degrees of hydrophobicity with colder substrates. This tendency is in agreement with Young's equation, $\hat{\sigma}_{\mathrm{LG}} \cos\theta_0 = \hat{\sigma}_{\mathrm{SG}} - \hat{\sigma}_{\mathrm{SL}}$, given that $\hat{\sigma}_{\mathrm{LG}}$ decreases with temperature and, therefore, a smaller θ_0 is necessary to balance $\hat{\sigma}_{\mathrm{SG}} - \hat{\sigma}_{\mathrm{SL}}$ (assuming that these forces are not altered by $\hat{T}_w$). A similar but significantly more pronounced variation in θ_0 due to $\hat{T}_w$ was observed by Mollaret *et al.* [89] with water on aluminium. FIG. 5.5a shows that θ continuously decreases at a progressively-increasing rate until the three-dimensional motion of the droplet begins to recover equilibrium at a new position. Simultaneously, $\hat{H}$ registers an equivalent type of nonlinear evolution, FIG. 5.5b. Each depinning event is characterised by a sudden reduction of $\hat{R}$ accompanied by simultaneous increase of $\hat{H}$ and θ, which is in agreement with previous works available in the literature, e.g. Crafton & Black [88] or Orejón *et al.* [100]. FIG. 5.5c reveals that the boundary between the two main stages mentioned above (CR-SS modes) becomes less distinct as $\hat{T}_w$ decreases. For $\hat{T}_w = 70$ °C, the first jump occurs at $\hat{t} = 125$ s (70% of the drop lifetime) when the maximum deviation, $(\hat{R}_0 - \hat{R})/\hat{R}_0$, is 2.3%. For $\hat{T}_w = 55$ °C, the first jump happens at $\hat{t} = 354$ s (70%) with a deviation equal to 3.6%. When the substrate is colder, $\hat{T}_w = 40$ °C, the deviation after the same fraction of time is 2.7%, $\hat{t} = 584$ s, but this rapidly becomes much larger, $\sim 15\%$, when the drop depins at $\hat{t} = 701$ s (84%). In this last case, just before the first contact-line jump, the drop goes through a transition stage wherein the evaporation mechanism is actually a combined mode. FIG. 5.5a and c show that both θ and $\hat{R}$ decrease simultaneously suggesting that this stage fits neither the CR nor the CA pure modes of evaporation. Thus, the transition from CR to SS mode is not instantaneous as for $\hat{T}_w = 55$ or 70 °C. This behaviour is identically observed in all five runs.

Our experiments show that the critical contact angle θ_c, at which the first drop jump takes place, is dependent on $\hat{T}_w$, see FIG. 5.6a. With a warmer substrate, it is observed that $\theta_c = 26° \pm 3°$ and $22° \pm 3°$ for $\hat{T}_w = 55$ and 70 °C, respectively. This compares well with the $20 - 40°$ range reported by Crafton & Black [88] for $\hat{T}_w = 60 - 95$ °C. A

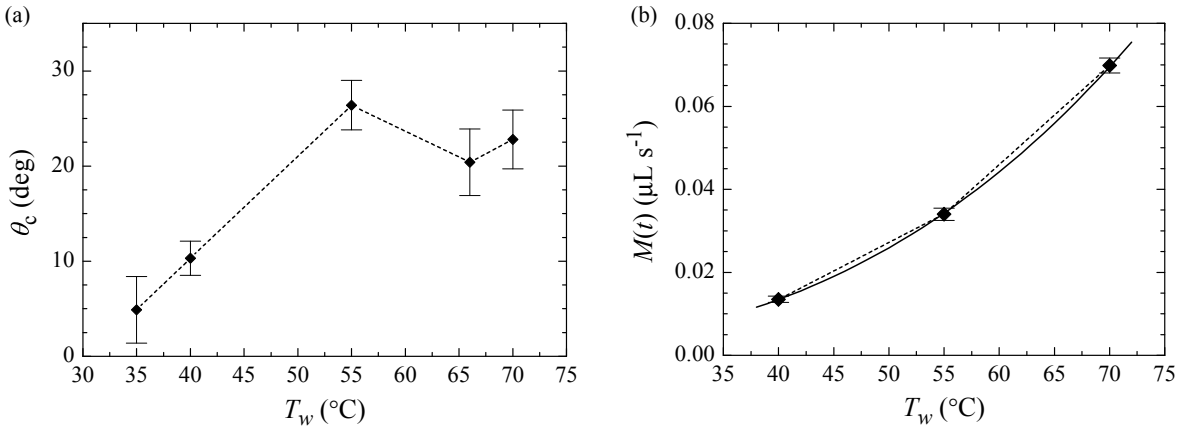

Figure 5.6: (a) Critical contact angle θ_c and (b) Evaporation rate $\hat{M}(\hat{t})$ of water droplets evaporating into N_2 at various levels of heat $\hat{T}_w$.

perceptible decrease of θ_c occurs when the substrate temperature is lower, i.e. $\theta_c = 10° \pm 2°$ with $\hat{T}_w = 40\,°\mathrm{C}$. Unlike for $\hat{T}_w = 55$ or $70\,°\mathrm{C}$, it is important to note that in this last case the contact line actually begins to recede before the first jump, to be more precise when $\theta \sim 25°$. The reasons for this were explained in the previous paragraph. The fact that, independently of $\hat{T}_w$, the actual depinning of the drops occurs in all cases when the contact angle reaches the same range $\theta = 22 - 26°$, i.e. at the same level of disequilibrium, suggests that the potential energy barrier postulated by Shanahan [101] is unaffected by temperature. However, our experiments reveal that the temperature does play an important role in determining the manner in which the three-dimensional motion of the contact line recovers equilibrium. This changes from instantaneous jumps at high temperatures to a progressive reduction (slip) of the base radius eventually followed by jumps in colder situations.

5.2.3 Evaporation rate

The instantaneous drop volume is illustrated in FIG. 5.5d. The evolution of $\hat{V}$ while the drop is pinned is found to be essentially linear for all values of $\hat{T}_w$. Hence, the resulting evaporation rate, $\hat{M}(\hat{t}) = -\mathrm{d}\hat{V}/\mathrm{d}\hat{t}$, is constant in the CR mode which is in agreement with previous works, e.g. [79, 89, 74, 95]. During this phase, our experiments show that $\hat{M}(\hat{t}) = 0.0135$, 0.0340 and $0.0698\,\mu\mathrm{L\,s^{-1}}$ for $\hat{T}_w = 40$, 55 and $70\,°\mathrm{C}$, respectively. The graphical representation of $\hat{M}(\hat{t})$, see FIG. 5.6b, reveals a nonlinear dependence between the substrate temperature and the measured evaporation rate. This is reasonable

given that the saturation pressure increases exponentially with the temperature (Antoine equation). Deviations from the linear behaviour of $\hat{M}(\hat{t})$ are noticed with $\hat{T}_w = 40\,^{\circ}\mathrm{C}$ when the drop is subjected to the combined evaporation mode right before the first jump, FIG. 5.5. The evaporation rate for this period is approximately 7% smaller than the initial one. Once the drop starts to experience the SS mode, the evolution of $\hat{V}$ becomes complex due to the multiple contact-line readjustments. In all cases, $\hat{M}(\hat{t})$ is smaller than that prior to the drop depinning. There is therefore agreement with the work by Picknett & Bexon [78] wherein the independent analysis of the two pure evaporation mechanisms revealed the CR mode as the one with highest evaporation rate. More recently, there have been other attempts to predict the lifetime of more realistic drops using a combined pinned-receding analysis, see Nguyen & Nguyen [96] and Stauber *et at.* [97], but the results are qualitatively the same for the most part.

5.3 Conclusions

The evaporation of small water droplets on a copper substrate at different temperatures has been examined experimentally. An experimental apparatus has been designed to simultaneously record the phase change process with an IR camera (top) and a CCD camera (side). The former allowed recording the interface temperature distribution along with the motion of the contact line. The latter allowed calculating the instantaneous contact angle, height, base radius and volume, see FIG. 5.5. The drops are placed within a closed chamber to generate a controlled nitrogen environment.

The results highlight the complexity of this physical process. With strong levels of heat, the drops normally evaporate following two distinct stages: an initial phase wherein the contact line is pinned is followed by a second period in which the drops experience a stick-slip behaviour characterised by abrupt jumps. In contrast, for lower substrate temperatures, an additional stage is observed in which the drops evaporate following a combined mode where both the contact angle and the base radius simultaneously decrease. For all levels of heat, the drop depinning occurs when the deviation from equilibrium is essentially the same, $\theta = 22 - 26^{\circ}$, which suggest an intrinsic energy barrier unaffected

by temperature. However, this work presents experimental evidence for the dependence of the contact line returning to equilibrium state on temperature.

In all cases, the drops remain pinned for at least 70% of their lifetime. During this time, the evolution of the drop volume decreases linearly, which is in agreement with previous works available in the literature. The measured evaporation rates are found to increase with temperature in a nonlinear fashion, see FIG. 5.6b. The thermography recordings show a concentric temperature distribution along the interface with the warmer region near the contact line. The difference between the substrate temperature and that of the apex decreases with decreasing drop height. No thermal fluctuations that could be indicative of unstable regimes are observed.

Chapter 6

Numerical Investigation of Evaporating Drops

The fully coupled two-phase dynamics of a evaporating sessile drops on a heated substrate are numerically investigated in this chapter. The simulations are designed to mimic the experimental conditions described in Chapter 5. As it has been previously mentioned, the sessile drop problem presents a number of additional challenges compared to the liquid layer system considered in Chapters 3 and 4, mainly due to the complicated contact-line dynamics and irregular geometry. Accounting for the associated phenomena requires the development of a more powerful model than that employed in the planar case (based on the VOF method). The diffuse-interface (DI) methodology is adopted to that end given that its versatility allows addressing not only pinned drops but also moving contact line (MCL) configurations. Following the philosophy of this investigation, traditional simplifications from "one-sided" or "1.5-sided" approaches (partial/complete neglect of the gas or simplified modelling via the Laplace approximation) are avoided by implementing transient advection-diffusion equations in both phases, therefore solving the interface momentum, energy and mass balances with more realistic local conditions.

Firstly, the instantaneous drying process of pinned drops is compared with the experimental data whilst new insights into the initial transient stage are provided. The investigation continues by examining the more complex case of sessile drops undergoing phase chance according to the constant-angle mode and, therefore, with contact line mo-

tion. The rest of the chapter is devoted to the study of three-dimensional phenomena occurring in drops with irregular contact area. The numerical results reveal the complexity of these situations wherein the drop geometry and, therefore, the local wettability and bulk dynamics are drastically affected by a complex surface-tension equilibrium on pursuit of the interface-area minimization.

6.1 Mathematical Formulation

6.1.1 Problem statement

A sketch of the problem is provided in FIG. 6.1. A sessile droplet of initial height $\hat{H}_0$ and contact radius $\hat{R}_0$ resting on heated substrate evaporates into a non-saturated surrounding gas at atmospheric pressure. The liquid is a pure substance while the gas is modelled as a mixture of two component, inert gas and vapour, of variable composition. All three pure substances are regarded as Newtonian fluids with invariable density under the present conditions. The density, dynamic viscosity, thermal conductivity and specific heat capacity for the liquid are denoted by $\hat{\rho}_l$, $\hat{\mu}_l$, $\hat{k}_l$, and $\hat{c}_{pl}$. The equivalent physical properties for the inert gas (referred to with subscript 1) and vapour (referred to with subscript 2) are represented by $\hat{\rho}_{g1}$, $\hat{\mu}_{g1}$, $\hat{k}_{g1}$, $\hat{c}_{pg1}$, and $\hat{\rho}_{g2}$, $\hat{\mu}_{g2}$, $\hat{k}_{g2}$, $\hat{c}_{pg2}$, respectively. Their coefficient of binary molecular diffusion is $\hat{D}$. The gas-mixture properties, denoted by $\hat{\rho}_g$, $\hat{\mu}_g$, $\hat{k}_g$ and $\hat{c}_{pg}$, depend on the relative amount of each component. These evolve with time due to transport phenomena in the gas and evaporation. The latent heat associated with the latter is $\Delta\hat{h}_v$. The liquid-gas interface is characterised by a surface tension, $\hat{\sigma}$, which decreases monotonically with temperature, $\hat{T}$, i.e. $\hat{\sigma} = \hat{\sigma}_0 - \hat{\gamma}\left(\hat{T} - \hat{T}_a\right)$, where $\hat{\sigma}_0$ is the surface tension at the reference temperature $\hat{T}_a$ and $\hat{\gamma} = -\partial\hat{\sigma}/\partial\hat{T}$ denotes its temperature-dependence coefficient. The substrate is considered to remain isothermal at temperature $\hat{T}_w$ while the gas far from the drop is at temperature $\hat{T}_a$.

The following changes of variables are introduced to non-dimensionalise this problem

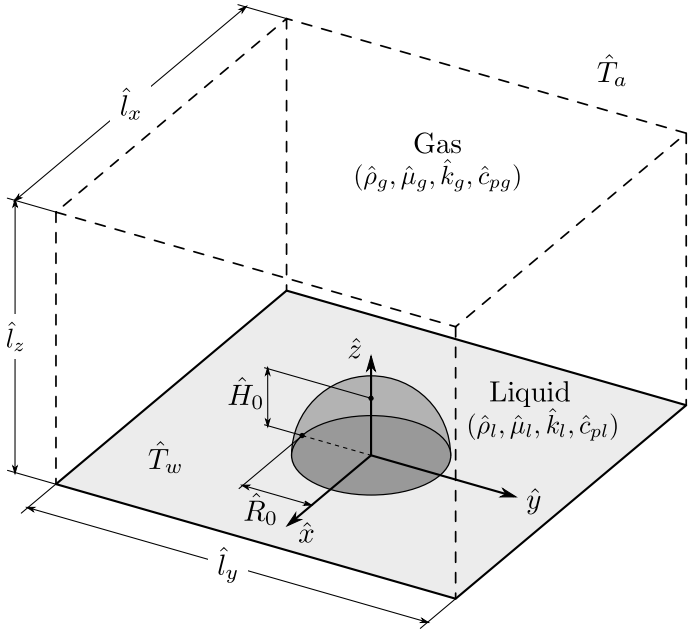

Figure 6.1: Schematic of the droplet model.

(the caret decoration denotes dimensional variables),

$$\begin{aligned} &\hat{\mathbf{x}} = \hat{H}_0\,\mathbf{x}, && \hat{\mathbf{u}} = \hat{U}_0\,\mathbf{u}, && \hat{p} = \hat{\rho}_l \hat{U}_0^2\,p, \\ &\hat{T} = T\,\Delta\hat{T} + \hat{T}_a, && \hat{t} = \frac{\hat{H}_0}{\hat{U}_0}\,t, && \hat{\sigma} = \hat{\sigma}_0 \sigma. \end{aligned} \tag{6.1}$$

Here, $\mathbf{x} = (x,\, y,\, z)$ and $\mathbf{u} = (u,\, v,\, w)$ are the coordinate and velocity vectors referred to Cartesian system of coordinates located at the centre of the drop, $\hat{U}_0 = \hat{\gamma}\Delta\hat{T}/\hat{\mu}_l$ represents the characteristic thermocapillary velocity with $\Delta\hat{T} = \hat{T}_w - \hat{T}_a$, p is the pressure, and t denotes the time. The physical properties of the inert gas and vapour are taken into consideration via the following ratios,

$$\begin{aligned} &\Gamma_\rho = \frac{\hat{\rho}_l}{\hat{\rho}_{g1}}, && \Gamma_\mu = \frac{\hat{\mu}_l}{\hat{\mu}_{l1}}, && \Gamma_k = \frac{\hat{k}_l}{\hat{k}_{l1}}, && \Gamma_{cp} = \frac{\hat{c}_{pl}}{\hat{c}_{pg1}}, \\ &\Omega_\rho = \frac{\hat{\rho}_l}{\hat{\rho}_{g2}}, && \Omega_\mu = \frac{\hat{\mu}_l}{\hat{\mu}_{l2}}, && \Omega_k = \frac{\hat{k}_l}{\hat{k}_{l2}}, && \Omega_{cp} = \frac{\hat{c}_{pl}}{\hat{c}_{pg2}}. \end{aligned} \tag{6.2}$$

The initial drop geometry (H_0, R_0) and the dimensions of the computational domain (L_x, L_y, L_z) become,

$$H_0 = 1, \qquad R_0 = \frac{\hat{R}_0}{\hat{H}_0}, \qquad L_x = \frac{\hat{l}_x}{\hat{H}_0}, \qquad L_y = \frac{\hat{l}_y}{\hat{H}_0}, \qquad L_z = \frac{\hat{l}_z}{\hat{H}_0}, \tag{6.3}$$

where $\hat{l}_x$, $\hat{l}_y$ and $\hat{l}_z$ are the width, depth and height of the computational region.

6.1.2 Governing equations

The fully-coupled two-phase dynamics of the drop and surrounding gas are modelled via a DI method. See Anderson *et al.* [128] for a review of DI methods. The mathematically sharp interface is, therefore, replaced with an interface of finite thickness which can be artificially prescribed [129]. On the other hand, the free evaporation of water drops at atmospheric pressure is a relatively slow phase change process. As it has been shown in numerous theoretical and experimental works available in the literature [78, 20, 18, 74], this characteristic results in that the gas right at the interface is (quasi) saturated with vapour. Hence, the problem of how to model the interface mass transfer rate is analogous to that discussed in section §4.1.1 for the evaporating liquid layer. The local evaporation rate S is, therefore, calculated with the same expression, i.e.,

$$S = \frac{(1-c)\,\rho_g}{t_s}\left(\frac{p_s}{p_s + \frac{1}{\mathscr{M}}\left(\frac{1}{\mathscr{P}} - p_s\right)} - \omega\right), \tag{6.4}$$

where ω is the vapour mass fraction, p_s denotes the saturation pressure and $\mathscr{M} = \hat{M}_{g2}/\hat{M}_{g1}$ is the vapour/inert-gas molar weight ratio. It should be noted that the new characteristic pressure selected for the drop, see (6.1), results in a different definition of the group $\mathscr{P} = \hat{\rho}_l \hat{U}_0^2/\hat{p}_r$, with $\hat{p}_r$ denoting the absolute pressure. The sign criterion is maintained, $S > 0$ for evaporation while $S < 0$ for condensation, as well as the form of the Antoine expression used to approximate the temperature dependence of the saturation pressure, i.e. $\log_{10}(\hat{p}_s) = \hat{A} - \hat{B}/(\hat{C} + \hat{T})$. Here, t_s symbolises the timestep size, which should be small enough to maintain saturation condition at the interface. This is selected in the same manner as for the evaporating liquid layer, chapter 4, with equation (4.12).

The DI method used is based on that developed by Ding *et al.* [130] (following Jacqmin [129] and Badalassi *et al.* [131]) for pure hydrodynamic problems, but with a number of extensions to address non-isothermal conditions and phase change. The main difference between VOF and DI models lies in that the colour function in the latter includes an additional diffuse term, which maintains a smooth evolution of c across the interface and

allows addressing contact-line dynamics. DI methods are grounded in two fundamental principles. The first one, by van der Waals [132] who theorised that, if the interface between two fluids is regarded as a narrow layer of finite thickness, the volumetric free energy density $\hat{f}$ across this is dependent on the local composition, represented by an order parameter denoted by c here, and on the local composition gradients, i.e.

$$\hat{f} = \hat{\varepsilon}^{-1}\hat{\sigma}_0\alpha\Psi(c) + \frac{1}{2}\hat{\varepsilon}\hat{\sigma}_0\alpha\left|\hat{\nabla}c\right|^2 \tag{6.5}$$

where $\hat{\varepsilon}$ is a measure of the interface thickness, $\Psi(c)$ is the bulk energy density with minimum levels corresponding to the fluids' two stable phases, and α is a dimensionless adjustment parameter. In addition, van der Waals [132] hypothesised that equilibrium interface profiles are those that minimise the total free energy $\hat{\mathscr{F}} = \int_\Omega \hat{f}\,\mathrm{d}\hat{V}$, where Ω represents the interfacial domain. From the calculus of variations [129], these profiles must satisfy,

$$\hat{\phi} = \hat{\varepsilon}^{-1}\hat{\sigma}_0\alpha\Psi'(c) + \hat{\varepsilon}\hat{\sigma}_0\alpha\hat{\nabla}^2 c = \text{constant}, \tag{6.6}$$

where $\hat{\phi} = \partial\hat{\mathscr{F}}/\partial c$ is the chemical potential. The second key element of DI methods was given by Cahn & Hilliard [133, 134] and Cahn [135] who extended the van der Walls' hypothesis to time-dependent situations postulating that irregular interface profiles recover equilibrium by virtue of diffusion fluxes which are proportional to chemical potential gradients. On these premises and selecting the liquid volume fraction as order parameter ($c = 1$ in the liquid, $c = 0$ in the gas and $0 < c < 1$ in the interface region), it can be shown that the spatio-temporal evolution of c is ruled by the phase-field advection-diffusion Cahn-Hilliard equation [130], i.e.,

$$\frac{\partial c}{\partial t} + \nabla\cdot(c\mathbf{u}) - \frac{1}{Pe}\nabla\cdot(M\nabla\phi) = 0, \tag{6.7}$$

where $Pe = \hat{U}_0\hat{H}_0/(\hat{M}_0\hat{\phi}_0)$ is the Péclet number, $M = c\,(1-c)$ is a diffusive coefficient referred to as mobility and whose characteristic value is denoted by $\hat{M}_0$, $\phi = \varepsilon^{-1}\left[\Psi'(c) - \varepsilon^2\nabla^2 c\right]$ is the chemical potential referred to the scale $\hat{\phi}_0$, $\Psi(c) = \frac{1}{4}c^2\,(1-c)^2$, and ε is a measure of the interface thickness, scaled by $\hat{H}_0$, which allows controlling its

thickness. With the appropriate boundary conditions, equation (6.7) conforms a mass-conservative interface capturing method in which the interface profile is maintained regular by means of the diffusive term. Some recent examples wherein this equation has been used comprise droplet spreading [136] and droplet motion under shear flow [137, 138] or two-layer flows [139].

For an evaporating drop, the mass is globally conserved but not the mass of liquid. This decreases in time due to the liquid-to-gas phase change which takes place at the interface. Thus, accounting for interface mass transfer requires adding a interface sink/source term in (6.7), which leads to the phase-change version of the Cahn-Hilliard equation, i.e.,

$$\frac{\partial c}{\partial t} + \nabla \cdot (c\mathbf{u}) - \frac{1}{Pe}\nabla \cdot (M\nabla\phi) = -S, \tag{6.8}$$

where S is only computed in the interface region. Following the accuracy/performance study conducted by Ding *et al.* [130], the Péclet number is set to $Pe = 1/\varepsilon^2$, choosing ε to be proportional to the grid resolution, i.e. $\varepsilon = 0.5\min(\Delta x, \Delta y, \Delta z)$. This configuration leads to an interface thickness, i.e. distance between contours of $c = 0.1$ and 0.9, of around three times the minimum grid spacing.

The overall mass balance is completed with the continuity equation while the conservation of momentum (neglecting gravity) is governed by the Navier-Stokes equations, i.e.,

$$\nabla \cdot \mathbf{u} = -S\left(1 - \Omega_\rho\right), \tag{6.9}$$

$$\frac{\partial (\rho\mathbf{u})}{\partial t} + \nabla \cdot (\rho\mathbf{u}\mathbf{u}) = -\nabla p + \frac{1}{Re}\nabla \cdot \left[\mu\left(\nabla\mathbf{u} + \nabla\mathbf{u}^T\right)\right] + \frac{1}{We}\phi\nabla c - \frac{1}{Re}\left(\nabla_s T\right)\delta, \tag{6.10}$$

where $\rho = c + \rho_g(1-c)$ and $\mu = c + \mu_g(1-c)$ are the one-fluid form of the density and viscosity, respectively. $Re = \hat{\rho}_l\hat{U}_0\hat{H}_0/\hat{\mu}_l$ is the Reynolds number, $We = \hat{\rho}_l\hat{U}_0^2\hat{H}_0/\left(6\sqrt{2}\hat{\sigma}_0\right)$ denotes the Weber number, $\phi\nabla c$ is the DI interpretation of the mean surface tension stress enforcing [129, 130], and $(\nabla_s T)\,\delta$ models the thermocapillarity effect with $\nabla_s = \nabla - \mathbf{n}(\mathbf{n}\cdot\nabla)$ being the gradient tangent to the interface, $\mathbf{n} = \nabla c/|\nabla c|$ the inwards unit vector normal to the interface, and $\delta = |\nabla c|$. It should be noted that several authors, e.g. Jacqmin [140], Ding & Spelt [136] and Yue *et al.* [141], have already shown that

the results from this DI approach converge to the sharp-interface limit as the interfacial thickness is reduced.

The conservation of energy in both phases is computed via

$$\frac{\partial\left(\rho c_p T\right)}{\partial t}+\nabla\cdot\left(\rho c_p T\mathbf{u}\right)=\frac{1}{RePr}\nabla\cdot\left(k\nabla T\right)-\frac{1}{Ja}S. \tag{6.11}$$

Here, $k=c+k_g\left(1-c\right)$ and $c_p=\left(c+\rho_g c_{pg}(1-c)\right)/\left(c+\rho_g(1-c)\right)$ are the one-fluid form thermal conductivity and specific heat capacity, and $Pr=\hat{\mu}_l\hat{c}_{pl}/\hat{k}_l$ and $Ja=\hat{c}_{pl}\Delta\hat{T}/\Delta\hat{h}_v$ are the Prandtl and Jakob numbers, respectively. Finally, the vapour mass fraction, ω, is governed by a general advection-diffusion transport equation only solved in gas phase, i.e,

$$\frac{\partial\left[\rho_g\left(1-c\right)\omega\right]}{\partial t}+\nabla\cdot\left[\rho_g\left(1-c\right)\omega\mathbf{u}\right]=\frac{1}{ReSc}\nabla\cdot\left[\rho_g\left(1-c\right)\nabla\omega\right]+S, \tag{6.12}$$

where $Sc=\hat{\mu}_l/(\hat{\rho}_l\hat{D})$ is the Schmidt number. Note that equations (6.9), (6.11) and (6.12) are exactly the same to those implemented with the VOF method for the liquid layer problem, i.e. equations (4.16), (4.20) and (4.22), respectively. The mixture properties, ρ_g, μ_g, k_g and c_{pg}, are similarly approximated according to,

$$\begin{aligned}
\rho_g &= \left[\Gamma_g\left(1-\omega\right)+\Omega_g\omega\right]^{-1},\\
\mu_g &= \left(1-\omega\right)/\Gamma_\mu+\omega/\Omega_\mu,\\
k_g &= \left(1-\omega\right)/\Gamma_k+\omega/\Omega_k,\\
c_{pg} &= \left(1-\omega\right)/\Gamma_{cp}+\omega/\Omega_{cp}.
\end{aligned} \tag{6.13}$$

6.1.3 Boundary and initial conditions

The boundary conditions are selected to mimic the experiments presented in Chapter 5. The lower boundary ($z=0$) is modelled as an isothermally heated wall ($T=1$) with no-slip ($\mathbf{u}=0$) and nonpenetration of mass ($\mathbf{n}_z\cdot\nabla\omega=0$). Note that a relatively large block of copper was intentionally employed as heated substrate in the experiments to make appropriate this choice of conditions for the lower boundary. Here, $\mathbf{n}_x$, $\mathbf{n}_y$ and $\mathbf{n}_z$ denote the unit vectors in the principal directions. The Cahn-Hilliard equation requires an additional Neumann boundary condition ($\mathbf{n}_z\cdot\nabla\phi=0$) to guarantee the volume con-

servation of each fluid [142]. The temperature of the upper boundary ($z = L_z$) is set to the ambient temperature as recorded by the secondary thermocouple ($T = 0$) while first-gradient boundary conditions ($\mathbf{n}_x \cdot \nabla T = 0$ and $\mathbf{n}_y \cdot \nabla T = 0$) are used at the vertical walls of the computational domain ($x = \pm L_x/2$ and $y = \pm L_y/2$). In the experimental setup, the size of test chamber was intentionally designed to be very large in comparison to the drop so this would evaporate into a vast volume of pure N_2 (dry gas). An approximate infinite amount of N_2 surrounding the drop makes it is reasonable to assume that the phase change does not result in a noteworthy increment in the bulk humidity. Thus, the zero Dirichlet boundary condition is imposed in the vertical and top boundaries ($\omega = 0$ at $x = \pm L_x/2$, $y = \pm L_y/2$ and $z = L_z$). Provided that the computational domain is large enough, the vapour distribution around the drop becomes independent of the far-field boundary conditions. For the same reason, it is considered that the flow far away from the drop is at rest ($\mathbf{u} = 0$ at $x = \pm L_x/2$, $y = \pm L_y/2$ and $z = L_z$). To conclude with the boundary conditions, the fact that the species equation is only solved in the gas phase requires the implicit imposition of the nonpenetration condition ($\mathbf{n} \cdot \nabla \omega = 0$ and $\mathbf{n} \cdot \mathbf{u} = 0$) along the species-field boundary in the liquid-gas interface (contour $c = 0.9$). It is important to note that here the condition $\mathbf{n} \cdot \mathbf{u} = 0$ merely symbolises that the convective fluxes across the selected contour bounding the species field have been strictly set to zero in the numerical solution of the species equation to ensure vapour mass conservation.

This time-dependent problem is closed with the initial conditions. At $t = 0$, the drop is a spherical cap of height $H_0 = 1$ and base radius R_0, the two-phase flow is at rest ($\mathbf{u} = 0$) and the gas-mixture is completely dry ($\omega = 0$). From the experiments, it is known that the chamber was let to reach thermal equilibrium before the drop was deposited onto the substrate and that the liquid dosed through the pipette was pumped from a reservoir located outside the chamber and, therefore, at ambient temperature. These two considerations lead to select the initial drop temperature as $T = 0$ while the initial temperature of the gas a linear distribution from the substrate temperature to the ambient temperature, i.e. $T = (L_z - z)/L_z$. Both conditions are simultaneously met with $T = (1 - c)(L_z - z)/L_z$.

6.1.4 Numerical method

The governing equations (6.8)-(6.12), coupled with the volumetric interface mass-transfer rate calculated with (6.4), conform a system of seven PDEs with seven unknowns (c, p, u, v, w, T and ω). This is simultaneously solved with a finite-volume discretization of the physical domain by means of a staggered Marker-And-Cell (MAC) grid. The MAC grid works such that scalar variables (c, p, T, ω) are stored in the cell centres while the velocity components (u, v, w) are defined at the control-volume faces. Mesh refinement tests are carried out to ensure that the results are grid-independent. The Cahn-Hilliard equation is solved numerically using the implicit-explicit strategy proposed by Badalassi *et al.* [131] with a second order semi-backward difference formula (SBDF) scheme, see Ascher *et al.* [143]. The convective term is explicitly computed approximating the fluxes at cell faces with an upwind (referred to the flow direction) fifth-order weighed essentially non-oscillatory (WENO) scheme, see Liu *et al.* [144], to increase the code's stability to the shock-like nature of the c profile across the interface [130]. The resolution of the velocity and pressure fields is achieved by a standard projection method wherein the intermediate velocity (without considering p) is found with the second-order Crank-Nicolson Adams-Bashforth (CNAB) scheme to approximate the diffusive (implicitly) and advective (explicitly) terms, respectively. The pressure is then added to update the velocity to its final value ensuring that the continuity condition is obeyed. The energy and species fields are advanced in time with similar semi-implicit CNAB techniques. Spatial derivatives are approximated by the centred scheme. The solution strategy requires knowing the value of all the variables at the current timestep (n) as well as c at the previous timestep ($n-1$). The computation then proceeds as follows,

1. Update the volume fraction field c solving equation (6.8) with c, $\mathbf{u}$ and S at timestep n and c at timestep $n-1$.

2. Update the vapour mass-fraction field ω solving equation (6.12) with c, $\mathbf{u}$, S, ω at timestep n and c at timestep $n+1$.

3. Update the temperature field T solving equation (6.11) with c, $\mathbf{u}$, S, ω, T at timestep n and c and ω at timestep $n+1$.

4. Finally, with c, ω and T known at n and $n+1$, the velocity is updated solving (6.9) and (6.10) with the surface tension and physical properties evaluated at $n+1/2$ as recommended by Ding *et al.* [130].

I developed the analytical model presented in subsection 6.1.2 and the numerical algorithm discussed above. The analytical model required deriving a novel phase-change version of the Cahn-Hilliard equation, i.e. equation 6.8, and a new expression for the interface mass-transfer rate appropriate for the DI method, i.e. equation 6.4. The code development started with the version used by Valluri *et al.* [139] to investigate stratified flows. This archaic model only addressed hydrodynamic problems with two pure fluids. I wrote new subroutines to also address two-phase heat transfer, i.e. equation 6.11, the advection-diffusion transport of vapour in the gas phase, i.e. equation 6.12, and phase change, i.e. equation 6.4. This required significant changes also in the momentum and continuity equations given that all the equations are fully-coupled and due to the fact that one of the fluids became a gas mixture rather than a pure substance. The species equation presented the additional complexity of requiring an implicit imposition of the non-penetration boundary condition at the liquid-gas interface, whose location is part of the solution. The code also required important changes in the momentum and Cahn-Hilliard equations to model the Marangoni effect and moving contact-line dynamics; these phenomena had not been addressed in Valluri *et al.* [139]. The mathematical algorithm was implemented in 3D in Fortran with all the routines parallelised with OpenMP. The code was executed on the supercomputer ARCHER and the post-processing was performed with Matlab scripts written as necessary.

6.2 Results and Discussion

To illustrate the dynamics of the evaporating drop and the changes resulting from different levels of heat, two of the configurations experimentally studied are numerically investigated here, namely $\hat{T}_w = 40\,^{\circ}\mathrm{C}\,(\Delta\hat{T} = 14.5\,^{\circ}\mathrm{C})$ and $70\,^{\circ}\mathrm{C}\,(\Delta\hat{\mathrm{T}} = 39.8\,^{\circ}\mathrm{C})$. The initial height and base radius of the drop are $\hat{H}_0 = 1.55\,\mathrm{mm}$ ($H_0 = 1$) and $\hat{R}_0 = 1.86\,\mathrm{mm}$ ($R_0 = 1.2$), respectively. The physical properties of distilled water, vapour and nitrogen

		N_2	Water (Vapour)	Water (Liquid)
ρ	($kg\,m^{-3}$)	1.09	0.701	997
μ	($Pa\,s$)	1.80×10^{-5}	1.05×10^{-5}	6.46×10^{-4} $(3.97 \times 10^{-4})^*$
k	($W\,m^{-1}\,K^{-1}$)	2.67×10^{-2}	1.97×10^{-2}	0.623
c_p	($J\,kg^{-1}\,K^{-1}$)	1040	1869	4180
M	($g\,mol^{-1}$)	28.01	18.02	
σ	($N\,m^{-1}$)	7.27×10^{-2}		
γ	($N\,m^{-1}\,K^{-1}$)	1.71×10^{-4}		
Δh_v	($J\,kg^{-1}$)	2.39×10^{6}		
D	($m^2\,s^{-1}$)	2.84×10^{-5} $(3.47 \times 10^{-5})^*$		

Table 6.1: Physical properties of distilled water (liquid and vapour) and nitrogen gas at $\hat{T} = 40\,^{\circ}C$ and $\hat{p} = 1\,atm$. *Corrected values used for $\hat{T} = 70\,^{\circ}C$.

$\hat{A}$	$\hat{B}$	$\hat{C}$
8.0557	1723.6	233.08

Table 6.2: Empirical coefficient for the Antoine equation $\log_{10}(\hat{p}_s) = \hat{A} - \hat{B}/(\hat{C} + \hat{T})$ for distilled water with $\hat{p}_s$ in (Pa) and $\hat{T}$ in (°C).

	Pr	Re	We	Ja	Sc	$\mathscr{P}$	$\mathscr{M}$
$\hat{T}_w = 40\,^\circ\mathrm{C}$	4.3	9.18×10^3	37	0.025	0.023	0.145	0.643
$\hat{T}_w = 70\,^\circ\mathrm{C}$	2.7	6.67×10^4	736	0.070	0.011	2.892	0.643

	Γ_ρ	Γ_μ	Γ_k	Γ_{cp}	Ω_ρ	Ω_μ	Ω_k	Ω_{cp}
$\hat{T}_w = 40\,^\circ\mathrm{C}$	915	36	23	4.0	1422	62	32	2.2
$\hat{T}_w = 70\,^\circ\mathrm{C}$	915	22	23	4.0	1422	38	32	2.2

Table 6.3: Dimensionless parameters representing the experimental configurations with $\hat{T}_w = 40\,^\circ\mathrm{C}\,(\Delta\hat{T} = 14.5\,^\circ\mathrm{C})$ and $\hat{T}_w = 70\,^\circ\mathrm{C}\,(\Delta\hat{T} = 39.8\,^\circ\mathrm{C})$ evaluated with $\hat{H}_0 = 1.55\,\mathrm{mm}$ and with the physical properties listed in TABLE 6.1.

are listed in TABLE 6.1. All physical properties have been evaluated in the range of temperatures considered in the simulations concluding that, in general, the variations due to temperature are negligible for the liquid ($< 4\%$) and for the gases ($< 8\%$), with the exception of the liquid viscosity $\hat{\mu}_l$ ($\sim 40\%$ lower at $70\,^\circ\mathrm{C}$) and molecular diffusivity $\hat{D}$ ($\sim 25\%$ larger at $70\,^\circ\mathrm{C}$), see TABLE 6.1. The empirical coefficients for the saturation pressure are available in TABLE 6.2. The resulting dimensionless groups for the two cases under consideration are summarised in TABLE 6.3.

6.2.1 Model validation

The direct numerical simulations begin by considering first the case of an axisymmetric droplet evaporating with its contact line pinned (CR mode). Initially, the droplet undergoes a transient stage wherein the temperature is adjusted while the Marangoni effect generates convection currents in both the liquid and the gas phases. Eventually the drop reaches a quasi-steady state wherein the two-phase flow characteristics evolve more gradually with t in accordance to the evaporation timescale. The instantaneous evolution of θ, H, R and V obtained with the simulations, for both $\hat{T}_w = 40\,^\circ\mathrm{C}$ and $70\,^\circ\mathrm{C}$, is compared with the experimental data in FIG. 6.2. It is is important to note that these curves essentially overlap in dimensionless form (as opposed to FIG. 5.5) as a natural consequence of the dimensional analysis and not of a relative (artificial) normalization of the curves. In other words, there is no loss of information in going from FIG. 5.5 to FIG. 6.2. This does not mean that the dynamics of a evaporating drop become independent of $\hat{T}_w$ when the problem is studied in the dimensionless framework, nonetheless.

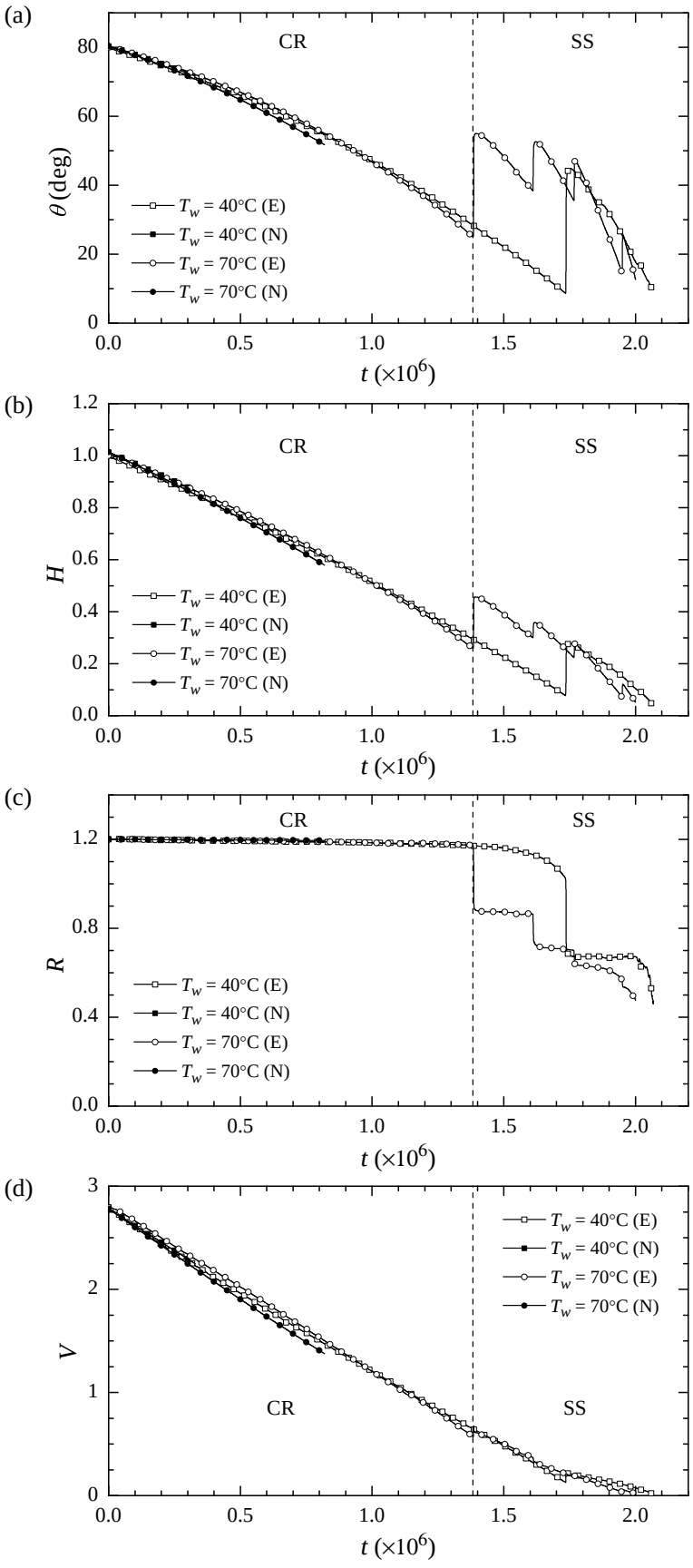

Figure 6.2: Comparisons between experimental (E) and numerical (N) data for the instantaneous (a) contact angle θ, (b) height H, (c) base radius R and (d) volume V, with different levels of substrate heat $\hat{T}_w$. The drop evaporates according to the CR mode during the initial 70% of the drop lifetime and in the SS mode for the remaining time. The governing parameters are listed in TABLE 6.3.

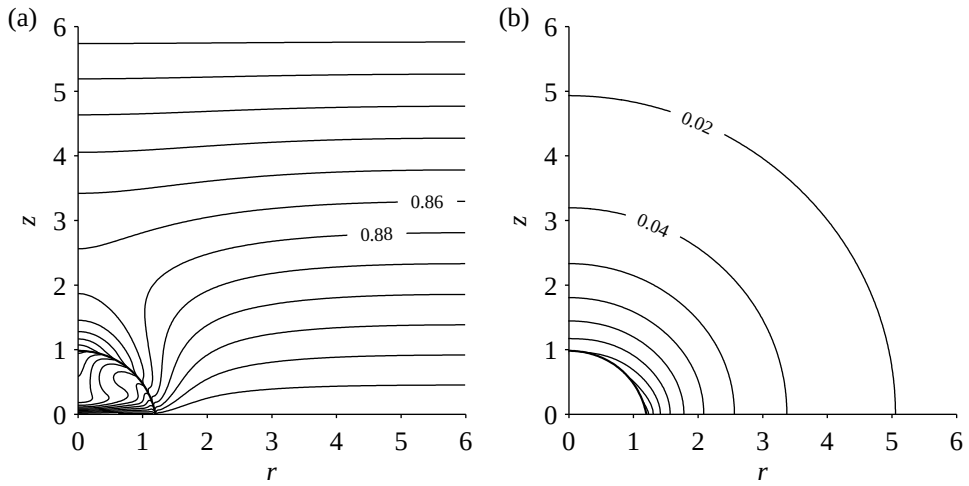

Figure 6.3: Quasi-steady state with $\hat{T}_w = 70\,^{\circ}\mathrm{C}$ and $H = 0.98$ ($t = 6.7 \times 10^4$). (a) Temperature, (b) Vapour mass fraction.

Excellent agreement between experiments and simulations is observed in the initial stages. The DI method maintains the contact line perfectly pinned in a very natural manner by virtue of the diffusive term in the Cahn-Hilliard equation. This allows the accurate mimicking of the pure CR evaporation mode (FIG. 6.2c), which corresponds to at least the initial 70% of the drop lifetime as showed by the experiments. The numerical evolution of V is essentially linear while θ and H decrease at a progressively increasing rate. The average dimensionless experimental evaporation rates are $M(t) = 1.46\times10^{-6}$ and 1.69×10^{-6} for $\hat{T}_w = 40\,^{\circ}\mathrm{C}$ and $70\,^{\circ}\mathrm{C}$, respectively. The simulations suggest dimensionless evaporation rates of $M(t) = 1.61 \times 10^{-6}$ and 1.72×10^{-6} for the same cases, FIG. 6.2c. The slightly larger evaporation rate predicted by the numerical simulations is associated to an insufficient size of the computational domain, restricted to $L_r = L_z = 5R_0$ for the results presented here. However, recent computations with much larger domains, $L_r = L_z = (20 - 100)R_0$, show more accurate results not only in the initial stages but also throughout the drop lifetime.

The initial quasi-steady (after the transient stage) temperature and vapour mass fraction are presented in FIG. 6.3. The evaporative cooling has an important thermal effect inside the drop as well as on the temperature of the surrounding gas outside the interface, FIG. 6.3a. The latent heat requirements induce a T depression for the gas in an otherwise linear distribution. This is progressively corrected further away from the drop until it becomes unnoticeable above $z > 5$. The vapour mass fraction, FIG. 6.3b, is dictated

by the local temperature at the interface but turns into an almost spherical distribution in the far field.

It seems adequate to provide some insights into such fundamental question as to how a water droplet heats up when it is placed on a hot substrate. This initial stage has received very little attention in the literature mainly due to the unsuitability to capture transient phenomena of the models employed. Hu & Larson [18, 80, 81, 82] or Girard *et al.* [103, 104, 105, 106] described the transient drop evolution as a sum of steady-state solutions and, therefore, could not capture the dynamics of the initial stage. The heating process is depicted in FIG. 6.4 for the case with $\hat{T}_w = 70\,^{\circ}\mathrm{C}$. The initial conditions (FIG. 6.4a) rapidly change due to the energy transport towards the drop from the heated substrate and from the surrounding gas. Some of this energy is absorbed by evaporation (strongest at the beginning given that $\omega_{t=0} = 0$) while the rest begins to increase the liquid temperature near the lower plate and along the interface. FIG. 6.4b reveals that this peripheral temperature rise is not uniform, nonetheless. There is a significantly larger downward heating taking place just below the apex related to the thermocapillary flow which is being established simultaneously within the drop, see 6.7a. Fluid from the contact line region (at higher T) is driven to the apex along the interface and then recirculated vertically downward towards the centre of the drop. This process (FIG. 6.4c, d, e) continues heating up the drop from the interior while the coldest location is slightly below the centre of the convection cell, i.e. $r \approx 0.8$, $z \approx 0.3$. Eventually the drop reaches the equilibrium state shown in FIG. 6.4f. The conclusion is, therefore, that the drop heating is dictated by the Marangoni-driven convection rather than by conduction.

6.2.2 Evaporation with moving contact line

The seminal work by Picknett & Bexon [78] provided a theoretical method to predict the phase-change rate and lifetime of drops evaporating according to the two pure theoretical modes, namely CA and CR. The authors only considered the isothermal case and, since the evaporative cooling leads to significant temperature disparities along the interface, the suitability of such approach to the heated-substrate scenario is a pending question. In order to obtain DNS results to fully test Picknett & Bexon's theory, in addition to the

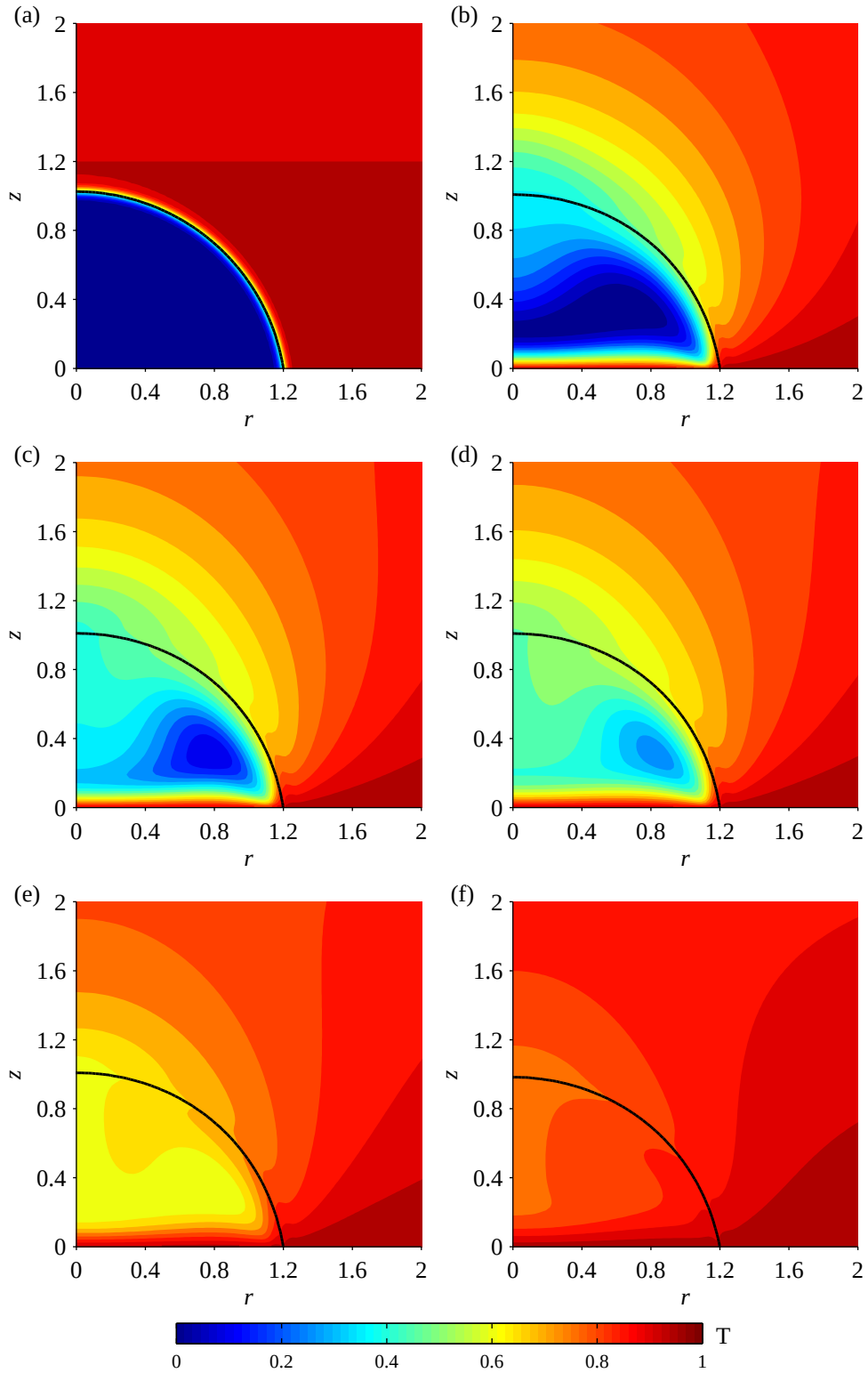

Figure 6.4: Transient heating of a water drop, initially at $\hat{T}_a$, placed on a substrate at $\hat{T}_w = 70\,^{\circ}\mathrm{C}$. (a) Initial conditions, $t = 0$, (b) $t = 1.7 \times 10^3$ (0.15 s), (c) $t = 3.4 \times 10^3$ (0.31 s), (d) $t = 5.1 \times 10^3$ (0.46 s), (e) $t = 1.1 \times 10^4$ (1.01 s), (f) $t = 6.7 \times 10^4$ (6.08 s).

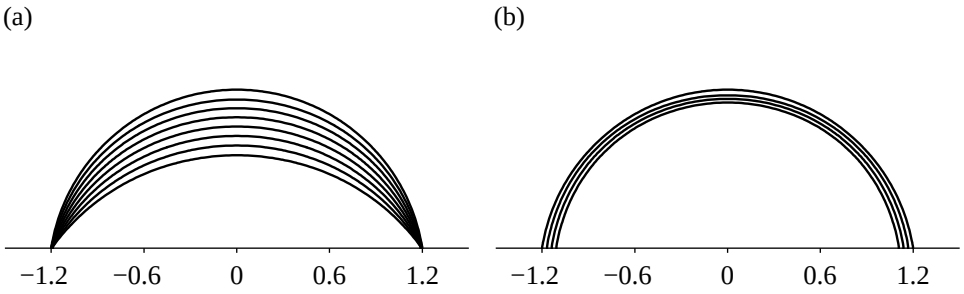

Figure 6.5: Snapshots of the interface at a time interval of 1.1×10^5 for a drop evaporating according to the (a) CR and (b) CA modes with $\hat{T}_w = 70\,^{\circ}\mathrm{C}$.

CR mode addressed in the previous section, we also aim to solve the drop evaporation according to the CA mode. Consequently, the challenge turns into a moving contact line (MCL) problem. The complexities of simulating such conditions have been thoroughly revisited in a recent annual review on the topic conducted by Sui *et at.* [108].

To date, only Karapetsas *et al.* [72] have numerically considered the MCL situation but, as pointed out by Sui *et at.* [108], they used a finite-element method for a single fluid with a free surface. Thus, DNS of a fully coupled two-phase flow with an MCL and phase change remains a challenge at this point [108]. In addition, it is important to empathise that Karapetsas *et al.* examined an intermediate pinned-receding contact line case rather than the pure CA mode making their results not adequate for comparison's purposes with either of the limiting modes.

The versatility of the DI method allows stimulating both CR and CA pure modes with minor changes as the interface thickness circumvents the stress singularity at the MCL (Seppecher [145], Jacqmin [140]). Over the last years, a number of models have been proposed to solve MCL problems, e.g. Qian *et al.* [146], Ding & Spelt [142], Carlson *et al.* [147] and Yue *et al.* [141]. The approach suggested by Ding & Spelt [142] is adopted here. The initial contact angle is, therefore, maintained by virtue of a Neumann boundary condition for c. For the velocity field, no slip is included as the slow contact line motion is solved by virtue of finite diffusion [108].

The reader should note that the generally tremendous complexity of predicting the location of a MCL is greatly simplified here due to the fact that its (very slow) motion is a consequence of evaporation only. A simple mass balance with the evaporation rate reveals that the contact line motion is a consequence of the liquid loss due to phase change rather

than due to capillary stresses. In other words, as the interface mass transfer rate goes to zero, so does the contact line velocity. From the numerical point of view, this is also tested by confirming that a drop wherein the liquid consumption has been artificially switched off, $S = 0$ in equation (6.8), results into a motionless contact line. Hence, the inertial-capillary regime (Sui *et at.* [108]) suggested by the Ohnesorge number $Oh = \hat{\mu}_l/\sqrt{\hat{\rho}_l \hat{\sigma}_0 \hat{H}_0}$, $O(0.001)$, in the context of spreading is not applicable for the slowly evaporating sessile drops under consideration.

FIG. 6.5 depicts the time evolution of the interface for the same drop evaporating according to the CR and CA modes. In both cases, the resulting deformable interface remains spherical as the drop volume decreases. The instantaneous evolution of the drop parameters is compared in FIG. 6.6. Preliminary results reflect the suitability of the DI model to represent the extreme evaporation modes. θ is effectively maintained while R and H decrease in the MCL case. Since the differences between modes are expected to be more noticeable towards the end of the drop lifetime, more data (currently being obtained) is necessary to assess whether the evolution of these parameters is linear or non-linear and to attempt a conclusive comparison with Picknett & Bexon [78]. The instantaneous evolution of V, see FIG. 6.6d, already shows that the evaporation rate in the CA mode is comparatively lower. This is in qualitative agreement with Picknett & Bexon [78], who predicted longer lifetimes with the CA mode. However, the deviation between V curves with a heated substrate seems to begin significantly earlier than what it is expected according to [78], wherein the disparity in V evolution is noticeable towards the end. This might be sign of important differences with respect to the isothermal configuration.

6.2.3 Three-dimensional phenomena

To date, the theoretical study of evaporating sessile drops has been restricted to the two-dimensional axisymmetric case for sake of simplicity. On this premise, experimental setups are meticulously designed to maximise the probability of producing drops with a perfectly circular contact area. In the majority of the cases and in most real-life applications, however, obtaining these ideal drops is an exception rather than the rule. In addition,

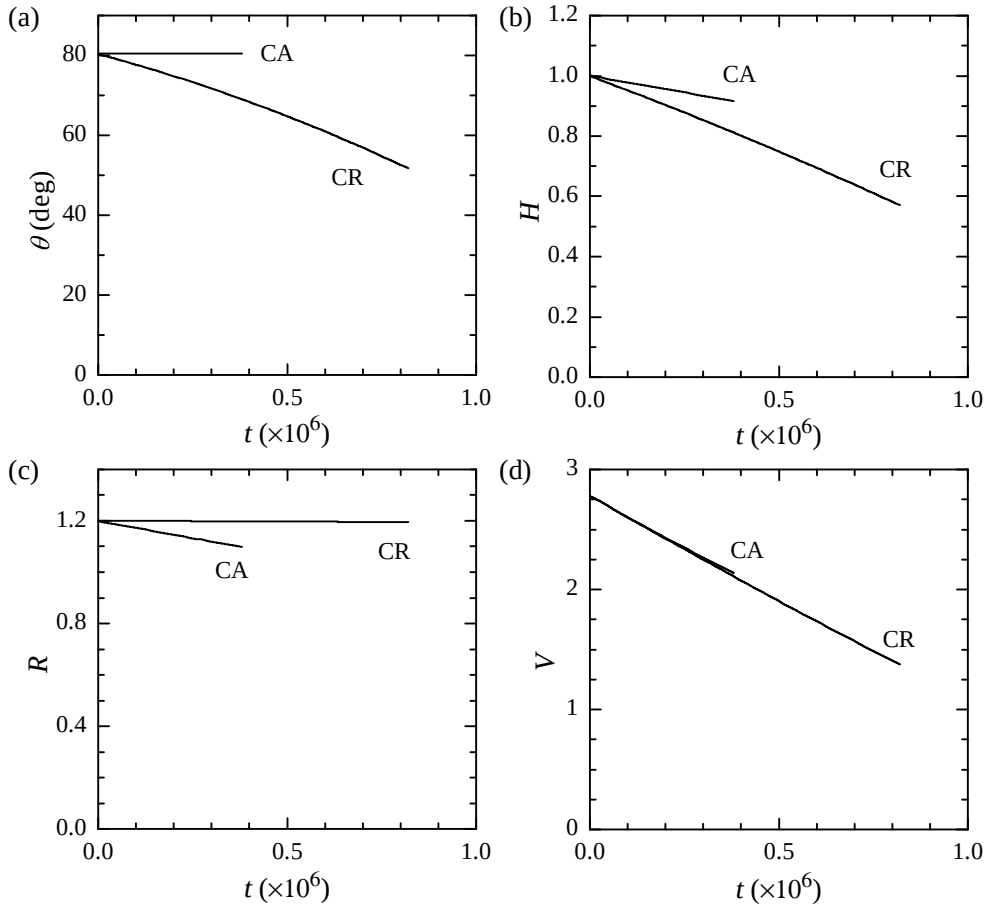

Figure 6.6: Instantaneous comparison between the parameters of a drop drying according to the CR and the CA evaporation modes with with $\hat{T}_w = 70\,^{\circ}\mathrm{C}$: (a) contact angle θ, (b) height H, (c) base radius R, (d) volume V.

even when this is achieved, an initially axisymmetrical drop will usually evolve into a deformed non-spherical cap after the first contact-line depinning. A real example showing this is provided in FIG. 5.2. In what follows, this investigation is restricted to PCL scenarios only.

6.2.3.1 Spherical drop

The spherical drop with $\hat{T}_w = 40\,^{\circ}\mathrm{C}$ earlier presented is considered here. In previous sections, it has been shown that the accurate resolution of this two-phase phase-change problem requires a very fine mesh resolution at the drop (to capture its intricate flow dynamics) as well as a very large domain (to obtain a realistic solution of the vapour distribution). In 3D, the computational cost of this configuration becomes unaffordable at this point. Nonetheless, the quasi-steady state nature of the system makes it possible to consider a smaller computational domain bounded with the field conditions provided by the 2D asymmetrical solution.

This strategy is employed to examine the drop at the beginning of the evaporation process ($H = 0.98$) and when its degree of non-equilibrium is close to the critical range for depinning observed in the experiments ($H = 0.3$), see FIG. 6.2. These two cases are selected to serve as reference against the non-spherical drops studied next. The former is compared in section 6.2.3.2 with a drop that for an unknown reason is deformed when placed onto the substrate. The latter provides a point of reference to illustrate what happens when the SS mode leads to a completely non-uniform drop after the first contact line jump, see section 6.2.3.3.

The horizontal size of the computational domain is $L_x = L_y = 3R_0$ while the vertical dimension is $L_z = L_x/2$ and $L_x/4$ for $H = 0.98$ and $H = 0.3$, respectively. A structured uniform mesh with $250 \times 250 \times 125$ elements is used in both cases. The governing dimensionless groups are available in TABLE 6.3.

A detailed description of the flow within the drop is illustrated in FIG. 6.7a. The non-uniform temperature along the interface, hottest near the contact line due to heating effect of the substrate and coldest at the apex due to the evaporative cooling, generate a cell-like Marangoni-driven flow qualitatively similar to that previously reported by Ruiz &

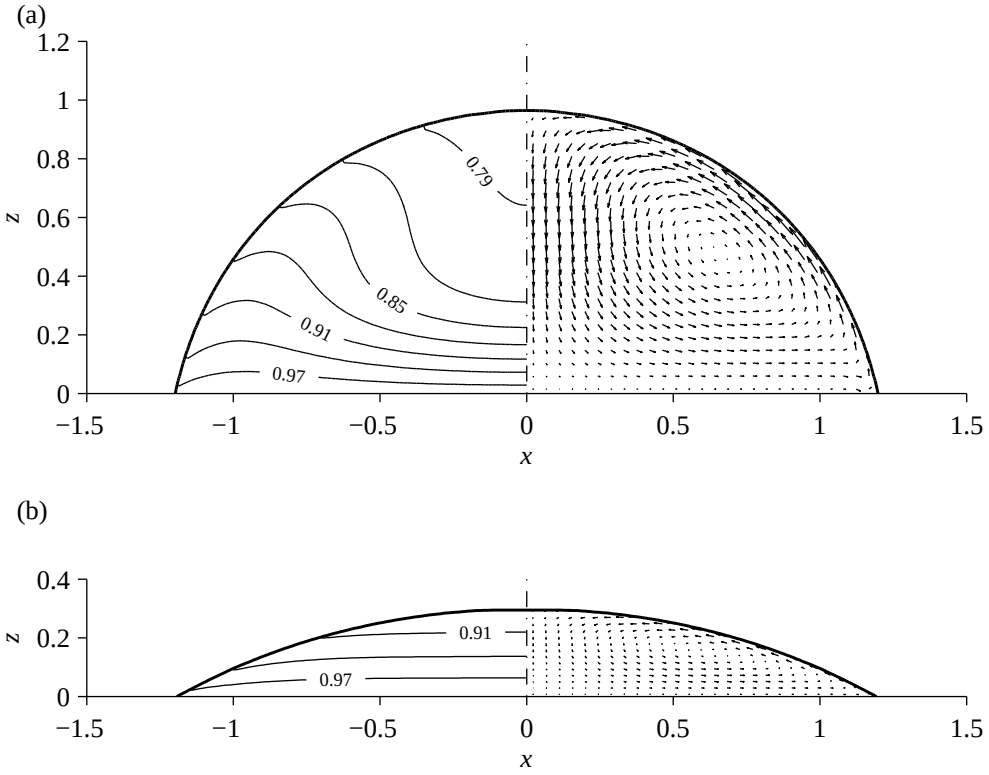

Figure 6.7: Drop temperature (left) and velocity (right) for different drop heights with $\hat{T}_w = 40\,^{\circ}\mathrm{C}$. (a) $H = 0.98$ (Experiment: FIG. 5.2a); (b) $H = 0.3$ (Experiment: FIG. 5.2c).

Black [102], Mollaret *et al.* [89], Girard *et al.* [103, 104, 105, 106] with heated substrates. However, it should be noted that the drop temperature in Mollaret *et al.* [89] and Girard *et al.* [103, 104, 105, 106] is significantly more uniform. Their numerical simulations reveal essentially isothermal drops, i.e. $(\hat{T}_w - \hat{T}_{apex})/\hat{T}_w < 1\%$. This contradicts the experimental evidence provided by our IR recordings, and supported by the numerical results of our two-phase model, which indicates T differences between the contact line and the apex ~10-20%. Hence, this notorious discrepancy is probably associated with the previously mentioned oversimplifications of one-sided models. Hu & Larson [81, 82] also provide insights into the bulk flow for non-heated substrates but the validity of their analysis is restricted to the last stage of the evaporation process, $\theta < 40°$, due to the use of the lubrication approximation.

Towards the end of the evaporation process, the progressive change in H has perceptible impact in the flow, see FIG. 6.7b. In agreement with the experimental observations,

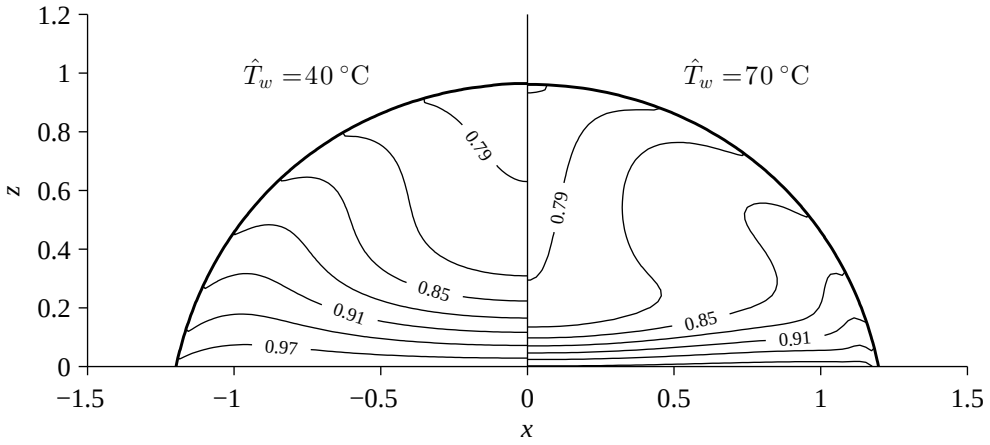

Figure 6.8: Comparison between the temperature distribution for the same drop ($H = 0.98$) evaporating at different levels of substrate heat: $\hat{T}_w = 40\,^{\circ}\mathrm{C}$ (left) and $\hat{T}_w = 70\,^{\circ}\mathrm{C}$ (right).

T rises and becomes more homogeneous due to the smaller drop thickness. The smoother T gradients tangent to the interface (driving force) maintain convection cells qualitatively similar but of smaller speed. The temperature distribution within the drop is also highly dependent on the strength of the Marangoni flow, see FIG. 6.8. For a given H, the dominance of thermocapillary convection increases with increasing $\hat{T}_w$, which leads to drops with a colder core due to the vertically-downward advection of liquid (at lower T) occurring below the apex. This enhanced Marangoni-driven cooling effect within the drop intensifies $\partial T/\partial z$ near the substrate suggesting a superior heat transfer from the hot substrate.

As expected, these cases provide axisymmetric results. However, they have been examined in 3D to validate the code and to serve as reference for the non-spherical cases studied next.

6.2.3.2 Elliptical contact area

Before attempting to investigate a drop with a completely irregular contact area, a slightly simpler case (with well-defined principal directions) is considered to help elucidate some of the fundamental dynamics related to three-dimensional phenomena. Let us consider that the initial contact area of the drop presented in FIG. 6.7a is elliptical rather than circular. This is not an unrealistic configuration at all given that it can be frequently

found in situations where droplet deposition is not exactly perpendicular to the substrate, e.g. vertical dosing onto inclined substrates, drops released at certain angle due to setup configurations or even due to convection currents in the gas, etc.

To provide the drop volume, the initial drop shape is arbitrarily assumed to be that of a semi-ellipsoid. Hence, the interface location is given in Cartesian coordinates by,

$$\frac{x^2}{a^2} + \frac{y^2}{b^2} + \frac{z^2}{c^2} = 1, \tag{6.14}$$

where a, b and c are the semi-axis lengths along the x, y and z directions, respectively. The volume of a semi-ellipsoid V_e is,

$$V_e = \frac{2}{3}\pi abc, \tag{6.15}$$

while the base circumference C_e can be estimated according to Ramanujan's second approximation, i.e.,

$$C_e \approx \pi\,(a+b)\left(1 + \frac{3h}{10 + \sqrt{4-3h}}\right), \tag{6.16}$$

where $h = (a-b)^2/(a+b)^2$. It is known that the overall evaporation rate of a sessile drop is proportional to its size (volume) and to the length of its contact line. Thus, a, b and c are selected so that the resulting ellipsoidal geometry provides the same volume and base perimeter as those for the spherical drop examined in FIG. 6.7a, i.e., $V_e = V_s$ and $C_e = C_s$ where V_s and C_s are the volume and base circumference of the spherical drop with $H = 0.98$ and $R = 1.2$. Equations (6.15) and (6.16) form a set of two equations with three unknowns. The missing expression necessary to complete a independent system is provided by the degree of deformation in the horizontal direction $\Lambda = a/b$, which is chosen to be $\Lambda = 3/2$. It follows that the resulting ellipsoidal geometry is defined by $a = 1.426$, $b = 0.951$ and $c = 0.955$. The governing parameters are maintained equal to those employed in the spherical case to allow direct comparison.

Our simulations suggest that an ellipsoid is not a possible shape for a drop with an elliptical pinned contact line. The initial drop geometry (arbitrarily selected) undergoes a rapid change as surface tension enforces the interface surface-area minimization for the

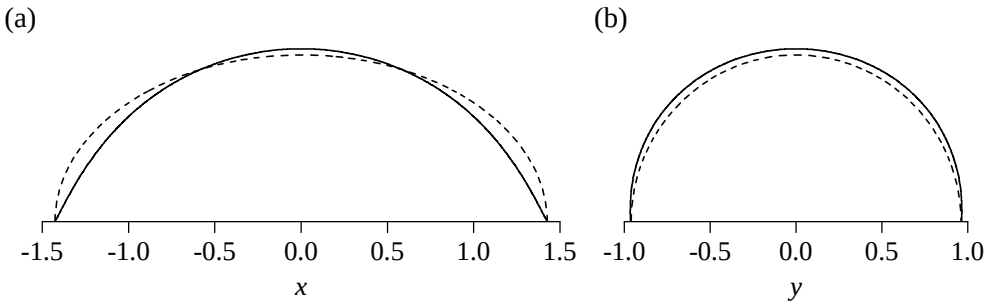

Figure 6.9: Initial (dashed line) and quasi-steady (solid line) interface profile along the principal (a) xz and (b) yz planes for a drop with an elliptical contact area whose base circumference and volume are equal to those of the spherical drop with $H = 0.98$ ($R = 1.2$) examined in section 6.2.3.1. The governing parameters are listed in TABLE 6.3 ($\hat{T}_w = 40\,^{\circ}\mathrm{C}$).

given volume. FIG. 6.9 illustrates the initial shape (dashed line) together with the final quasi-steady drop profile (solid line). The pinned contact line impedes the formation of a sphere but surface tension drives the drop shape to reach the closest possible configuration. In an attempt to even the different axis lengths, there is interface pulling along the longest axis, x, while the geometry expands in the other two directions, y and z. For the same volume and base perimeter, the interface area of the quasi-steady drop is smaller than the area of an ellipsoid (98.8%) but larger than the area of a spherical cap (101.2%). It is important to note that this initial shape adjustment is not caused by evaporation. The time interval in which this takes place is so short that the volume difference between the initial and the quasi-steady drop shape is negligible ($\Delta V \approx 0.1\%$). The resulting contact angle is not constant along the triple line as it happens in the spherical case. Here, θ progressively changes between 58° (at xz-plane with $y = 0$) and 94° (at yz-plane with $x = 0$) as shown in FIG. 6.10a. The range of contact angle variation throughout the base line, $\Delta\theta = \theta_{\max} - \theta_{\min} = 36°$ with $\Lambda = 3/2$, increases for increasing degree of deformation Λ. If $\Lambda = 1$ (spherical cap) the contact angle is constant everywhere, i.e. $\Delta\theta = 0$. In addition, $\Delta\theta$ changes in time due to evaporation ($\Delta\theta$ decreases for decreasing V).

The resulting evaporation rate $M(t)$ is 2.3% larger than that for the spherical drop, which is in accordance with the surface area increment. The interface T distribution is presented in FIG. 6.10b. The strength of the Marangoni effect varies along each radial trajectory given that the temperature difference, from $T = 1$ at the contact line to $T = 0.77$ at the apex, occurs along paths with different lengths and local curvature. The flow characteristics is different for each vertical section across the z axis. The temper-

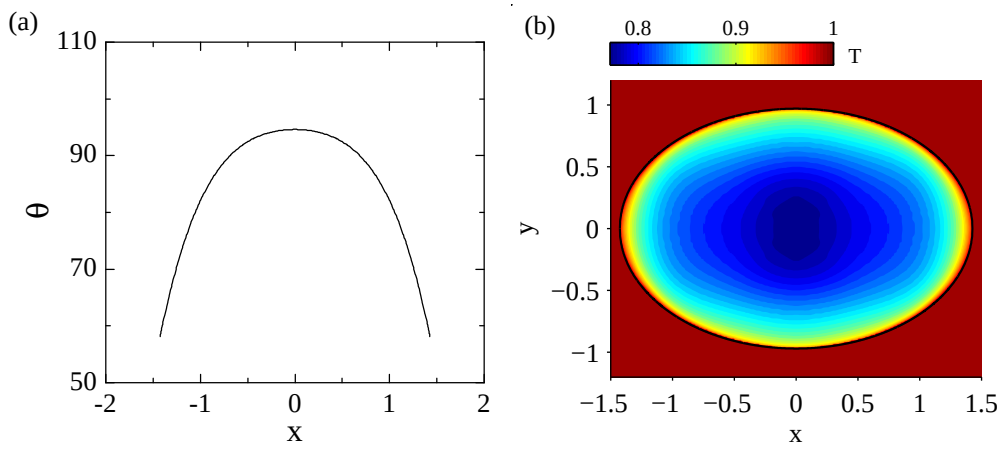

Figure 6.10: (a) Contact angle variation along the triple line and (b) interface temperature for a drop with an elliptical contact area as that described in FIG. 6.9. These figures show the contact angle and temperature of the 3D drop found right after the initial geometry adjustment ($V - V_0 \approx 0.1\%$).

ature and velocity fields for the principal planes of reference are depicted in FIG. 6.11. Although qualitatively similar, the convection patterns and temperature distribution are more elongated along the yz plane due to the effect of the drop deformation. Intermediate sections obey transitional features between those shown in FIG. 6.11.

6.2.3.3 Non-uniform drop

The experiments showed (FIG. 5.2) that a perfectly spherical drop normally results into a non-spherical cap with a irregular contact area after the first contact-line jump at critical non-equilibrium conditions ($H \approx 0.3$ and $\theta \approx 22°$). The recreation of the system's dynamics just before the 3D readjustment (which experimentally corresponds to FIG. 5.2c) have been examined in FIG. 6.7b. Now we aim to provide more insights into the flow and evaporation process of a more realistic drop found right after the first sudden jump (which experimentally corresponds to FIG. 5.2d).

The 3D drop shape considered is depicted in FIG. 6.12a. FIG. 6.12b shows the final contact line location together with its position prior to the droplet depinning (FIG. 6.7b). It must be empathised that, contrary to the MCL problem investigated in section 6.2.2, the contact-line motion within the SS stage is triggered (due to the liquid loss that eventually makes the drop reach the critical conditions for the depinning) but *not directly governed* by evaporation. Thus, the three-dimensional motion has to be evaluated according to that of an inertial-capillary regime, see Sui *et at.* [108]. Since this complex problem is

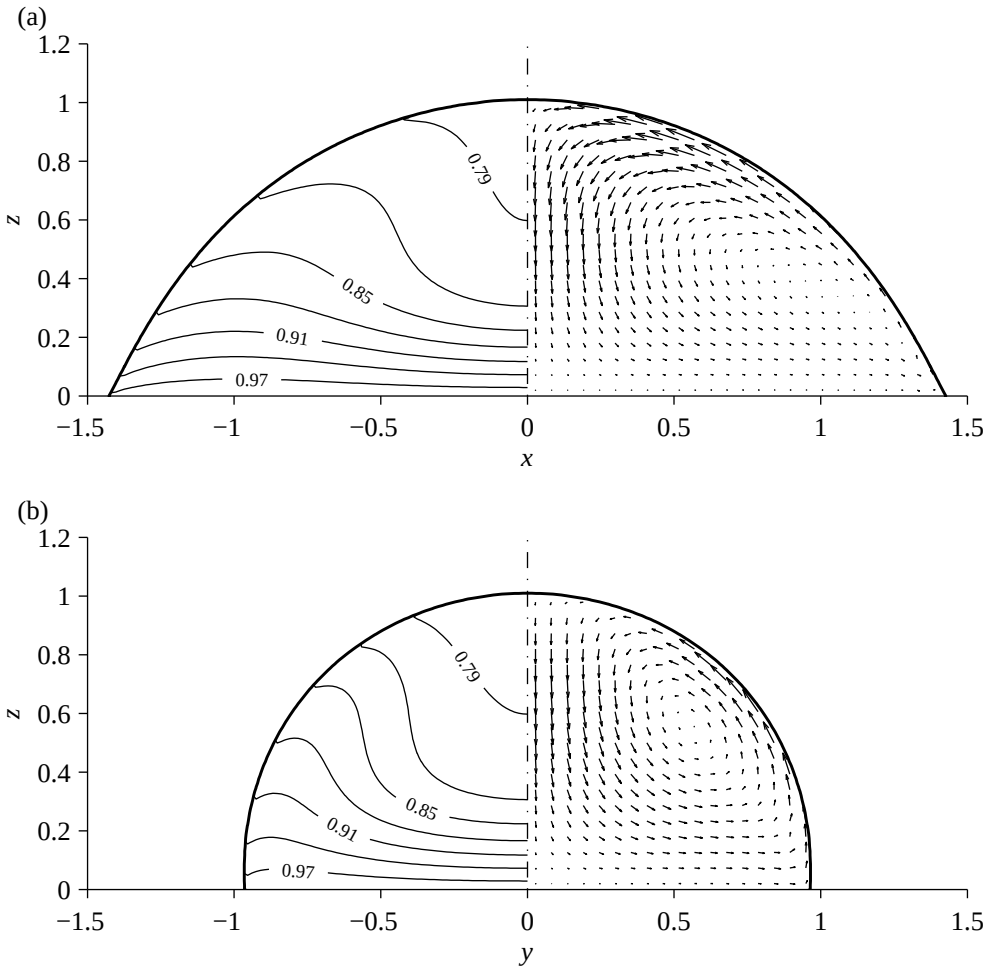

Figure 6.11: Drop temperature (left) and velocity (right) along the (a) xz- ($y = 0$) and (b) yz- ($x = 0$) planes for the drop presented in FIG. 6.9.

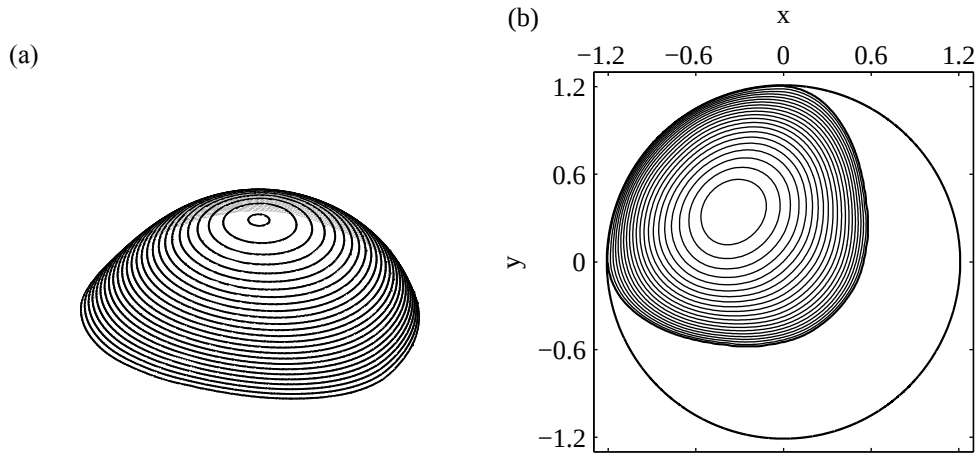

Figure 6.12: Drop with non-uniform contact area representing (approximately) the case experimentally observed (FIG. 5.2d) just after the first contact line jump with $\hat{T}_w = 40\,^{\circ}\mathrm{C}$. (a) 3D geometry; (b) Contact line before and after the first drop depinning. The flow just before the contact-line jump is examined in FIG. 6.7b.

beyond the scope of this investigation, we do not attempt to predict the instantaneous contact-line evolution between pinned locations. Instead, we simply consider a new PCL case whose contact-area approximately recreates that experimentally observed in FIG. 5.2d.

The CCD recordings revealed a quasi-instantaneous drop readjustment and, therefore, a negligible change in volume between the original and the new pinning positions, see FIG. 5.5d. For this reason, the same volume than that of the drop preceding the depinning is given to the new drop. More data is necessary before we are in the position of providing more conclusive and quantitative findings. However, we can already observe that the 3D drop shape, which results from the effect of surface tension as in the ellipsoidal configuration, has a surface area significantly smaller to that in FIG. 6.7b. Consequently, the evaporation rate decreases in a percentage of the same order of magnitude, which is in agreement with the experiments as they reveal comparatively lower evaporation rates as the drops enter the SS stage.

The evolution of θ is presented in FIG. 6.13. The contact line coordinates and its corresponding local contact angle are given according to two segments to allow the representation of the 3D data in a 2D plot. At this point, the main conclusion that it can be drawn is the obvious increasing complexity with respect to the spherical and ellipt-

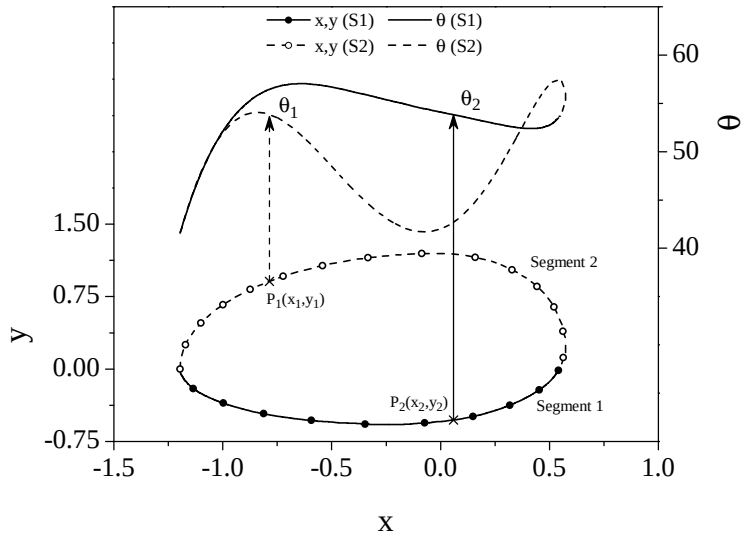

Figure 6.13: Contact angle distribution along the triple line for a drop with a non-uniform contact area as that shown in FIG. 6.12.

ical configurations. θ ranges from 41° to 57°. Consistently with the concepts discussed around FIG. 6.10a, there seem to be pairs of "mirrored" points with the same contact angle. Locations of minimum θ appear to be those whose horizontal separation is maximum, while the points of maximum θ seem to be in the direction perpendicular to that connecting the former. This observation suggests that θ can be evaluated in terms of a degree of horizontal deformation as in FIG. 6.10a. Once again, more results (currently being obtained) are required to make conclusive statements.

6.3 Conclusions

A novel model based on the diffuse-interface method has been developed to address the fully-coupled two-phase direct numerical simulation of evaporating sessile drops on heated substrates. The main advantage of this approach with respect to previous works available in the literature is that the gas phase is completely solved which allows a more realistic recreation of the system's dynamics. Both interface mass and heat transfer are computed based on the local conditions, these obtained with general advection-diffusion equations rather with the traditionally-used Laplace approximation. The versatility of the diffuse-interface methodology provides the means to solve not only pinned drops but also the more complex case of drops evaporating with a receding contact line. The interface is

deformable and, therefore, the drop geometry is part of the solution.

Pinned drops evaporating at different levels of heat have been simulated. The instantaneous volume decrease linearly while the contact angle and drop height do at a progressively increasing rate in agreement with the experimental work presented in Chapter 5. The initial transient stage has been investigated concluding that the drop heating is mainly governed by Marangoni convection rather than by energy conduction. Consequently, the drop is convectively heated through its core flow rather than via conduction mechanisms along its periphery.

For the first time, the direct numerical simulation of a fully coupled two-phase flow with a moving contact line and phase change has been addressed by simulating the drying process of a drop according to theoretical contact angle mode. In this configuration, the contact line recedes due to the transient mass loss of liquid. The suitability of the diffuse-interface model to resolve this problem has been demonstrated. Preliminary results show qualitative agreement with the predictions by Picknett & Bexon [78] for the non-heated case. However, early deviations in the evaporation rate for the constant angle mode might suggest deviations not captured in isothermal case [78]. More results are necessary to conclusively asses the applicability of Picknett & Bexon's theory to heated drops, wherein the thermal gradients along the interface are prohibitively large.

In the last part of the chapter, the attention of this work has turned into three-dimensional phenomena in which, to the best of our knowledge, compromises the first attempt in the context of theory and simulations. A spherical drop has been considered initially to validate the 3D results and to provide more insights into the dynamics of the drop, which change with time and with the level of heat. Two non-spherical cases have been examined subsequently. A drop with an elliptical contact area, which illustrates occurrences found when the dossing trajectory is not perfectly perpendicular to the solid surface, has been examined revealing a varying distribution of the contact angle along the triple line. Inherent to non-spherical drops, this range of contact angles appears due to the interface-area minimization driven by surface tension. The amplitude of the range is found to depend on the degree of deformation of the contact area and on the volume of the drop. Thus, the resulting flow within the drop is different at each vertical

section. This has been presented for the principal directions. To conclude, the more complex case of a evaporating drop with non-uniform contact line has been investigated. The subject drop recreates the typical irregular configurations experimentally observed after the first contact line jump characteristic of the stick-slip final stage near the drop dry-out. Preliminary results indicate a less homogeneous local contact angle variation and complex fully three-dimensional flow features within the drop. It is concluded that non-circular contact areas lead to intricate drop shapes governed by a three-dimensional interface contraction/expansion equilibrium dictated by surface tension and with variable contact angle along the triple line.

Chapter 7

Conclusions and Future Work

For sake of conciseness and given that comprehensive conclusions have been provided at the end of each chapter, only an overview with the fundamental findings emerging from this investigation is provided in section §7.1. This thesis concludes in section §7.2 with the recommended actions for future works attempting to shed more light on the dynamics, stability and phase change of thermocapillary flows.

7.1 Conclusions

Whether a horizontally-heated planar liquid layer or a sessile drop on a heated substrate is considered, the resulting bulk flow in both the liquid and in the surrounding gas may be significantly affected by the Marangoni effect. Despite the more complex singularities inherent to evaporating drops, some of the physics underlying both systems bear similarities and, therefore, have been studied employing similar approaches in the past. Representative examples focusing (theoretically or numerically) on the stability of planar layers are, for instance, those by Smith & Davis [11, 30], Xu & Zebib [42], Bucchignani [43] or Sim *et al.* [45]. Similarly, a flavour of previous approaches significant to the sessile drop problem can be acquired from Picknett & Bexon [78], Deegan *et al.* [20, 21], Hu & Larson [18, 80, 81], Girard *et al.* [103, 104, 105, 106] or Karapetsas *et al.* [72]. To date, all these works have completely or partially disregarded the effect of the gas phase by invoking the so-called "one-sided" or "1.5-sided" approximations, which decouples the dynamics of the

two phases including the interface allowing to concentrate solely on the liquid. Additionally, in the few cases in which either the gas temperature of the vapour distribution are addressed, the dynamics of these have been solved accounting for diffusion mechanisms only. Throughout this thesis the philosophy has been to avoid these and similar simplifications by developing two-phase models grounded in general advection-diffusion transport equations and accounting for interfacial deformations. This distinctive capability permits not only to capture advection-related phenomena in the gas obviated in the past but also to solve the interface energy, mass and momentum balances according to more realistic local conditions.

Following these guidelines a model based on the Volume-of-Fluid method has been developed to examine the stability of laterally-heated shallow liquid layers under saturated environments (Chapter 3). The hydrothermal-wave instability obliquely propagating has been observed showing good agreement with experiments, Riley & Neitzel [40], and linear theory, Smith & Davis [11, 30]. The implementation of a deformable interface has revealed previously unknown interfacial waves also arising in unstable regimes. We have concluded the chapter showing that the transient nature of these travelling thermal fluctuations have a significant effect on the mechanism of heat transfer across the interface never captured before. The model used for liquid layers under saturated environments has been enhanced to address phase change in a subsequent stage (Chapter 4). Further validation has been provided before assessing the impact of evaporation on the hydrothermal waves. Analysis of the onset and growth of the oscillatory regime has shown a stabilizing-destabilizing effect associated with the interface mass transfer: the latent-heat consumption due to evaporation mitigates the inception of the thermal fluctuations whereas the associated liquid consumption promotes the interfacial waves. The dynamics of the gas phase have been extensively examined noticing the significance of instability-induced convective mechanisms on the local vapour distribution. Interestingly, high (low) concentration regions of vapour appear at a certain small distance above cold (hot) spots, even though the vapour concentration right at the interface follows exactly the opposite tendency as expected. Our results also show that the advection in the gas associated with the Marangoni effect plays a major role in the bulk vapour distribution as well as in the

local evaporation flux along the interface and can lead to areas of local condensation in an otherwise evaporating liquid layer. These results illustrate the importance of some of the physical mechanisms obviated by the previously-mentioned simplified models.

The second part of this thesis has been devoted to the study of similar phenomena in evaporating sessile drops. This new problem has been approached in the laboratory first (Chapter 5). An experimental apparatus has been designed to allow the accurate investigation of water drops evaporating on a heated copper substrate and surrounded by a controlled nitrogen environment. The phase change has been simultaneously recorded from the side with digital camera and from the top with an infrared camera allowing the capture of the instantaneous drop characteristics along with the interface thermal signature and three-dimensional contact line motion. Typically a drop evaporates for 70% of the time with its contact line pinned before it enters a stick-slip stage wherein the drop dries undergoing contact line jumps. The critical disequilibrium conditions bounding the end and beginning of these phases have been identified. For lower temperatures an intermediate stage has been observed wherein the drop evaporates according to a combined mode with a smoothly receding contact line and contact angle. To conclude, this experimental work has been complemented with accompanying direct numerical simulations (Chapter 6). A new model based on the diffuse-interface method has been developed to solve the more intricate problem of sessile drops, especially due to the contact-line dynamics and non-uniform geometry. Drops evaporating at different levels of heat have been simulated observing excellent agreement with the experimental data. Further insights into the two-phase flow dynamics have been provided as well as into the initial transient stage, in which the Marangoni effect has been found to play a major role in the droplet heating. The resourcefulness of the diffuse-interface methodology has allowed us to recreate the two pure modes of evaporation, namely the constant-radius and constant-angle modes, to evaluate the applicability of the theory Picknett & Bexon [78] (and similar subsequent works) to the heated configuration. The last part of Chapter 6 has been dedicated to the investigation of three-dimensional phenomena on what, to the extent of our knowledge, represents the first attempt in this context. Drops with non-circular contact areas have been found to exhibit a sophisticated contact-angle distribution along the triple line due to

the complex three-dimensional drop geometries dictated by interface tension as this tries to minimise the surface area for the given volume. The resulting evaporation rate varies due to three-dimensional features as well as the two-phase flow, which become different for each vertical section across the drop centre.

7.2 Future Work

The physical richness and relevance of such fundamental topics as those addressed in this thesis make the space for further research not only vast but also attractive for several applications. More investigations are required especially along the lines of the work on drops presented in Chapters 5 and 6. To begin with, gravity has been left out at this point for sake of simplicity. However, there is experimental evidence that strongly suggests the importance, and probably leading role, of buoyancy in the govern of the gas dynamics. With minor updates, similar to those presented for the liquid layer, our diffuse-interface model will be capable of capturing this advection-related phenomenon to provide more insights into this matter. The recent development of an experimental technique that uses infrared tomography to measure the three-dimensional vapour distribution above evaporating drops, see Kelly-Zion *et al.* [148], makes this problem particularly interesting as it would allow direct comparison between numerical and experimental data. Configurations in which there are externally imposed convection currents in the gas also become new and very interesting opportunities.

The addition of the solid substrate to the current model is a potential new feature that is highly desirable too. This would allow the complete three-phase simulation of drops evaporating on substrates with lower thermal conductivities and thermal mass to that considered here. Under such conditions, the works by David *et al.* [90] and Dunn *et al.* [73] suggest major effects of the substrate's thermal properties on the energy distribution as well as lifetime of the drops.

We have addressed the two pure evaporation modes, namely constant-radius and constant-angle, however experiments have shown that there is a significant number of intermediate scenarios wherein the drops usually dry according to some combinations of

these. There are stages in the evaporation process which are subject to combined modes, wherein both the drop radius and contact angle reduce smoothly, while in others the contact line jumps between pinned positions. Predicting the contact line motion in these scenarios would be really interesting but also tremendously challenging (specially in the latter case due to its inertial-capillarity nature). As pointed out by Sui *et at.* [108], the use of the currently available moving contact line models is justified provided that the grid spacing in the contact line region is small enough for the viscosity and surface tension to be the dominant forces. In other words, the mesh must be able to resolve flows not only on the macroscale, but also simultaneously on the microscale, which is easily below $O(10^{-4})$ of the macroscale [108]. Since the rest of the domain does not need to be so finely gridded, adaptive mesh refinement algorithms seem a necessary ingredient to attempt the challenge. These combined macro-micro simulations of evaporating drops would also allow to fully understand better the phase-change process as it is known that the evaporation flux is critically affected by the disjoining pressure which becomes relevant in the microscopic thin film at the contact line.

To conclude, it should be noted that at this point we also have all the ingredients necessary to address one of the end-goals of this investigation, the numerical simulation of the hydrothermal-wave like instabilities observed in sessile drops by Sefiane *et al.* [66]. To that end, similar simulations to those presented here are planned to be performed shortly with FC-72, ethanol and methanol, as drops of these liquids are known to be prone to develop into unstable regimens.

List of Publications

Conferences (*Oral presentations)

1. Sáenz P. J., Valluri P., and Sefiane K. Understanding the physics and stability of evaporating drops. *Chemical Engineering Day UK 2014*. University of Manchester, Manchester, UK (2014).

2. *Sáenz P. J., Valluri P., Sefiane K., Karapetsas G., Kim J., and Matar O. K. Dynamics of evaporating droplets. *American Physical Society, 66th Division of Fluid Dynamics Meeting*. Pittsburgh, Pennsylvania, US (2013).

3. Sáenz P. J., Valluri P., and Sefiane K. Thermocapillary instabilities. *Chemical Engineering Day UK 2013*. Imperial College London, London, UK (2013).

4. *Sáenz P. J., Valluri P., Sefiane K., Karapetsas G., and Matar O. K. On phase change in thermocapillary flows. *American Physical Society, 65th Division of Fluid Dynamics Meeting*. San Diego, California, US (2012).

5. *Sáenz P. J., Valluri P., Sefiane K., Karapetsas G., and Matar O. K. Two-phase investigation of hydrothermal waves in saturated atmospheres. *American Physical Society, 65th Division of Fluid Dynamics Meeting*. San Diego, California, US (2012).

6. *Sáenz P. J. On the dynamics of Marangoni-driven flows. Stability, phase change and other physical mechanisms. *Institute for Materials and Processes Seminar Series*. University of Edinburgh, Scotland, UK (2012).

7. *Sáenz P. J., Valluri P., Sefiane K., Karapetsas G., and Matar O. K. Numerical study of thermocapillary instabilities in evaporating annular pools and sessile droplets.

American Physical Society, 64th Division of Fluid Dynamics Meeting. Baltimore, Maryland, US (2011).

8. *Sefiane K., Karapetsas G., Sáenz P. J., Valluri P., and Matar O. K. Numerical study of the evaporation of sessile drops: formation of hydrothermal waves. *American Physical Society, 63rd Division of Fluid Dynamics Meeting.* Long Beach, California, US (2010).

9. *Sáenz P. J., Valluri P., Karapetsas G., Sefiane K., and Matar O. K. Hydrothermal waves in evaporating annular pools and sessile drops using DNS. *American Physical Society, 63rd Division of Fluid Dynamics Meeting.* Long Beach, California, US (2010).

Journal Articles

1. Sáenz P. J., Valluri P., Sefiane K., Matar O. K., and Kim J. Two-phase evaporation of sessile drops. Experiments and direct numerical simulations with three-dimensional phenomena. *(To be submitted to J Fluid Mech)*

2. Sáenz P. J., Valluri P., Sefiane K., Karapetsas G., and Matar O. K. On phase change in Marangoni-driven flows and its effects on the hydrothermal-wave instabilities. *Physics of Fluids* 26(2): 024114, 2014. DOI 10.1063/1.4866770.

3. Sáenz P. J., Valluri P., Sefiane K., Karapetsas G., and Matar O. K. Linear and nonlinear stability of hydrothermal waves in planar liquid layers driven by thermocapillarity. *Physics of Fluids* 25(9): 094101, 2013. DOI 10.1063/1.4819884.

List of Figures

List of Tables

Bibliography

[1] R. Hooke. An attempt for the explication of the phenomena observable in an experiment published by the Right Hon. Robert Boyle, in the 35th experiment of his Epistolical Discourse touching the Air, in confirmation of a former conjecture made by R. Hooke, 1661.

[2] T. Young. An essay on the cohesion of fluids. *Philosophical Transactions of the Royal Society of London*, 95:65–87, 1805.

[3] J. Thomson. Xlii. on certain curious motions observable at the surfaces of wine and other alcoholic liquors. *Philosophical Magazine Series 4*, 10(67):330–333, 1855.

[4] C. G. M. Marangoni. *On the spreading of liquid droplets.* PhD thesis, Unversity of Pavia, 1865.

[5] J. W. Gibbs. *On the equilibrium of heterogeneous substances*, volume 3. Transactions of the Connecticut Academy of Arts and Sciences, 1874-1878.

[6] A. Einstein. Folgerungen aus den capillaritätserscheinungen. *Annalen der Physik*, 309(3):513–523, 1901.

[7] P. De Gennes, F. Brochard-Wyart, and D. Quéré. *Capillarity and wetting phenomena: drops, bubbles, pearls, waves.* Springer, 2004.

[8] N. Garnier, A. Chiffaudel, and F. Daviaud. Hydrothermal waves in a disk of fluid. *Dynamics of Spatio-Temporal Cellular Structures: Henri Benard Centenary Review*, 207:147–161, 2006.

[9] D. Schwabe, A. Scharmann, F. Preisser, and R. Oeder. Experiments on surface-tension driven flow in floating zone-melting. *Journal of Crystal Growth*, 43(3):305–312, 1978.

[10] H. C. Kuhlmann. *Thermocapillary convection in models of crystal growth*. Springer Tracts in Modern Physics (Book 152). Springer, 1999.

[11] M. K. Smith and S. H. Davis. Instabilities of dynamic thermocapillary liquid layers. Part 1. Convective instabilities. *Journal of Fluid Mechanics*, 132(Jul):119–144, 1983.

[12] D. Schwabe and A. Scharmann. Some evidence for the existence and magnitude of a critical Marangoni number for the onset of oscillatory flow in crystal-growth melts. *Journal of Crystal Growth*, 46(1):125–131, 1979.

[13] C. H. Chun and W. Wuest. Experiments on the transition from the steady to the oscillatory Marangoni-convection of a floating zone under reduced gravity effect. *Acta Astronautica*, 6(9):1073–1082, 1979.

[14] D. Schwabe, A. Zebib, and B. C. Sim. Oscillatory thermocapillary convection in open cylindrical annuli. Part 1. Experiments under microgravity. *Journal of Fluid Mechanics*, 491:239–258, 2003.

[15] K. Sefiane. On the formation of regular patterns from drying droplets and their potential use for bio-medical applications. *Journal of Bionic Engineering*, 7:S82–S93, 2010.

[16] J. P. Jing, J. Reed, J. Huang, X. H. Hu, V. Clarke, J. Edington, D. Housman, T. S. Anantharaman, E. J. Huff, B. Mishra, B. Porter, A. Shenker, E. Wolfson, C. Hiort, R. Kantor, C. Aston, and D. C. Schwartz. Automated high resolution optical mapping using arrayed, fluid-fixed DNA molecules. *Proceedings of the National Academy of Sciences of the United States of America*, 95(14):8046–8051, 1998.

[17] M. Chopra, L. Li, H. Hu, M. A. Burns, and R. G. Larson. DNA molecular configurations in an evaporating droplet near a glass surface. *Journal of Rheology*, 47(5):1111–1132, 2003.

[18] H. Hu and R. G. Larson. Evaporation of a sessile droplet on a substrate. *Journal of Physical Chemistry B*, 106(6):1334–1344, 2002.

[19] S. Karlsson, A. Rasmuson, I. N. Bjorn, and S. Schantz. Characterization and mathematical modelling of single fluidised particle coating. *Powder Technology*, 207(1-3):245–256, 2011.

[20] R. D. Deegan, O. Bakajin, T. F. Dupont, G. Huber, S. R. Nagel, and T. A. Witten. Capillary flow as the cause of ring stains from dried liquid drops. *Nature*, 389(6653):827–829, 1997.

[21] R. D. Deegan, O. Bakajin, T. F. Dupont, G. Huber, S. R. Nagel, and T. A. Witten. Contact line deposits in an evaporating drop. *Physical Review E*, 62(1):756–765, 2000.

[22] A. Bar-Cohen, M. Arik, and M. Ohadi. Direct liquid cooling of high flux micro and nano electronic components. *Proceedings of the Ieee*, 94(8):1549–1570, 2006.

[23] V. Dugas, J. Broutin, and E. Souteyrand. Droplet evaporation study applied to DNA chip manufacturing. *Langmuir*, 21(20):9130–9136, 2005.

[24] H. Sirringhaus, T. Kawase, R. H. Friend, T. Shimoda, M. Inbasekaran, W. Wu, and E. P. Woo. High-resolution inkjet printing of all-polymer transistor circuits. *Science*, 290(5499):2123–2126, 2000.

[25] H. Bénard. The cellular whirlpools in a liquid sheet transporting heat by convection in a permanent regime. *Annales De Chimie Et De Physique*, 23:62–101, 1901.

[26] L. Rayleigh. On convection currents in a horizontal layer of fluid, when the higher temperature is on the under side. *Philosophical Magazine*, 32(187-92):529–546, 1916.

[27] M. J. Block. Surface tension as the cause of Benard cells and surface deformation in a liquid film. *Nature*, 178(4534):650–651, 1956.

[28] J. R. A. Pearson. On convection cells induced by surface tension. *Journal of Fluid Mechanics*, 4(5):489–500, 1958.

[29] L. E. Scriven and C. V. Sternling. On cellular convection driven by surface-tension gradients - Effects of mean surface tension and surface viscosity. *Journal of Fluid Mechanics*, 19(3):321–340, 1964.

[30] M. K. Smith and S. H. Davis. Instabilities of dynamic thermocapillary liquid layers. Part 2. Surface-wave instabilities. *Journal of Fluid Mechanics*, 132(Jul):145–162, 1983.

[31] S. H. Davis. Thermocapillary instabilities. *Annual Review of Fluid Mechanics*, 19:403–435, 1987.

[32] M. K. Smith. Instability mechanisms in dynamic thermocapillary liquid layers. *Physics of Fluids*, 29(10):3182–3186, 1986.

[33] J. M. Garr-Peters. The neutral stability of surface-tension driven cavity flows subject to buoyant forces - I. Transverse and longitudinal disturbances. *Chemical Engineering Science*, 47(5):1247–1264, 1992.

[34] J. M. Garr-Peters. The neutral stability of surface-tension driven cavity flows subject to buoyant forces - II. Oblique disturbances. *Chemical Engineering Science*, 47(5):1265–1276, 1992.

[35] P. M. Parmentier, V. C. Regnier, and G. Lebon. Buoyant-thermocapillary instabilities in medium-Prandtl-number fluid layers subject to a horizontal temperature-gradient. *International Journal of Heat and Mass Transfer*, 36(9):2417–2427, 1993.

[36] J. F. Mercier and C. Normand. Buoyant-thermocapillary instabilities of differentially heated liquid layers. *Physics of Fluids*, 8(6):1433–1445, 1996.

[37] C. F. Chan and C. L. Chen. Effect of gravity on the stability of thermocapillary convection in a horizontal fluid layer. *Journal of Fluid Mechanics*, 647:91–103, 2010.

[38] M. F. Schatz and G. P. Neitzel. Experiments on thermocapillary instabilities. *Annual Review of Fluid Mechanics*, 33:93–127, 2001.

[39] J. Burguete, N. Mukolobwiez, F. Daviaud, N. Garnier, and A. Chiffaudel. Buoyant-thermocapillary instabilities in extended liquid layers subjected to a horizontal temperature gradient. *Physics of Fluids*, 13(10):2773–2787, 2001.

[40] R. J. Riley and G. P. Neitzel. Instability of thermocapillary-buoyancy convection in shallow layers. Part 1. Characterization of steady and oscillatory instabilities. *Journal of Fluid Mechanics*, 359:143–164, 1998.

[41] D. Schwabe, U. Moller, J. Schneider, and A. Scharmann. Instabilities of shallow dynamic thermocapillary liquid layers. *Physics of Fluids*, 4(11):2368–2381, 1992.

[42] J. Y. Xu and A. Zebib. Oscillatory two- and three-dimensional thermocapillary convection. *Journal of Fluid Mechanics*, 364:187–209, 1998.

[43] E. Bucchignani. Numerical characterization of hydrothermal waves in a laterally heated shallow layer. *Physics of Fluids*, 16(11):3839–3849, 2004.

[44] Y. R. Li, L. Peng, Y. Akiyama, and N. Imaishi. Three-dimensional numerical simulation of thermocapillary flow of moderate Prandtl number fluid in an annular pool. *Journal of Crystal Growth*, 259(4):374–387, 2003.

[45] B. C. Sim, A. Zebib, and D. Schwabe. Oscillatory thermocapillary convection in open cylindrical annuli. Part 2. Simulations. *Journal of Fluid Mechanics*, 491:259–274, 2003.

[46] Y. R. Li, N. Imaishi, T. Azami, and T. Hibiya. Three-dimensional oscillatory flow in a thin annular pool of silicon melt. *Journal of Crystal Growth*, 260(1-2):28–42, 2004.

[47] W. Y. Shi and N. Imaishi. Hydrothermal waves in differentially heated shallow annular pools of silicone oil. *Journal of Crystal Growth*, 290(1):280–291, 2006.

[48] L. Peng, Y. R. Li, W. Y. Shi, and N. Imaishi. Three-dimensional thermocapillary-buoyancy flow of silicone oil in a differentially heated annular pool. *International Journal of Heat and Mass Transfer*, 50(5-6):872–880, 2007.

[49] W. Y. Shi, G. Y. Li, X. Liu, Y. R. Li, L. Peng, and N. Imaishi. Thermocapillary convection and buoyant-thermocapillary convection in the annular pools of silicon melt and silicone oil. *Journal of Superconductivity and Novel Magnetism*, 23(6):1169–1172, 2010.

[50] A. M. Mancho and H. Herrero. Instabilities in a laterally heated liquid layer. *Physics of Fluids*, 12(5):1044–1051, 2000.

[51] D. Merkt and M. Bestehorn. Benard-Marangoni convection in a strongly evaporating fluid. *Physica D-Nonlinear Phenomena*, 185(3-4):196–208, 2003.

[52] H. Mancini and D. Maza. Pattern formation without heating in an evaporative convection experiment. *Europhysics Letters*, 66(6):812–818, 2004.

[53] O. Ozen and R. Narayanan. The physics of evaporative and convective instabilities in bilayer systems: Linear theory. *Physics of Fluids*, 16(12):4644–4652, 2004.

[54] E. Sultan, A. Boudaoud, and M. Ben Amar. Evaporation of a thin film: diffusion of the vapour and Marangoni instabilities. *Journal of Fluid Mechanics*, 543:183–202, 2005.

[55] K. Kanatani. Effects of convection and diffusion of the vapour in evaporating liquid films. *Journal of Fluid Mechanics*, 732:128–149, 2013.

[56] H. J. Palmer. Hydrodynamic stability of rapidly evaporating liquids at reduced pressure. *Journal of Fluid Mechanics*, 75(Jun11):487–511, 1976.

[57] K. Kanatani and A. Oron. Nonlinear dynamics of confined thin liquid-vapor bilayer systems with phase change. *Physics of Fluids*, 23(3):032102, 2011.

[58] W. Guo and R. Narayanan. Interfacial instability due to evaporation and convection: linear and nonlinear analyses. *Journal of Fluid Mechanics*, 650:363–389, 2010.

[59] O. E. Shklyaev and E. Fried. Stability of an evaporating thin liquid film. *Journal of Fluid Mechanics*, 584:157–183, 2007.

[60] J. Margerit, M. Dondlinger, and P. C. Dauby. On the use of Galerkin-Eckhaus method to study the nonlinear regime of Marangoni-Benard instabilities in an evaporating liquid layer. *European Physical Journal B*, 54(4):485–492, 2006.

[61] J. Margerit, M. Dondlinger, and P. C. Dauby. Improved 1.5-sided model for the weakly nonlinear study of Benard-Marangoni instabilities in an evaporating liquid layer. *Journal of Colloid and Interface Science*, 290(1):220–230, 2005.

[62] A. Oron and S. G. Bankoff. Dewetting of a heated surface by an evaporating liquid film under conjoining/disjoining pressures. *Journal of Colloid and Interface Science*, 218(1):152–166, 1999.

[63] J. P. Burelbach, S. G. Bankoff, and S. H. Davis. Nonlinear stability of evaporating condensing liquid-films. *Journal of Fluid Mechanics*, 195:463–494, 1988.

[64] B. Haut and P. Colinet. Surface-tension-driven instabilities of a pure liquid layer evaporating into an inert gas. *Journal of Colloid and Interface Science*, 285(1):296–305, 2005.

[65] G. B. McFadden, S. R. Coriell, K. F. Gurski, and D. L. Cotrell. Onset of convection in two liquid layers with phase change. *Physics of Fluids*, 19(10):104109, 2007.

[66] K. Sefiane, J. R. Moffat, O. K. Matar, and R. V. Craster. Self-excited hydrothermal waves in evaporating sessile drops. *Applied Physics Letters*, 93(7):074103, 2008.

[67] K. Sefiane, A. Steinchen, and R. Moffat. On hydrothermal waves observed during evaporation of sessile droplets. *Colloids and Surfaces a-Physicochemical and Engineering Aspects*, 365(1-3):95–108, 2010.

[68] D. Brutin, B. Sobac, F. Rigollet, and C. Le Niliot. Infrared visualization of thermal motion inside a sessile drop deposited onto a heated surface. *Experimental Thermal and Fluid Science*, 35(3):521–530, 2011.

[69] B. Sobac and D. Brutin. Thermocapillary instabilities in an evaporating drop deposited onto a heated substrate. *Physics of Fluids*, 24(3), 2012.

[70] F. Carle, B. Sobac, and D. Brutin. Hydrothermal waves on ethanol droplets evaporating under terrestrial and reduced gravity levels. *Journal of Fluid Mechanics*, 712:614–623, 2012.

[71] K. Sefiane, Y. Fukatani, Y. Takata, and J. Kim. Thermal patterns and hydrothermal waves (HTWs) in volatile drops. *Langmuir*, 29(31):9750–9760, 2013.

[72] G. Karapetsas, O. K. Matar, P. Valluri, and K. Sefiane. Convective rolls and hydrothermal waves in evaporating sessile drops. *Langmuir*, 28(31):11433–11439, 2012.

[73] G. J. Dunn, S. K. Wilson, B. R. Duffy, S. David, and K. Sefiane. The strong influence of substrate conductivity on droplet evaporation. *Journal of Fluid Mechanics*, 623:329–351, 2009.

[74] A. M. Cazabat and G. Guena. Evaporation of macroscopic sessile droplets. *Soft Matter*, 6(12):2591–2612, 2010.

[75] H. Y. Erbil. Evaporation of pure liquid sessile and spherical suspended drops: A review. *Advances in Colloid and Interface Science*, 170(1-2):67–86, 2012.

[76] D. M. Anderson and S. H. Davis. The spreading of volatile liquid droplets on heated surfaces. *Physics of Fluids*, 7(2):248–265, 1995.

[77] V. S. Ajaev. Spreading of thin volatile liquid droplets on uniformly heated surfaces. *Journal of Fluid Mechanics*, 528:279–296, 2005.

[78] R. G. Picknett and R. Bexon. Evaporation of sessile or pendant drops in still air. *Journal of Colloid and Interface Science*, 61(2):336–350, 1977.

[79] C. Bourgès-Monnier and M. E. R. Shanahan. Influence of evaporation on contact angle. *Langmuir*, 11(7):2820–2829, 1995.

[80] H. Hu and R. G. Larson. Analysis of the microfluid flow in an evaporating sessile droplet. *Langmuir*, 21(9):3963–3971, 2005.

[81] H. Hu and R. G. Larson. Analysis of the effects of Marangoni stresses on the microflow in an evaporating sessile droplet. *Langmuir*, 21(9):3972–3980, 2005.

[82] H. Hu and R. G. Larson. Marangoni effect reverses coffee-ring depositions. *Journal of Physical Chemistry B*, 110(14):7090–7094, 2006.

[83] W. D. Ristenpart, P. G. Kim, C. Domingues, J. Wan, and H. A. Stone. Influence of substrate conductivity on circulation reversal in evaporating drops. *Physical Review Letters*, 99(23), 2007.

[84] K. S. Birdi, D. T. Vu, and A. Winter. A study of the evaporation rates of small water drops placed on a solid-surface. *Journal of Physical Chemistry*, 93(9):3702–3703, 1989.

[85] S. M. Rowan, M. I. Newton, and G. Mchale. Evaporation of microdroplets and the wetting of solid-surfaces. *Journal of Physical Chemistry*, 99(35):13268–13271, 1995.

[86] H. Y. Erbil, G. McHale, and M. I. Newton. Drop evaporation on solid surfaces: Constant contact angle mode. *Langmuir*, 18(7):2636–2641, 2002.

[87] C. Poulard, O. Benichou, and A. M. Cazabat. Freely receding evaporating droplets. *Langmuir*, 19(21):8828–8834, 2003.

[88] E. F. Crafton and W. Z. Black. Heat transfer and evaporation rates of small liquid droplets on heated horizontal surfaces. *International Journal of Heat and Mass Transfer*, 47(6-7):1187–1200, 2004.

[89] R. Mollaret, K. Sefiane, J. R. E. Christy, and D. Veyret. Experimental and numerical investigation of the evaporation into air of a drop on a heated surface. *Chemical Engineering Research & Design*, 82(A4):471–480, 2004.

[90] S. David, K. Sefiane, and L. Tadrist. Experimental investigation of the effect of thermal properties of the substrate in the wetting and evaporation of sessile drops. *Colloids and Surfaces a-Physicochemical and Engineering Aspects*, 298(1-2):108–114, 2007.

[91] K. Sefiane and R. Bennacer. An expression for droplet evaporation incorporating thermal effects. *Journal of Fluid Mechanics*, 667:260–271, 2011.

[92] B. Sobac and D. Brutin. Thermal effects of the substrate on water droplet evaporation. *Physical Review E*, 86(2), 2012.

[93] X. F. Xu and J. B. Luo. Marangoni flow in an evaporating water droplet. *Applied Physics Letters*, 91(12), 2007.

[94] K. Sefiane, S. K. Wilson, S. David, G. J. Dunn, and B. R. Duffy. On the effect of the atmosphere on the evaporation of sessile droplets of water. *Physics of Fluids*, 21(6):062101–1 – 062101–9, 2009.

[95] M. E. R. Shanahan, K. Sefiane, and J. R. Moffat. Dependence of volatile droplet lifetime on the hydrophobicity of the substrate. *Langmuir*, 27(8):4572–4577, 2011.

[96] T. A. H. Nguyen and A. V. Nguyen. Increased evaporation kinetics of sessile droplets by using nanoparticles. *Langmuir*, 28(49):16725–16728, 2012.

[97] J. M. Stauber, S. K. Wilson, B. R. Duffy, and K. Sefiane. On the lifetimes of evaporating droplets. *Journal of Fluid Mechanics*, 744:R2, 2014.

[98] K. Sefiane and L. Tadrist. Experimental investigation of the de-pinning phenomenon on rough surfaces of volatile drops. *International Communications in Heat and Mass Transfer*, 33(4):482–490, 2006.

[99] J. R. Moffat, K. Sefiane, and M. E. R. Shanahan. Effect of TiO2 nanoparticles on contact line stick-slip behavior of volatile drops. *Journal of Physical Chemistry B*, 113(26):8860–8866, 2009.

[100] D. Orejon, K. Sefiane, and M. E. R. Shanahan. Stick-slip of evaporating droplets: Substrate hydrophobicity and nanoparticle concentration. *Langmuir*, 27(21):12834–12843, 2011.

[101] M. E. R. Shanahan. Simple theory of stick-slip wetting hysteresis. *Langmuir*, 11(3):1041–1043, 1995.

[102] O. E. Ruiz and W. Z. Black. Evaporation of water droplets placed on a heated horizontal surface. *Journal of Heat Transfer-Transactions of the Asme*, 124(5):854–863, 2002.

[103] F. Girard, M. Antoni, S. Faure, and A. Steinchen. Evaporation and Marangoni driven convection in small heated water droplets. *Langmuir*, 22(26):11085–11091, 2006.

[104] F. Girard, M. Antoni, S. Faure, and A. Steinchen. Influence of heating temperature and relative humidity in the evaporation of pinned droplets. *Colloids and Surfaces a-Physicochemical and Engineering Aspects*, 323(1-3):36–49, 2008.

[105] F. Girard, M. Antoni, and K. Sefiane. On the effect of Marangoni flow on evaporation rates of heated water drops. *Langmuir*, 24(17):9207–9210, 2008.

[106] F. Girard and M. Antoni. Influence of substrate heating on the evaporation dynamics of pinned water droplets. *Langmuir*, 24(20):11342–11345, 2008.

[107] E. Y. Gatapova, A. A. Semenova, D. V. Zaitsev, and O. A. Kabov. Evaporation of a sessile water drop on a heated surface with controlled wettability. *Colloids and Surfaces a-Physicochemical and Engineering Aspects*, 441:776–785, 2014.

[108] Yi Sui, Hang Ding, and Peter D.M. Spelt. Numerical simulations of flows with moving contact lines. *Annual Review of Fluid Mechanics*, 46(1):97–119, 2014.

[109] P. J. Sáenz, P. Valluri, K. Sefiane, G. Karapetsas, and O. K. Matar. Linear and nonlinear stability of hydrothermal waves in planar liquid layers driven by thermocapillarity. *Physics of Fluids*, 25(9):094101, 2013.

[110] A. Alexeev, T. Gambaryan-Roisman, and P. Stephan. Marangoni convection and heat transfer in thin liquid films on heated walls with topography: Experiments and numerical study. *Physics of Fluids*, 17(6), 2005.

[111] A. Alexeev and A. Oron. Suppression of the Rayleigh-Taylor instability of thin liquid films by the marangoni effect. *Physics of Fluids*, 19(8), 2007.

[112] C. Ma and D. Bothe. Direct numerical simulation of thermocapillary flow based on the Volume of Fluid method. *International Journal of Multiphase Flow*, 37(9):1045–1058, 2011.

[113] C. W. Hirt and B. D. Nichols. Volume of Fluid (VOF) method for the dynamics of free boundaries. *Journal of Computational Physics*, 39(1):201–225, 1981.

[114] R. Scardovelli and S. Zaleski. Direct numerical simulation of free-surface and interfacial flow. *Annual Review of Fluid Mechanics*, 31:567–603, 1999.

[115] J. U. Brackbill, D. B. Kothe, and C. Zemach. A continuum method for modeling surface-tension. *Journal of Computational Physics*, 100(2):335–354, 1992.

[116] O. Ubbink and R. I. Issa. A method for capturing sharp fluid interfaces on arbitrary meshes. *Journal of Computational Physics*, 153(1):26–50, 1999.

[117] F. Daviaud and J. M. Vince. Traveling waves in a fluid layer subjected to a horizontal temperature-gradient. *Physical Review E*, 48(6):4432–4436, 1993.

[118] S. Kumar and O. K. Matar. On the Faraday instability in a surfactant-covered liquid. *Physics of Fluids*, 16(1):39–46, 2004.

[119] M. A. Pelacho, A. Garcimartin, and J. Burguete. Local Marangoni number at the onset of hydrothermal waves. *Physical Review E*, 62(1):477–483, 2000.

[120] J. Burguete, H. Chate, F. Daviaud, and N. Mukolobwiez. Bekki-Nozaki amplitude holes in hydrothermal nonlinear waves. *Physical Review Letters*, 82(16):3252–3255, 1999.

[121] P. J. Sáenz, P. Valluri, K. Sefiane, G. Karapetsas, and O. K. Matar. On phase change in Marangoni-driven flows and its effects on the hydrothermal-wave instabilities. *Physics of Fluids*, 26(2):024114, 2014.

[122] I. Langmuir. The evaporation of small spheres. *Physical Review*, 12(5):368–370, 1918.

[123] Z. Q. Zhu and Q. S. Liu. Coupling of thermocapillary convection and evaporation effect in a liquid layer when the evaporating interface is open to air. *Chinese Science Bulletin*, 55(3):233–238, 2010.

[124] D. Villers and J. K. Platten. Coupled buoyancy and Marangoni convection in acetone - Experiments and comparison with numerical simulations. *Journal of Fluid Mechanics*, 234:487–510, 1992.

[125] P. Kavehpour, B. Ovryn, and G. H. McKinley. Evaporatively-driven Marangoni instabilities of volatile liquid films spreading on thermally conductive substrates. *Colloids and Surfaces a-Physicochemical and Engineering Aspects*, 206(1-3):409–423, 2002.

[126] T. H. Kim, E. Kommer, S. Dessiatoun, and J. Kim. Measurement of two-phase flow and heat transfer parameters using infrared thermometry. *International Journal of Multiphase Flow*, 40:56–67, 2012.

[127] T. A. H. Nguyen, A. V. Nguyen, M. A. Hampton, Z. P. Xu, L. B. Huang, and V. Rudolph. Theoretical and experimental analysis of droplet evaporation on solid surfaces. *Chemical Engineering Science*, 69(1):522–529, 2012.

[128] D. M. Anderson, G. B. McFadden, and A. A. Wheeler. Diffuse-interface methods in fluid mechanics. *Annual Review of Fluid Mechanics*, 30:139–165, 1998.

[129] D. Jacqmin. Calculation of two-phase Navier-Stokes flows using phase-field modeling. *Journal of Computational Physics*, 155(1):96–127, 1999.

[130] H. Ding, P. D. M. Spelt, and C. Shu. Diffuse interface model for incompressible two-phase flows with large density ratios. *Journal of Computational Physics*, 226(2):2078–2095, 2007.

[131] V. E. Badalassi, H. D. Ceniceros, and S. Banerjee. Computation of multiphase systems with phase field models. *Journal of Computational Physics*, 190(2):371–397, 2003.

[132] J. S. Rowlinson. Translation of JD van der Waals "The thermodynamik theory of capillarity under the hypothesis of a continuous variation of density". *Journal of Statistical Physics*, 20(2):197–200, 1979.

[133] J. W. Cahn and J. E. Hilliard. Free energy of a nonuniform system .1. Interfacial free energy. *Journal of Chemical Physics*, 28(2):258–267, 1958.

[134] J. W. Cahn and J. E. Hilliard. Free energy of a nonuniform system .3. Nucleation in a 2-component incompressible fluid. *Journal of Chemical Physics*, 31(3):688–699, 1959.

[135] J. W. Cahn. On spinodal decomposition. *Acta Metallurgica*, 9(9):795–801, 1961.

[136] H. Ding and P. D. M. Spelt. Inertial effects in droplet spreading: a comparison between diffuse-interface and level-set simulations. *Journal of Fluid Mechanics*, 576:287–296, 2007.

[137] H. Ding and P. D. M. Spelt. Onset of motion of a three-dimensional droplet on a wall in shear flow at moderate Reynolds numbers. *Journal of Fluid Mechanics*, 599:341–362, 2008.

[138] H. Ding, M. N. H. Gilani, and P. D. M. Spelt. Sliding, pinch-off and detachment of a droplet on a wall in shear flow. *Journal of Fluid Mechanics*, 644:217–244, 2010.

[139] P. Valluri, L. o. Naraigh, H. Ding, and P. D. M. Spelt. Linear and nonlinear spatio-temporal instability in laminar two-layer flows. *Journal of Fluid Mechanics*, 656:458–480, 2010.

[140] D. Jacqmin. Contact-line dynamics of a diffuse fluid interface. *Journal of Fluid Mechanics*, 402:57–88, 2000.

[141] P. T. Yue, C. F. Zhou, and J. J. Feng. Sharp-interface limit of the Cahn-Hilliard model for moving contact lines. *Journal of Fluid Mechanics*, 645:279–294, 2010.

[142] H. Ding and P. D. M. Spelt. Wetting condition in diffuse interface simulations of contact line motion. *Physical Review E*, 75(4), 2007.

[143] U. M. Ascher, S. J. Ruuth, and B. T. R. Wetton. Implicit explicit methods for time-dependent partial-differential equations. *Siam Journal on Numerical Analysis*, 32(3):797–823, 1995.

[144] X. D. Liu, S. Osher, and T. Chan. Weighted Essentially Nonoscillatory Schemes. *Journal of Computational Physics*, 115(1):200–212, 1994.

[145] P. Seppecher. Moving contact lines in the Cahn-Hilliard theory. *International Journal of Engineering Science*, 34(9):977–992, 1996.

[146] T. Z. Qian, X. P. Wang, and P. Sheng. A variational approach to moving contact line hydrodynamics. *Journal of Fluid Mechanics*, 564:333–360, 2006.

[147] A. Carlson, M. Do-Quang, and G. Amberg. Modeling of dynamic wetting far from equilibrium. *Physics of Fluids*, 21(12), 2009.

[148] P. L. Kelly-Zion, C. J. Pursell, N. Hasbamrer, B. Cardozo, K. Gaughan, and K. Nickels. Vapor distribution above an evaporating sessile drop. *International Journal of Heat and Mass Transfer*, 65:165–172, 2013.